1 All-Sky Direct Aerosol Radiative Effects Estimated from

2 Integrated A-Train Satellite Measurements

- 3 Meloë S.F. Kacenelenbogen¹, Ralph Kuehn², Nandana Amarasinghe³, Kerry Meyer¹, Edward
- 4 Nowottnick¹, Mark Vaughan⁴, Hong Chen⁵, Sebastian Schmidt⁵, Richard Ferrare⁴, John Hair⁴,
- 5 Robert C. Levy¹, Hongbin Yu¹, Paquita Zuidema⁶, Robert Holz², Willem Marais²
- 6 NASA Goddard Space Flight Center, Greenbelt, MD, USA
- ²Cooperative Institute for Meteorological Satellite Studies, Space Science and Engineering Center, University of
- 8 Wisconsin—Madison, Madison, Wisconsin, USA
- 9 ³Science Systems and Applications Inc/NASA Goddard Space Flight Center, Lanham, MD, USA
- 10 ⁴NASA Langley Research Center, Hampton, Virginia, USA
- ⁵Department of Atmospheric and Oceanic Sciences, University of Colorado, Boulder, CO, USA
- 12 ⁶Rosenstiel School of Atmospheric, Marine and Earth Science, University of Miami, Miami, Florida, USA
- 14 Correspondence to: Meloë S. F. Kacenelenbogen (meloe.s.kacenelenbogen@nasa.gov)
- 16 Abstract. The improvement of satellite-derived calculations of the Direct Aerosol Radiative Effects (DARE) is
- 17 essential for reducing the uncertainty in the impact of aerosol on solar radiation. We develop a framework to compute
- 18 DARE at the top of the Earth's atmosphere, in the short-wave part of the electromagnetic spectrum and in all-sky
- 19 conditions along the track of the A-Train constellation of satellites. We use combined state-of-the-art aerosol and
- 20 cloud properties from satellite sensors Cloud-Aerosol Lidar with Orthogonal Polarization (CALIOP) and Moderate
- 21 Resolution Imaging Spectroradiometer (MODIS). We also use a global reanalysis from the Modern-Era Retrospective
- 22 analysis for Research and Applications Version 2 (MERRA-2) to provide vertical distribution of aerosol properties
- 23 and atmospheric conditions. Diurnal mean satellite DARE values range from -25 (cooling) to 40 W·m⁻² (warming)
- 24 over the Southeast Atlantic during three days from the NASA ObseRvations of Aerosols above CLouds and their
- 25 intEractionS (ORACLES) aircraft campaign. These three days indicate agreement between our satellite-calculated
- DARE and co-located airborne Solar Spectral Flux Radiometer (SSFR) measurements. This paper constitutes the first
- step before applying our algorithm to more years of combined satellite and model data over more regions of the world.
- 28 The goal is to ultimately assess the order of importance of atmospheric parameters in the calculation of DARE for
- 29 specific aerosol and cloud regimes. This will inform future missions where, when and how accurately the retrievals
- 30 should be performed to reduce all-sky DARE uncertainties.

32 Key Points.

31

33

13

- 34 Our semi-observational estimates of all-sky Direct Aerosol Radiative Effect (DARE), along the CALIPSO orbital
- track, compare well with suborbital measurements during the ORACLES field campaign over the Southeast Atlantic.

- This paper constitutes the foundation for extending the algorithm to broader regions and multiple years to assess the order of importance of atmospheric parameters in the calculation of DARE for specific aerosol and cloud regimes.
- 38• We discuss the limitations in our semi-observational satellite all-sky DARE results

41 42

43

44

45

46

47 48

49

50

51

5253

54

55

56

57 58

59 60

1 Introduction

Small suspended individual particles (aerosols) can scatter, reflect and/or absorb incoming sunlight (also called direct aerosol-radiation interactions) and influence cloud properties (also called aerosol-cloud interactions or indirect aerosol-radiation interactions), both of which perturb the radiation balance of the Earth-atmosphere system. The impact of aerosols on solar radiation plays a key role in the Earth's climate as they offset roughly one-third of the warming from anthropogenic greenhouse gases (Li et al., 2022). The aerosol radiative effect is the immediate impact of aerosols on the radiation budget, while the aerosol radiative forcing is the change in that impact compared to preindustrial times. Reducing uncertainties in the total aerosol radiative forcing contributes to reducing uncertainty in quantifying present-day climate change (Forster et al., 2021). Although uncertainties in aerosol-cloud interactions dominate the total aerosol radiative forcing (given a global anthropogenic aerosol radiative forcing of $-1.0 \pm 0.7~\mathrm{W \cdot m^{-1}}$ 2), uncertainties due to aerosol-radiation interactions are still on the order of 100% (given a global anthropogenic radiative forcing of -0.3 ± 0.3 W·m⁻²) (Forster et al., 2021). These uncertainties represent model diversity and are generally considered a lower bound on uncertainty (e.g., Li et al., 2022). To illustrate, Myhre et al. (2013) conducted aerosol comparisons between observations and models, and reported a large inter-model spread in the Radiative Forcing due to aerosol-radiation interactions (RFari) of the aerosol species. For example, a range from 0.05 to 0.37 W·m⁻² in RFari exists from Black Carbon (BC, the dominant light absorbing biomass burning (BB) smoke aerosol component across all visible wavelengths), with a standard deviation of 0.07 W·m⁻² compared to a mean RFari of 0.18 W·m⁻² of BC (i.e., a 40% relative standard deviation). Our study focuses on the instantaneous or diurnally-averaged direct aerosol radiative effect (i.e., without consideration of pre-industrial times) in the shortwave (SW) part of the electromagnetic spectrum (i.e., four broad band channels between 345 nm and 1242 nm, to be exact), at the Top-Of-Atmosphere (TOA), in all-sky conditions (i.e., in cloud-free and cloudy skies) without distinguishing between aerosols from human-made (anthropogenic) or natural sources.

62 63

64

61

The instantaneous TOA SW Direct Aerosol Radiative Effects (DARE) – referred to as DARE in $W \cdot m^{-2}$ – quantifies the difference in the net radiative flux at TOA, F^{net} , due to perturbations in the loading of aerosol in the atmosphere, which can be expressed by the following equation:

6566

```
67 DARETOA
```

68 =
$$F_{aerosol\ present}^{net} - F_{no\ aerosol\ present}^{net}$$

69 = $\left(F_{aerosol\ present}^{\downarrow,TOA} - F_{aerosol\ present}^{\uparrow,TOA}\right) - \left(F_{no\ aerosol\ present}^{\downarrow,TOA} - F_{no\ aerosol\ present}^{\uparrow,TOA}\right)$

70

(1)

71 where F^{\downarrow} and F^{\uparrow} are the downwelling and upwelling flux. Since the incoming solar radiation is the same (i.e.,

 $F_{aerosol\ present}^{\downarrow,TOA} = F_{no\ aerosol\ present}^{\downarrow,TOA}$), DARE can be simplified as the change in the upwelling radiative flux at TOA

73 (i.e., $F_{no\ aerosol\ present}^{\uparrow,TOA} - F_{aerosol\ present}^{\uparrow,TOA}$).

A negative DARE indicates a cooling effect because more energy leaves the Earth's climate system, while a positive DARE indicates a trap of energy in the climate system or a warming effect. The magnitude and sign of DARE depends on extensive aerosol properties (which are associated with aerosol loading), intensive aerosol properties (which are associated solely with aerosol type) and the reflectivity of the underlying surface (e.g., Yu et al., 2006; Chand et al., 2009; Wilcox et al., 2012; Peters et al., 2011; De Graaf et al., 2012, 2014; Meyer et al., 2013, 2015; Peers et al., 2015; Feng and Christopher, 2015). For example, even for a homogeneous aerosol layer, Russell et al. (2002) showed how DARE can switch from negative values (cooling) in non-cloudy skies over oceans (low surface albedo) to positive

values (warming) over clouds (high surface albedo).

 Substantial progress has been made in the estimation of DARE in non-cloudy skies using satellite observations (e.g., Yu et al., 2006; Oikawa et al., 2013, 2018, Matus et al., 2015, 2019, Korras-Carraca et al., 2019, Lacagnina et al., 2017, Thorsen et al., 2021). However, fewer studies use satellite observations to estimate DARE above optically thick clouds, and even fewer studies are devoted to DARE estimates above all types of clouds (e.g., De Graaf et al., 2012, 2014; Meyer et al., 2013, 2015; Zhang et al., 2016; Thorsen et al., 2021). The number of studies examining DARE below optically thin clouds is vanishingly small. By not including aerosols below thin clouds in all-sky DARE calculations, a significant portion of the total aerosol effect on radiation is missed. Previous studies listed in Thorsen et al. (2021) show a wide range of DARE values using satellites, i.e., from -3.1 to -0.61 W·m⁻² in all-skies and from -7.3 to -2.2 W·m⁻² in non-cloudy skies. This is why further reduction in the overall (still significant) uncertainties in observational DARE is needed. As such, it is important to account for the vertical order, location and amount of different tropospheric aerosol types, the ocean and cloud reflectivity using satellite observations to calculate DARE.

In this paper, we develop a framework to compute a semi-observational DARE along the track of the A-Train constellation of satellites using combined aerosol and cloud properties from state-of-the-art satellite sensors CALIOP/CALIPSO and MODIS/Aqua. We describe this as a "semi-observational" product because MERRA-2, a global reanalysis that assimilates space-based observations of aerosols is used to provide additional aerosol intensive properties and atmospheric conditions. We use MODIS-derived pixel-level cloud properties such as Cloud Fraction (CF) and the cloud albedo, which is mostly informed by the Cloud Optical Thickness (COT), and the Cloud droplet Effective Radius (CER) (note that Cloud Water Path (CWP) can also be derived from COT and CER) (Twomey, 1974). CF is the percentage of a given pixel in a satellite image that is covered by clouds. COT is a measurement of how much light is scattered and reflected by clouds, indicating how "thick" clouds appear to be. CER represents the average size of cloud droplets. CWP is a measurement of the total amount of liquid water contained within a vertical column of a cloud, indicating how much water is present in clouds.

CALIOP and MERRA-2 aerosol properties used in all-sky DARE calculations are the spectral Aerosol Optical Depth (AOD), Single Scattering Albedo (SSA) and asymmetry parameter (ASY), as well as the aerosol vertical distribution in the atmosphere, and particularly its location relative to clouds. AOD is a measure of the extinction of sunlight due to aerosols that depends on the aerosol amount and aerosol type (e.g., for a fixed loading and relative humidity, the AOD of smoke will be significantly higher than the AOD of marine aerosols). SSA is a measure of aerosol light scattering over light extinction which depends on the light absorption (i.e. the aerosol composition) and the aerosol size. ASY is a measure of the directionality of scattered light from the aerosol (e.g., if the radiation is scattered back to space, there is a loss of energy for the Earth's climate system) and depends on particle shape. The spectral dependence of the AOD is a first-order indication of the effective size of the aerosol particles. To illustrate the effective particle size of the aerosol (to the first order) in our study, we introduce the Extinction Angstrom Exponent (EAE) parameter, the ratio of two aerosol extinction coefficients at two different wavelengths divided by the ratio of these two wavelengths in log space. Coarse size mode-dominated particles (e.g., dust aerosols) usually record smaller EAE values compared to fine-mode dominated particles (e.g., smoke). Finally, the spectral shape of SSA is useful for distinguishing between different types of absorbing aerosols (e.g., Russell et al., 2014; Kacenelenbogen et al., 2022).

We compute DARE for three specific days over the Southeast Atlantic (this paper) as a first step before extending the study to multiple years and other regions of the globe. We carefully select our case studies such that our semi-observational satellite DARE results can be validated against airborne observations from the ORACLES campaign. Several studies have attempted to estimate DARE over the Southeast Atlantic (see, for example, the studies listed in Table 1 of Kacenelenbogen et al., (2019)). This region is known to show global maximum positive DARE values (e.g., Waquet et al., 2013). According to Jouan et al. (2024), the long-term increase of biomass burning aerosols over the Southeast Atlantic could represent an underrecognized source of global warming (i.e., all-sky DARE has become more positive, $+0.04 \pm 0.15$ W m⁻² yr⁻¹, due to aerosols in cloudy sky regions). Note that the long-term increase of smoke over this region can be attributed to increased warm temperature advection and strengthening of the easterly winds over time (Tatro and Zuidema, 2025).

The paper is organized as follows - Section 2 describes a framework to compute DARE in the case of a few identified atmospheric scenarios along the satellite track. Section 3 presents our semi-observational estimates of DARE, the inputs of aerosol and cloud parameters, and comparisons against field campaign measurements during our three case studies. Sections 4 and 5 discuss future work and conclude our paper.

2 Data and Method

In this paper, we present two estimates of DARE (both in W m⁻²). First, a DARE_obs parameter that uses observations from satellite sensors and estimations from a model (see section 2.1) and represents the main results of our study. Second, a parametrized DARE_param parameter based on Cochrane et al. (2021) is used as one of two ways to evaluate our DARE_obs results (see section 2.2).

- Table 1 defines the acronyms used to describe the satellite-derived and model-based computational inputs to the
- DARE calculations. Table 2 summarizes the steps required to calculate estimates of DARE_obs and DARE_param.
- The subsections of section 2 describe the contents of Table 2 in further detail.

| | Input Parameter | Description | | | | |
|------------------|--------------------------------|--|--|--|--|--|
| | to DARE | | | | | |
| | Calculation | | | | | |
| | CALIOP _{ACAOD_stand} | CALIOP above-cloud AOD (ACAOD) or total column AOD at 532nm | | | | |
| | _ | obtained by integrating the standard CALIOP version 4.51 (V4.51) | | | | |
| | ard Or | aerosol extinction profile (Young and Vaughan, 2009) between the | | | | |
| m) | CALIOP _{AOD_standard} | aerosol top and base heights above clouds or in non-cloudy skies | | | | |
| /3 k | CALIOD | CALIOP V4.51 above-cloud AOD at 532 nm derived using the | | | | |
| CALIOP (~1/3 km) | $CALIOP_{ACAOD_DR}$ | depolarization ratio (DR) method described in Hu et al. (2007) | | | | |
| TOI | CALIOP _{ODAOD} | CALIOP V4.51 total column AOD at 532 nm estimated using the Ocean | | | | |
| CAI | | Derived Aerosol Optical Depths (ODAOD) product (Ryan et al., 2024) | | | | |
| | CALIOP _{vfm} | CALIOP V4.51 Vertical Feature Mask (VFM) reports detected layer | | | | |
| | | heights and identifies aerosols and clouds according to type and subtype | | | | |
| | | (Vaughan et al., 2009; Liu et al., 2010) | | | | |
| | | (i) Cloud optical/microphysical properties and cloud-top property | | | | |
| | | retrievals from MODIS Cloud Properties (CLDPROP) Version-1.1 | | | | |
| N | MODIS _{Cloud} (1km) | (Platnick et al., 2021) | | | | |
| | | (ii) MODIS aerosol and cloud products corrected for overlying aerosols | | | | |
| | | using a new aerosol radiative model (Meyer et al., 2015) | | | | |
| | | Atmospheric composition and weather profiles from the Modern-Era | | | | |
| M | ERRA-2 (~55 km) | Retrospective analysis for Research and Applications, Version 2 | | | | |
| | | (Gelaro et al., 2017) | | | | |

Table 1: Acronyms used to describe computational inputs to DARE_obs and DARE_param calculations in Table 2.

| Aerosol above and below a single low level (<3km) thick, thin and/ or broken liquid cloud and aerosol in mostly non-cloudy skies; Table 3 lists which satellite-derived criteria are used to define four atmospheric scenarios Model | | DARE_obs | DARE_param | | | | |
|---|-----------------------------|---|---------------------------------|--|--|--|--|
| Scenarios Skies; Table 3 lists which satellite-derived criteria are used to define four atmospheric scenarios RRTMG-SW CALIOP _{vfm} and MODIS _{Cloud} to select qualifying clouds and to define thick, broken and/ or thin clouds in atmospheric scenarios (see Table 3); MODIS _{Cloud} to assign cloud properties (i.e., CWP, CER, COT) (section 2.1.1) Cloud Albedo N/A Cloud Albedo Cloud Top Height (CTH) and Cloud Base Height (CBH) Aerosol Top Height (ABH) CALIOP _{vfm} to define CTH; CBH = CTH - 500m CALIOP _{vfm} to define ATH above clouds and ATH and ABH in non-cloudy skies; ABH = CTH above clouds; MERRA-2 to define ATH and ABH below clouds Vertical distribution of We use MERRA-2 (section N/A | | Aerosol above and below a single low level (<3km) thick, thin | | | | | |
| Model RRTMG-SW Cloud Detection and Characterization Cloud Albedo Cloud Top Height (CTH) and Cloud Base Height (ATH) and Aerosol Top Height (ATH) and Aerosol Base Height (Coud Merosol Base Height (ATH) and Aerosol Base Height (ATH) and ABH below clouds We use MERRA-2 (section N/A | Four Atmospheric | and/ or broken liquid cloud and aerosol in mostly non-cloudy | | | | | |
| Model RRTMG-SW Cloud Detection and Characterization Cloud Albedo Cloud Albedo Cloud Top Height (CTH) and Cloud Base Height (CBH) Aerosol Top Height (ATH) and Aerosol Base Height (ATH) above clouds; MERRA-2 to define ATH and ABH below clouds Vertical distribution of We use MERRA-2 (section N/A CALIOP _{vfm} and MODIS _{Cloud} to select qualifying clouds and to define thick, broken and/or thin clouds in atmospheric scenarios (see Table 3); MODIS _{Cloud} to assign cloud properties (i.e., CWP, CER, COT) (section 2.1.1) Computed for RRTMG bands (25) using Mic calculations and DISORT N/A CALIOP _{vfm} to define CTH; N/A CALIOP _{vfm} to define ATH and ABH in non-cloudy skies; ABH = CTH above clouds; MERRA-2 to define ATH and ABH below clouds COLIOP (Section 2.1.1) | Scenarios | skies; Table 3 lists which satellite-derived criteria are used to | | | | | |
| Cloud Detection and Characterization Cloud Albedo Cloud Top Height (CTH) and Cloud Base Height (CBH) Aerosol Top Height (ATH) and Aerosol Base Height (ATH) and ABH below clouds We use MERRA-2 (section N/A | | define four atmospheric scenarios | | | | | |
| Cloud Detection and Characterization Characterization Cloud Albedo Cloud Top Height (CTH) and Cloud Base Height (CBH) Aerosol Top Height (ATH) and Aerosol Base Height (ATH) and ABH below clouds; MERRA-2 to define ATH and ABH below clouds Vertical distribution of We use MERRA-2 (section N/A | Model | DDTMC SW | Eq. 12 of Cochrane et al. | | | | |
| Cloud Detection and Characterization Characterization Cloud Albedo Cloud Albedo N/A Cloud Top Height (CTH) and Cloud Base Height (CBH) Aerosol Top Height (ATH) and Aerosol Base Height (ATH) above clouds; MERRA-2 to define ATH and ABH below clouds Vertical distribution of We use MERRA-2 (section M/A CER, COT) (section 2.1.1) Computed for RRTMG bands (25) using Mie calculations and DISORT N/A CALIOP _{vfm} to define CTH; N/A N/A N/A N/A N/A | Model | KKTWO-5W | (2021) | | | | |
| Characterization (see Table 3); MODIS _{Cloud} to assign cloud properties (i.e., CWP, CER, COT) (section 2.1.1) Computed for RRTMG bands (25) using Mie calculations and DISORT Cloud Top Height (CTH) and Cloud Base Height (CBH) CALIOP _{vfm} to define CTH; CBH = CTH - 500m CALIOP _{vfm} to define ATH above clouds and ATH and ABH in non-cloudy skies; ABH = CTH above clouds; MERRA-2 to define ATH and ABH below clouds Vertical distribution of We use MERRA-2 (section N/A | | CALIOP _{vfm} and MODIS _{Cloud} to | select qualifying clouds and to | | | | |
| Cloud Albedo N/A Cloud Top Height (CTH) and Cloud Base Height (CBH) CALIOP _{vfm} to define CTH; CBH = CTH - 500m CALIOP _{vfm} to define ATH above clouds and ATH and ABH in non-cloudy skies; ABH = CTH above clouds; MERRA-2 to define ATH and ABH below clouds Vertical distribution of We use MERRA-2 (section N/A Computed for RRTMG bands (25) using Mie calculations and DISORT N/A N/A | Cloud Detection and | define thick, broken and/ or thin c | clouds in atmospheric scenarios | | | | |
| Cloud Albedo N/A (25) using Mie calculations and DISORT Cloud Top Height (CTH) and Cloud Base Height (CBH) CBH = CTH - 500m CALIOP _{vfm} to define CTH; N/A CBH = CTH - 500m CALIOP _{vfm} to define ATH above clouds and ATH and ABH in non-cloudy skies; ABH = CTH above clouds; MERRA-2 to define ATH and ABH below clouds Vertical distribution of We use MERRA-2 (section N/A | Characterization | (see Table 3); MODIS _{Cloud} to assi | gn cloud properties (i.e., CWP, | | | | |
| Cloud Albedo N/A (25) using Mie calculations and DISORT Cloud Top Height (CTH) and Cloud Base Height (CBH) CALIOP _{vfm} to define CTH; CBH = CTH - 500m CALIOP _{vfm} to define ATH above clouds and ATH and ABH in non-cloudy skies; ABH = CTH above clouds; MERRA-2 to define ATH and ABH below clouds Vertical distribution of We use MERRA-2 (section N/A | | CER, COT) (se | ection 2.1.1) | | | | |
| Cloud Top Height (CTH) and Cloud Base Height (CBH) CALIOP _{vfm} to define CTH; CBH = CTH - 500m CALIOP _{vfm} to define ATH above clouds and ATH and ABH in non-cloudy skies; ABH = CTH above clouds; MERRA-2 to define ATH and ABH below clouds Vertical distribution of We use MERRA-2 (section N/A | | | Computed for RRTMG bands | | | | |
| Cloud Top Height (CTH) and Cloud Base Height (CBH) CALIOP _{vfm} to define CTH; CBH = CTH - 500m CALIOP _{vfm} to define ATH above clouds and ATH and ABH in non-cloudy skies; ABH = CTH above clouds; MERRA-2 to define ATH and ABH below clouds Vertical distribution of We use MERRA-2 (section N/A | Cloud Albedo | N/A | (25) using Mie calculations | | | | |
| Aerosol Top Height (ATH) and Aerosol Base Height (ABH) CALIOP _{vfm} to define CTH; CBH = CTH - 500m CALIOP _{vfm} to define ATH above clouds and ATH and ABH in non-cloudy skies; ABH = CTH above clouds; MERRA-2 to define ATH and ABH below clouds Vertical distribution of We use MERRA-2 (section N/A | | | and DISORT | | | | |
| Aerosol Top Height (ATH) and Aerosol Base Height (ABH) CALIOP _{vfm} to define ATH above clouds and ATH and ABH in non-cloudy skies; ABH = CTH above clouds; MERRA-2 to define ATH and ABH below clouds Vertical distribution of We use MERRA-2 (section N/A | Cloud Top Height (CTH) | CALIOD . to define CTU | | | | | |
| CALIOP _{vfm} to define ATH above clouds and ATH and ABH in non-cloudy skies; ABH = CTH above clouds; MERRA-2 to define ATH and ABH below clouds Vertical distribution of We use MERRA-2 (section N/A | and Cloud Base Height | · | N/A | | | | |
| Aerosol Top Height (ATH) and Aerosol Base Height (ABH) CTH above clouds; MERRA-2 to define ATH and ABH below clouds Vertical distribution of We use MERRA-2 (section N/A | (CBH) | CBH = C1H - 300m | | | | | |
| Aerosol Top Height (ATH) and Aerosol Base Height (ABH) CTH above clouds; MERRA-2 to define ATH and ABH below clouds Vertical distribution of We use MERRA-2 (section N/A | | CALIOP _{vfm} to define ATH | | | | | |
| in non-cloudy skies; ABH = (ATH) and Aerosol Base Height (ABH) CTH above clouds; MERRA-2 to define ATH and ABH below clouds Vertical distribution of We use MERRA-2 (section N/A | A awasal Tan Hainht | above clouds and ATH and ABH | | | | | |
| Height (ABH) CTH above clouds; MERRA-2 to define ATH and ABH below clouds Vertical distribution of We use MERRA-2 (section N/A | | in non-cloudy skies; ABH = | NT/A | | | | |
| to define ATH and ABH below clouds Vertical distribution of We use MERRA-2 (section N/A | | CTH above clouds; MERRA-2 | N/A | | | | |
| Vertical distribution of We use MERRA-2 (section N/A | Height (ABH) | to define ATH and ABH below | | | | | |
| N/A | | clouds | | | | | |
| spectral ASY and SSA 2.1.1) | Vertical distribution of | We use MERRA-2 (section | NT/A | | | | |
| | spectral ASY and SSA | 2.1.1) | N/A | | | | |
| Below clouds, we use MERRA-2; elsewhere (above clouds and | | Below clouds, we use MERRA-2 ; elsewhere (above clouds and | | | | | |
| Vertical distribution of non-cloudy sky), MERRA-2 normalized spectral aerosol | Vertical distribution of | Vertical distribution of non-cloudy sky), MERRA-2 normalized spectral aerosc | | | | | |
| spectral aerosol extinction extinction coefficient is multiplied by CALIOP AOD at 532nm. | spectral aerosol extinction | n extinction coefficient is multiplied by CALIOP AOD at 532nm. | | | | | |
| coefficient Table A3 describes how CALIOP AOD is chosen to be | coefficient | Table A3 describes how CALIOP AOD is chosen to be | | | | | |
| CALIOP _{ACAOD_standard} , CALIOP _{ACAOD_DR} , CALIOP _{AOD_standard} and/ | | CALIOP _{ACAOD_standard} , CALIOP _{ACAOD_DR} , CALIOP _{AOD_standard} and/ | | | | | |

| Diurnal cycle of aerosols | or CALIOP _{ODAOD} in different atmospheric scenarios. Figure 1 illustrates how we combine satellite and model data. | | | | | |
|---|--|--|--|--|--|--|
| and clouds | We only vary Solar Zenith Angles (SZAs), assuming constant aerosol and cloud properties during the day | | | | | |
| Atmospheric composition, weather and ocean surface winds(*) | We use MERRA-2 (section 2.1.1) | | | | | |
| Ocean Surface BRDF | Cox-Munk BRDF [Jin et al., 2011] with Chlorophyl concentration = 0.2 g/m ³ | Standard Lambertian with an albedo value of 0.03 | | | | |
| ΔDARE calculation | Compute upper and lower bounds using uncertainties listed in Table 4 | N/A | | | | |

Table 2: Two different DARE calculations (i.e., semi-observational DARE_obs described in section 2.1, and parametrized DARE_param described in section 2.2) in our study and their respective inputs. RRTMG-SW stands for Short-wave Rapid Radiative Transfer Model. See Table 1 for a description of CALIOP $_{ACAOD_standard}$, CALIOP $_{ACAOD_DR}$, CALIOP $_{ACAOD_DR}$, CALIOP $_{ODAOD}$, CALIOP $_{ODAOD}$, CALIOP $_{ODAOD}$, MODIS $_{Cloud}$ and MERRA-2. (*) These parameters are assumed constant along the satellite track: CO $_2$ volume mixing ratio = 400 ppmv, N $_2$ O mass density = 0.3 ppmv, and CH $_4$ mass density = 1.7 ppmv. O $_2$ mass density, which is also a required input to RRTMG, is assumed to be 0.0 kg m $_3$. Ocean surface wind variability along the satellite track is provided by MERRA-2. The profiles of temperature, pressure, air density (calculated from pressure and temperature), water vapor, and O $_3$ vary along the satellite track and are also provided by MERRA-2.

To estimate DARE_obs in section 2.1, we perform solar broadband radiative transfer (RT) calculations using the Shortwave Rapid Radiative Transfer Model for General Circulation Model (GCM) applications (RRTMG-SW) RT code (hereafter, only called RRTMG) (Clough et al., 2005; Iacono et al., 2008) (see Table 2). In RRTMG, gaseous absorption is treated using the correlated-k approach (Mlawer et al., 1997); the delta-Eddington (Joseph et al., 1976) two-stream approximation (Meador and Weaver, 1980; Oreopoulos and Barker, 1999) is used for scattering calculations. Therefore, RRTMG does not need information on the aerosol phase function, which is why we only use ASY as input. Broadband solar fluxes are calculated from 14 broadbands with bandwidths ranging from 0.2 to 12.0 μm. The four SW RRTMG broadband channels are between 345-442, 442-625, 625-778 and 778-1242 nm. As listed in Table 2, inputs for RRTMG include the optical properties of aerosol and cloud, atmospheric profiles, ocean surface BRDF and Solar Zenith Angle (SZA) information. In RRTMG (using two-stream approximation), total fluxes have an accuracy within 1-2 W·m⁻² relative to the standard RRTM-SW (using DISORT) in non-cloudy skies and

within 6 W·m⁻² in cloudy skies. RRTM-SW with DISORT itself is accurate to within 2 W·m⁻² of the data-validated multiple scattering model, CHARTS (https://github.com/AER-RC/RRTMG_SW) (Iacono et al., 2008).

173174175

176

177

172

The parametrization that allows us to compute DARE_param is described in section 2.2. It builds on a method that systematically links aircraft observations of SSFR-linked spectral fluxes to aerosol optical thickness and other parameters using nine cases from the 2016 and 2017 ORACLES campaigns. This observationally driven link is expressed by a parametrization of the shortwave broadband DARE in terms of the mid-visible AOD and scene albedo.

178179180

181 182 In this study, we compute both the instantaneous (or instant) DARE along the satellite track for a given location and time and an estimated diurnal average (or 24 h) DARE at the same location that accounts only for the varying solar zenith angle (SZA) throughout the day. We vary SZA corresponding to every hour at the same location and date, compute DARE and average all instant DARE to obtain 24 h DARE.

183 184 185

186 187

188

189

190

191

192

193

194

195

196 197

198

199

200

201202

203

204

2.1 Semi-Observational DARE_obs Calculations

To design the algorithm that computes DARE obs, we need to gain understanding of DARE obs sensitivities from idealized cases. To do that, we compute a theoretical-based cloudy DARE parameter (i.e., DARE theo) using RT calculations on several canonical atmospheric cases. Like Table 2 for DARE obs and DARE param, Table A1 in the appendix lists the input parameters to our DARE theo calculations. DARE theo is computed for two types of single low warm liquid clouds (i.e., COT=1, CER=12 and CWP=8 vs. COT=10, CER=12 and CWP=80) and varying vertical distributions of RRTMG "build-in" aerosol types (see Fig. A1) while keeping cloud heights, AOD, ASY, atmospheric composition, weather and ocean surface BRDF constant (see thirty-two canonical cases illustrated in panels a, b, c, and d of Fig. A2 where we vary the order and amount of two aerosol types over clouds in the vertical). No matter which type and which vertical distribution of aerosol above cloud is considered, DARE theo values are lower when aerosols are present above a cloud of COT equal to 1 (cases (e-b) and (e-d)), compared to a COT equal to 10 (cases (e-a) and (e-c) in Fig. A2). This is illustrated by changes of approximatively -7 to -1 W·m⁻² for (e-b) and (e-d) vs. approximatively 9 to 24 W·m⁻² for (e-a) and (e-c) of Fig. A2. We also record lower DARE theo values when adding more scattering aerosols (i.e., "continental" aerosol type) to already absorbing aerosols (i.e., "urban" aerosol type). In effect, DARE theo values drop from approximatively 24 to 14 W·m⁻² when aerosols are more scattering above a cloud of COT equal 10 (see C1-C4 in (e-a) vs. C5-C8 in (e-a) of Fig. A2). And DARE theo values drop from approximatively -1 to -5 W·m⁻² when aerosols are more scattering above a cloud of COT equal 1 (see C1-C4 in (e-b) vs. C5-C8 in (e-b) of Fig. A2). In conclusion, the variability of these DARE theo calculations confirm, as expected, that our semi-observational DARE obs calculations need to account for the vertical order and location of aerosol types and aerosol amount.

205206

207

As listed in Table 2, DARE_obs uses a mix of satellite and model products as input parameters to RRTMG. Section 2.1.1 describes these satellite and model products in further detail. Section 2.1.2 provides more information on how

these products are combined. Section 2.1.3 describes how we divide the atmosphere into four atmospheric scenarios along the satellite track. Section 2.1.4 describes the DARE obsuncertainty calculations.

2.1.1 Data

CALIOP flew onboard the CALIPSO platform for 17 years from 2006 to 2023. From launch in April 2006 until September 2018, CALIPSO flew in tandem with multiple other platforms as part of the A-Train constellation of Earth-observing satellites (Stephens et al., 2018). CALIOP measured high-resolution vertical profiles of attenuated backscatter coefficients (at 532 nm and 1064 nm) and volume depolarization ratios (at 532 nm) from aerosols and clouds in the Earth's atmosphere from the surface up to ~40 km. Full instrument details are given in Hunt et al. (2009). A succession of sophisticated retrieval algorithms is used to derive CALIOP Level 2 products from the Level 1 products (Winker et al., 2009). These retrieval algorithms are composed of a feature detection scheme (Vaughan et al., 2009), a module that first distinguishes cloud from aerosol (Liu et al., 2019) and then partitions clouds according to thermodynamic phase (Avery et al., 2020) and aerosols according to subtypes (Kim et al., 2018; Tackett et al., 2023), and, finally, an extinction algorithm (Young et al., 2018) that retrieves profiles of aerosol backscatter and extinction coefficients and the total column AOD based on modeled values of the extinction-to-backscatter ratio (also called lidar ratio) inferred for each detected aerosol layer subtype.

Previous studies have shown that CALIOP standard AOD products underestimate AOD in non-cloudy skies (Kacenelenbogen et al., 2011; Thorsen et al., 2017; Toth et al., 2018) and above clouds (e.g., Kacenelenbogen et al., 2014, Rajapakshe et al., 2017), mostly because CALIOP does not detect tenuous aerosol layers having attenuated backscatter coefficients less than the CALIOP detection threshold (Rogers et al., 2014). The low biases in the total column and above cloud AODs, denoted in this work as, respectively, CALIOPAOD standard and CALIOPACAOD standard (see Table 1; AC stands for Above Cloud), motivates us to also use two new, independently derived estimates of column optical depth at 532 nm. The first of these uses the depolarization ratio (DR) method developed in Hu et al. (2007), hereafter called CALIOPACAOD DR at 532 nm, to calculate total column optical depths above opaque water clouds. By leveraging the unique relationship between layer-integrated volume depolarization ($\delta_{\rm v}$) and the layereffective multiple scattering factor in opaque liquid water clouds (Hu et al., 2006), together with characteristic values of water cloud lidar ratios, an accurate estimate of the opaque water cloud integrated attenuated backscatter in noncloudy skies (γ'_{clear}) can be obtained (Platt, 1973). The two-way transmittance due to aerosols above the cloud (and hence above cloud optical depth) is thus obtained by dividing the measured cloud integrated attenuated backscatter, $\gamma'_{\text{measured}}$, by the γ'_{clear} estimate. As of CALIOP's version 4.51 data release, CALIOPACAOD DR retrievals are now included as a standard scientific data set (SDS) contained in the layer products for all averaging resolutions. However, the individual components required for the DR method (e.g., $\delta_{\rm v}$ and $\gamma'_{\rm measured}$) were routinely reported in earlier data releases, and hence AODs derived using the DR method have been used extensively in previous studies (e.g., Chand et al., 2008; Liu et al., 2015; and Kacenelenbogen et al., 2019). Furthermore, comparisons made by Ferrare et al. (2017) show that CALIOPACAOD_DR agrees well (bias and RMS differences less than 0.05 and 10%) with coincident measurements by the NASA Langley Research Center airborne High Spectral Resolution Lidars (HSRL) during two

flights (18 and 20 of September 2016) of the ORACLES field campaign (Redemann et al., 2021). The second of CALIOP's independently derived total column AOD estimates is provided by the Ocean Derived Column Optical Depths (ODCOD) algorithm (Ryan et al., 2024), hereafter called CALIOPODAOD at 532 nm. As with the DR method estimates, the ODCOD AOD is a new parameter reported for the first time in CALIOP's V4.51 data release. ODCOD works by comparing an idealized parameterization of laboratory measurements of the 532 nm detector impulse response function (IRF) to space-based measurements of the backscattered energy from the ocean surface. Similar in operation to the technique employed by Venkata and Reagan (2016), the ODCOD algorithm shifts the IRF model in time and scales it in magnitude to achieve the best fit to the measured data. When weighted by surface wind speed, the area under the curve of this shifted and scaled model is directly related to the attenuation of the laser surface return by the intervening atmosphere. Note that both ODCOD and the DR method report effective optical depths; that is, the product of the true overlying optical depths and a column-effective multiple scattering factor, η_{col} , where $0 < \eta_{col} \le$ 1. Because ODCOD AODs are retrieved immediately after executing the CALIOP surface detection algorithm, and prior to conducting a search for atmospheric layers, no attempt is made to separate multiple scattering and single scattering contributions made by the overlying particulates (i.e., clouds and/or aerosols). Fortunately, in cloud-free columns containing only aerosol layers, $\eta_{col} \approx 1$ (Young et al., 2018). Consequently, multiple scattering corrections are neglected in the standard extinction retrieval (Winker et al., 2009) and considered unnecessary in the ODCOD analyses. The extensive comparisons shown in Ryan et al. (2024) demonstrate that CALIOPODAOD agrees well with coincident HSRL measurements during all CALIOP-HSRL co-located flights from 2006 to 2022. The median difference in the daytime between CALIOP_{ODAOD} and HSRL AOD is -0.037 ± 0.052 (-12 % ± 25%; N=149) with CALIOPODAOD lower and a correlation coefficient of 0.775.

In our study, as listed in Table 2, we use CALIOP to characterize aerosol optical depth above clouds (CALIOPACAOD_standard, CALIOPACAOD_DR) and in cloud-free skies (CALIOPACD_Standard, and CALIOPODAOD), to establish aerosol and cloud top heights (CALIOPvfm; VFM stands for Vertical Feature Mask), and as the source for the SZAs in our DARE_obs calculations. Table A3 describes how CALIOP AOD is chosen to be equal to CALIOPACAOD_standard, CALIOPACAOD_DR, CALIOPACD_Standard and/ or CALIOPODAOD in different atmospheric scenarios (i.e., non-cloudy skies, or among thick and/or thin clouds present). We also use the latest CALIOP stratospheric aerosol profile product (version 1.00; Kar et al., 2019) to correct for attenuation by stratospheric aerosols in CALIOPACAOD_DR and CALIOPODAOD. To do that, we compute a zonal climatology of Stratospheric Aerosol Optical Depth (SAOD) from the equal-angle data product, then interpolate the zonal data to the latitude grid of the CALIPSO granule observations (see Fig. A3 in the appendix). Finally, we subtract the SAOD from CALIOPACAOD_DR and CALIOPODAOD. Note that while performing our DARE_theo calculations, we confirmed the importance of considering stratospheric aerosols. Adding stratospheric aerosols between 25-30 km with a typical AOD value of 0.04 in the stratosphere (Kloss et al., 2021) to tropospheric aerosols above clouds leads to an absolute difference in DARE_theo up to 3.7 W·m². We also use CALIOPvfm to select clouds of interest (i.e., single layer low warm liquid clouds) and to define thick, broken and/ or thin clouds in our four atmospheric scenarios described in section 2.1.3.

MODIS/Aqua flew as part of the A-Train constellation of satellites from 2002 until a final drag makeup satellite maneuver in December 2021, after which Aqua began a slow descent below the A-Train. MODIS has 20 shortwave spectral bands from 412 nm to 2130 nm, along with 16 infrared bands from 3.7 to 14.4µm, enabling retrievals of the macrophysical, microphysical and radiative properties of clouds. CER commonly is retrieved simultaneously with COT from passive imager remote sensing observations using a bi-spectral technique (Nakajima and King, 1990; Platnick et al., 2003) pairing a non-absorbing visible or near-infrared spectral channel sensitive to COT with an absorbing shortwave infrared or mid-wave infrared spectral channel sensitive to CER. In this paper, we use two types of cloud products from MODIS (referred to as MODIScloud in Table 1). The first type of MODIScloud product is from the current operational algorithm and does not account for the presence of aerosols above clouds (Meyer et al., 2013). These are called uncorrected MODIScloud products in this paper and are derived from the Cross-platform HIgh resolution Multi-instrument AtmosphEric Retrieval Algorithms (CHIMAERA) shared-core suite of cloud algorithms (Wind et al., 2020). This suite of algorithms includes cloud optical/microphysical properties (e.g., thermodynamic phase, optical thickness, particle effective size, water path) and cloud-top property retrievals from MODIS/Visible Infrared Imaging Radiometer Suite (VIIRS) CLDPROP Version-1.1, designed to sustain the long-term records of MODIS (cloud properties continuity product) (Platnick et al., 2021). The second type of MODIS_{Cloud} product derives from a new retrieval technique that corrects the MODIS cloud retrievals by accounting for overlying aerosols. In this paper these are called corrected MODIScloud products in this paper. In Grosvenor et al. (2018), comparisons between MODIS and Advanced Microwave Scanning Radiometer 2 (AMSR2), which is not sensitive to the above-cloud aerosol, indicate derived cloud droplet number concentration differences of < 10 cm⁻³ over most of the Southeast Atlantic stratocumulus deck. As described in Meyer et al. (2015), what we call corrected MODIScloud in this paper was achieved by adding aerosols with prescribed scattering properties in the radiative transfer calculations that are used to construct bi-spectral lookup tables. Note that this correction is strongly dependent on the assumed aerosol scattering properties. For this study, these properties are derived from the NASA Spectrometers for Sky-Scanning Sun-Tracking Atmospheric Research (4STAR) observations obtained during ORACLES 2016. Since the cases we carefully selected for DARE obs also are during the deployment of ORACLES, we can assess the effects of using either corrected or uncorrected MODIScloud properties in DARE obs calculations (see section 2.1.4). The main cloud properties needed in the DARE obs calculations are CWP, CER and COT (see Table 2).

308 309 310

311

312

313

314

315

316

317

318

282

283

284

285

286

287

288

289

290

291

292 293

294

295

296

297

298

299

300

301

302

303

304

305

306

307

Regardless of the cloud product used, validating retrievals such as COT, CER, and CWP is difficult, as there are no direct measurements of these radiative quantities. Microphysical retrievals can be compared against airborne *in-situ* cloud probes, and previous investigations have found notable differences, though strong correlation, between the two, with MODIS-derived CER on average more than 2µm larger than that derived from legacy *in-situ* probes (e.g., Nakajima et al., 1991; Platnick and Valero, 1995; Painemal and Zuidema, 2011; Min et al., 2012; King et al., 2013; Noble and Hudson, 2015; Gupta et al., 2022). Other studies using probes leveraging different observation techniques (e.g., Witte et al., 2018) have shown no systematic differences in CER. Comparisons against other retrieval techniques, such as polarimetry, can also inform on CER retrieval quality. Using ORACLES airborne observations, Meyer et al., (2025) performed an extensive comparison of spectral imager liquid CER retrievals (from the Enhanced MODIS

Airborne Simulator, eMAS, an airborne proxy instrument of MODIS, and the Research Scanning Polarimeter, RSP) with those from polarimetry (from RSP) and CER derived from two *in-situ* cloud probes. Agreement between the imager, polarimetric, and probe-derived CER, was found to be case- and spectral-dependent, and accounting for above-cloud aerosol absorption in the bi-spectral imager retrievals (equivalent to using corrected MODIS_{cloud}) either has no impact or worsens the agreement depending on the spectral channel used. In section 2.1.4, we demonstrate that correcting cloud properties for aerosol above them leads to insignificant differences in mean instant DARE_obs values (up to 4 W.m⁻²) for all three case studies.

325326327

328

329

330

331

332

333

334

335

336

337

338

339

340

341

342

343

344

345

346

347

348

349

350

351

352

353

354

355

319

320

321

322

323

324

Like other papers (e.g., Su et al., 2013), and because satellites are not yet well suited to broadly observe the vertical profile of aerosol intensive properties, we use NASA's Global Modeling and Assimilation Office (GMAO) MERRA-2 to complement satellite observations. MERRA-2 data became available in September 2015 (Gelaro et al., 2017), covering 1980 - Present. It is based on a version of the GEOS-5 atmospheric data assimilation system that was frozen in 2008 and was produced on a 0.5 x 0.625° grid (~55 km x 69 km) on 72 hybrid sigma-pressure coordinate system vertical levels. It was frozen so that the underlying model physics, schemes, and data assimilation techniques are the same for the duration of the MERRA-2 reanalysis. It uses a version of the Goddard Chemistry Aerosol Radiation and Transport (GOCART) model (Chin et al., 2002, Colarco et al., 2010, Colarco et al., 2014) to treat the emission, transport, removal, and chemistry of dust, sea salt, sulfate, and carbonaceous aerosols. Aerosol optical properties are computed from the Mie theory based Optical Properties of Aerosol and Cloud (OPAC) dataset (Hess et al., 1998), except for dust, which were derived by an observation-derived dataset of refractive indices and an assumption of a spheroidal shape as described in Colarco et al. (2014). MERRA-2 assimilates satellite, air, and ground observations (Randles et al., 2017) to constrain both the atmospheric and aerosol state in the model. MERRA-2 also provides optical properties within the SW RRTMG broadband channels. As listed in Table 2, our DARE obscalculations use MERRA-2 (GMAO, 2015) ocean surface winds, ozone, temperature, pressure, air density, and water vapor profiles, and aerosol intensive properties (i.e., spectral extinction coefficient, SSA, ASY) above and below low opaque water clouds and in non-cloudy skies. We use CALIOP AOD quantities at 532 nm and we populate the 442-625nm RRTMG channel with an observational AOD value. We then spectrally extrapolate the AOD at 532 nm in the other broadband RRTMG channels of the short-wave part of the spectrum using the MERRA-2 spectral shape of extinction coefficients as further described in section 2.1.2. Many papers have shown that MERRA-2 aerosol extensive, and intensive properties and horizontal/vertical distribution are far from perfect (e.g., Nowottnick et al., 2015). For example, GEOS aerosol Single Scattering Albedo (SSA) was shown to be consistently higher than in-situ measurements during the ORACLES field campaign, explained by an underestimation of BC content by the GEOS model (Das et al., 2024). We expect, according to the DARE theo calculations illustrated in Fig. A2, that a high bias in the MERRA-2 estimated SSA, if not compensated by other factors, would cause a low bias in DARE obs calculations (see, for example, lower DARE theo values in (e-a) for C5-C8 where SSA is higher compared to higher DARE theo values in (e-a) for C1-C4 where SSA is lower). As CALIOP cannot reliably provide any aerosol information below clouds due to signal attenuation, we also use MERRA-2 to inform on aerosol extensive, intensive properties and layer heights below clouds.

Finally, we must assume a consistent observed and modeled extinction coefficient threshold under which we consider there is no aerosol present in the atmosphere. Based on Rogers et al. (2014), we consider that there are no aerosols (and hence DARE_obs = 0) if the CALIOP extinction coefficient at 532 nm is below 0.07 km⁻¹. As the lower threshold on the CALIOP extinction of 0.07 km⁻¹ is based on an aerosol layer that is 1.5 km thick in Rogers et al. (2014), we impose a lower threshold on MERRA-2 extinction of 0.014 km⁻¹ in the 442-625 nm RRTMG broadband channel. This is because the MERRA-2 layers are, on average, 0.29 km thick in September 2016 in a MERRA-2 grid box located at [-10°W-10°E, -40°S-0°] and between 1-5 km altitude. In section 2.1.4, we demonstrate that adding or removing such a threshold on the aerosol extinction coefficient leads to insignificant differences in mean instant DARE_obs values (up to 0.8 W.m⁻²) for all three case studies.

2.1.2 Combination of Satellites and Model

In this subsection, we show how we combine the satellite products with modeled data to perform RT calculations that represents DARE_obs. As described in Table 2, on the one hand, MODIS and CALIOP satellites are used to detect and characterize clouds, define aerosol height, and provide aerosol extinction coefficients above clouds and in non-cloudy skies. MERRA-2, on the other hand, is used to define aerosol top and base heights below clouds and provide the vertical distribution of spectral ASY, SSA, and extinction coefficient above, below clouds and in non-cloudy skies, along with information about atmospheric composition, weather, and ocean surface winds. We emphasize that we use MERRA-2 aerosol and atmospheric data regardless of any MERRA-2 simulated clouds (i.e., we do not use MERRA-2 cloud simulations in any way), nor do we assess cloud agreement between MERRA-2 and satellite observations in this paper.

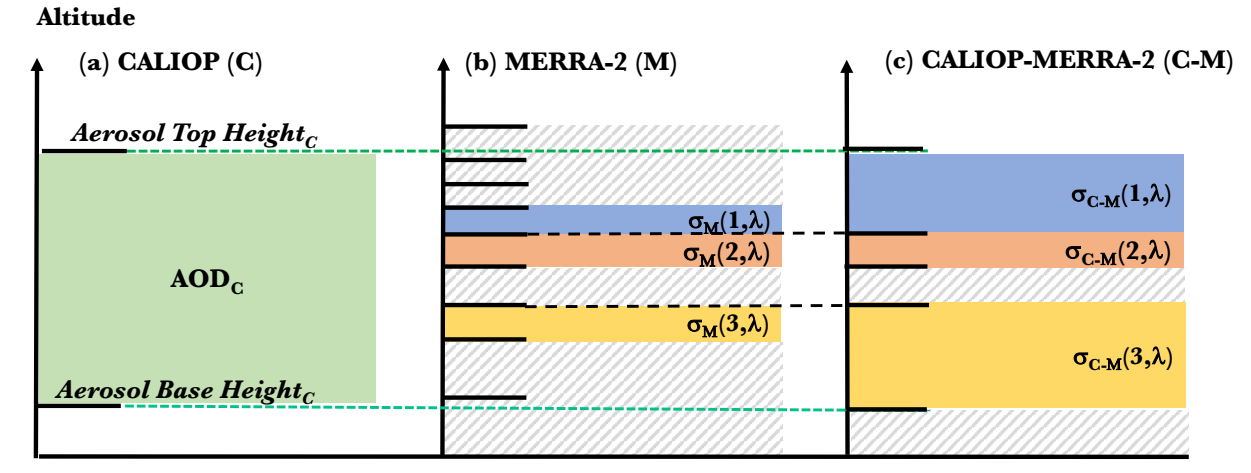
First, we collocate MODIS and CALIOP satellite observations every 1 km horizontally along CALIOP's track using the method described in Nagle and Holz (2009). By doing this we account for the parallax effect, i.e., the cloud top height dependence on spatial colocation. Using a simple surface collocation method that does not account for the parallax effect could result in a horizontal shift of more than 5 pixels (Holz et al., 2008).

Second, to compute DARE_obs, we need to combine aerosol extensive properties primarily obtained from CALIOP with aerosol intensive properties primarily obtained from MERRA-2. Figure 1 illustrates the combination of CALIOP and MERRA-2 products above clouds and in non-cloudy skies. In the green region in Fig. 1a, we assume one or multiple aerosol layer(s) of different aerosol types contained between the uppermost CALIOP-informed aerosol top and the lowermost CALIOP-informed aerosol base heights. The AOD at 532 nm, corresponding to the vertical integration of the extinction coefficients of these single or multiple aerosol layers, is obtained from CALIOP (called AODc) on Fig. 1 (i.e., either CALIOPACAOD_standard, CALIOPACAOD_DR, CALIOPACAOD_standard or CALIOPODAOD -- see Table 1). The illustrative MERRA-2 profile in Fig. 1b collocated in space and time with the profile in Fig. 1a shows three aerosol layers in blue, orange and yellow on an initial (and uneven) MERRA-2 vertical grid. It also shows six "aerosol-free" MERRA-2 aerosol layers in hashed grey (i.e., aerosol layers for which MERRA-2 extinction coefficients are below 0.014 km⁻¹ in the 442-625nm RRTMG broadband channel). We call L, the number of MERRA-

2 aerosol layers (L=3 in Fig. 1b). In each vertical layer, i, and for each RRTMG broadband channel, λ , we record the MERRA-2 extinction coefficient, $\sigma_M(i,\lambda)$, MERRA-2 SSA, $SSA_M(i,\lambda)$, and MERRA-2 ASY, $ASY_M(i,\lambda)$ in Fig. 1b. To combine CALIOP and MERRA-2 (Fig. 1c), we keep L constant and do not allow "aerosol-free" layers (hashed grey) to physically touch either the CALIOP-inferred aerosol top and aerosol base heights. Combined CALIOP and MERRA-2 (C-M) $SSA_{C-M}(i,\lambda)$ and $ASY_{C-M}(i,\lambda)$ are respectively equal to MERRA-2 $SSA_M(i,\lambda)$, and $ASY_M(i,\lambda)$. The combined CALIOP and MERRA-2 extinction coefficients, $\sigma_{C-M}(i,\lambda)$, is computed as in Eq. 2:

$$\sigma_{C-M}(i,\lambda) = \left(\frac{AOD_C(532nm)}{L}\right) \times \left(\frac{\sigma_M(i,\lambda)}{\sigma_M(i,442-625nm)}\right)$$
 (2)

. . .



Aerosol Layers:

 $\begin{aligned} & \mathbf{SSA_{M}}(1,\lambda), \mathbf{ASY_{M}}(1,\lambda) \\ & \mathbf{SSA_{M}}(2,\lambda), \mathbf{ASY_{M}}(2,\lambda) \\ & \mathbf{SSA_{M}}(3,\lambda), \mathbf{ASY_{M}}(3,\lambda) \end{aligned}$

No aerosol if $\sigma_{\rm M}$ < 0.014 km⁻¹

Figure 1: Illustration of how we combine MERRA-2 and CALIOP above clouds and in non-cloudy skies. In green in (a), we assume one or multiple aerosol layers contained between a CALIOP-inferred aerosol uppermost layer top height and aerosol lowermost base height. The AOD of the aerosol plume in green is informed by CALIOP at 532 nm, AOD_C. (b) is the MERRA-2 profile collocated in time and space to the CALIOP profile in (a). The MERRA-2 profile in (b) shows three aerosol layers (blue, orange and yellow) for which the MERRA-2 extinction coefficient, SSA, and ASY is respectively called $\sigma_M(i,\lambda)$, $SSA_M(i,\lambda)$, and $ASY_M(i,\lambda)$, in each layer i and in each broadband RRTMG channel λ . The combined CALIOP and MERRA-2 profile in (c) records $SSA_M(i,\lambda)$, $ASY_M(i,\lambda)$, and $\sigma_{C-M}(i,\lambda)$ as computed using Eq. 2.

2.1.3 DARE obs for Four Atmospheric Scenarios

Based on our theoretical calculations (see Table A1 and Fig. A2) and previous studies such as Matus et al. (2019), DARE results are clearly dependent on cloud thickness and cloud spatial homogeneity. To evaluate DARE, we generalize the atmospheric conditions into four scenarios based on different cloud conditions. In assembling our combined CALIPSO + MODIS data set, we start by removing records that report clouds of any types and at any altitudes above the single low warm liquid cloud (LWLC) that is closest to the Earth's surface (i.e., any clouds above a top height of 3 km). The first three scenarios show aerosol above and below different types of LWLC and the fourth scenario shows aerosol in (possibly cloud contaminated) non-cloudy skies. We define the geometrical thickness and spatial uniformity of LWLC using both CALIOP and MODIS cloud properties. Table 3 defines our nomenclature for different types of LWLC moving forward, how each type is characterized using CALIOP and MODIS data, and in which scenario they can be present.

| Fo | ur Atmospheric Scenario | S1 | S2 | S3 | S4 | | |
|-------------------------------------|--|-------------------|---|------------|----------------------|--|--|
| Single Lo | w Warm Liquid Cloud (LWLC) | Thick and uniform | Thick and broken Thin, and possibly broken | | Small or not present | | |
| Cloud | Number of cloud layer @ 1km using | | 1 | | <=1 | | |
| Conditions | CALIOP _{VFM} | | | | | | |
| | Cloud classification and cloud phase | I | Highly confider | nt | N/A | | |
| | identification @ 1km using | | | | | | |
| | CALIOP _{VFM} | | | | | | |
| | Number of single shot cloud detected | 3 | >= | =2 | <=2 | | |
| | within1km using CALIOP _{VFM} | | | | | | |
| | Number of single shot opaque flag | 3 | 2 | <=1 | <=2 | | |
| | within1km using CALIOP _{VFM} | | | | | | |
| | CALIOP _{VFM} shows consecutive | FAl | LSE | TRUE | FALSE | | |
| | single shot non-opaque clouds | | | | | | |
| | within1km | | | | | | |
| | CALIOP _{VFM} shows consecutive | TRUE FALS | | FALSE | FALSE | | |
| | single shot opaque clouds within1km | | | | | | |
| | MOD35 cloud mask @ 1km Bits 1-2 | N/A | | | 2 or 3 (i.e., | | |
| | "Unobstructed FOV confidence flag" | | | | "probably | | |
| | using MODIS _{Cloud} | | | | clear" or | | |
| | | | | | "clear") | | |
| | CLDPROP | > | 4 | < 4 | N/A | | |
| | (CLDPROP_L2_MODIS_Aqua) and | | | | | | |
| | CLDPROPOACAERO COT @ 1km | | | | | | |
| | using MODIS _{Cloud} | | | | | | |
| Synonyms and Main Features of LWLC: | | | | | | | |
| Thick | Opaque, non-transparent according to CALIOP and COT>4 according to MODIS | | | | | | |
| Thin | Non-opaque, semi-transparent, or transparent according to CALIOP and COT<4 according to | | | | | | |
| | MODIS | | | | | | |
| Uniform | Non-broken, homogeneous according to CALIOP (i.e., CALIOP detects three consecutive single | | | | | | |
| | shot clouds within a 1 km stretch) | | | | | | |
| Broken | Non-uniform, non-homogeneous acco | ording to CA | LIOP (i.e., C. | ALIOP does | not detect three | | |
| | consecutive single shot clouds within a | 1 km stretch) | | | | | |

- 426 Table 3: Method to distinguish single Low Warm Liquid Cloud (LWLC) in atmospheric scenario S1, S2, S3 and S4 using
- 427 MODIS_{Cloud} and CALIOP_{VFM} (see Table 1). For all scenarios, we collocate MODIS and CALIOP every 1km along the
- 428 CALIOP track using the method described in Nagle and Holz (2009); profiles are deleted if high clouds are present with
- 429 CALIOP cloud top height > 3km; clouds are "highly confident" when 111 > CALIOP Cloud-Aerosol Discrimination (CAD)
- 30 > 20; CALIOP cloud temperature > -10°C; CALIOP phase Quality Assurance ≥ 2; CALIOP cloud phase = 2.

- 432 Table A3 in the appendix describes which aerosol (derived from CALIOP and/ or MERRA) and cloud parameters
- 433 (derived from MODIS) were used and how these parameters were filtered to compute DARE obs in the case of S1,
- 434 S2, S3 and S4.

435

- We compute DARE_obs using the input parameters in Table 2 and for each 1 km stretch to which is attributed a
- particular atmospheric scenario in Table 3. We then regroup all these DARE_obs results along the track to obtain
- daily, and, eventually, regional, monthly, seasonal and/ or yearly DARE obs statistics.
- When clouds are present in the atmosphere, DARE obs of aerosol above clouds (i.e., DARE_{cloudy} for S1, S2, and S3
- combined) is the subtraction of upward fluxes for clouds without aerosols and for clouds with aerosols above them. If
- 441 we have N1 x S1, N2 x S2, and N3 x S3 cases along track, where NX represents the number of cases occurring for
- scenario SX, then we compute DARE_{cloudy} as follows:

$$DARE_{cloudy} = \frac{\sum_{i=1}^{N_1} DARE_{S_{1,i}} + \sum_{j=1}^{N_2} DARE_{S_{2,j}} + \sum_{k=1}^{N_3} DARE_{S_{3,k}}}{N_1 + N_2 + N_3}$$
(3)

- When clouds are absent in the atmosphere, DARE obs of aerosol in non-cloudy skies (i.e., DARE_{non-cloudy} for scenario
- S4) is the subtraction of upward fluxes for non-cloudy skies without aerosols and non-cloudy skies with aerosol
- present. If we have N4 x S4 cases, we compute DARE_{non-cloudy} as follows:

$$DARE_{non-cloudy} = \frac{\sum_{l=1}^{N4} DARE_{S4,l}}{N4}$$
 (4)

- 448 To be consistent with the assumptions in the RT used for the MODIS COT retrieval (i.e., MODIS assumes CF=1 to
- 449 retrieve COT), we assign MODIS CF values of 1 for S1, S2, and S3 and 0 for S4. Finally, we compute DARE in all
- sky conditions (DARE_{all-sky} for scenario S1, S2, S3 and S4) as follows:

$$DARE_{all-sky} = \frac{DARE_{cloudy} \times (N1+N2+N3) + DARE_{non-cloudy} \times N4}{N1+N2+N3+N4}$$
(5)

452453

2.1.4 DARE obs Uncertainties

- We vary AOD, CWP, SSA, ASY and surface albedo according to their uncertainties in our DARE_obs calculations
- 455 to obtain the DARE obsuncertainties. Table 4 describes the assumed or computed uncertainties used on these five
- input parameters to DARE obs.

| Variable | Uncertainty |
|---|--------------------------|
| CALIOP _{ACAOD_standard} , CALIOP _{AOD_standard} or CALIOP _{ACAOD_DR} | Computed using Eq. (6-7) |

| CALIOP _{ODAOD} | 0.11(Ryan et al., 2024) | | | | |
|----------------------------|---|--|--|--|--|
| MODIS _{Cloud} CWP | Reported at pixel-level (Platnick et al., 2021) | | | | |
| MERRA-2 SSA | 0.05 (e.g., Jethva et al., 2024) | | | | |
| MERRA-2 ASY | 0.02 (e.g., Kassianov et al., 2012) | | | | |
| Surface Albedo | 0.01 (Jin et al., 2011) | | | | |

Table 4: Input uncertainties on AOD, CWP, SSA, ASY and surface albedo used in our DARE_obs uncertainty calculation. See Table 1 for definition of CALIOPACAOD_standard, CALIOPACAOD_DR, MODISCloud and MERRA-2 and Table 2 on how these input parameters are used to computed DARE obs.

mean μ over a 20km stretch as follows:

Regarding uncertainties on the AOD values, we use Eq. 6 and 7 described below to compute an uncertainty on CALIOP_{ACAOD_standard}, CALIOP_{ACAOD_standard} and CALIOP_{ACAOD_DR} for each 20km stretch. We assume a gaussian distribution of N single-shot samples x₁, ..., x_N (e.g., CALIOP_{ACAOD_standard}, CALIOP_{AOD_standard} or CALIOP_{ACAOD_DR}) with each sample x_i recording a single shot uncertainty σ_i reported by the CALIOP team. We compute a weighted

$$\mu = \frac{\sum_{i=1}^{N} \left(\frac{x_i}{\sigma_i^2}\right)}{\sum_{i=1}^{N} \left(\frac{1}{\sigma^2}\right)}$$

$$\tag{6}$$

where the weighting factor is the inverse square of the error, $1/\sigma_i^2$. Note that the smaller the uncertainty, the larger the weight and vice-versa. The error on the weighted mean can be computed as follows:

470
$$\sigma^2(\mu) = \frac{1}{\sum_{i=1}^{N} \left(\frac{1}{\sigma_i^2}\right)}$$
 (7)

(Bevington and Robinson, 1992). When filtering for ocean surface wind speeds between 3 and 15 m.s⁻¹ in Ryan et al., (2024), CALIOP_{ODAOD} values have an averaged uncertainty of \sim 0.11 \pm 0.01 (75 % \pm 37 % relative) day and night. This uncertainty is mostly due to ocean surface wind speed. In our study, we average CALIOP_{ODAOD} over 20km stretches, for which the ocean surface wind speed remains constant because we use MERRA-2 with a horizontal resolution of \sim 55km. Therefore, in our study, we use a constant value of 0.11 for the averaged uncertainty on CALIOP_{ODAOD}. We use reported uncertainties at the pixel-level on CWP (Platnick et al., 2021). As for uncertainties on the aerosol intensive properties, we use an uncertainty of 0.05 for SSA and 0.02 for ASY. The averaged SSA uncertainty of 0.05 is inspired by Jethva et al. (2024), who developed a novel synergy algorithm that combines direct airborne measurements of above-cloud aerosol optical depth and the TOA spectral reflectance from Ozone Monitoring Instrument (OMI) and MODIS sensors. It shows, in its Table 3, a maximum absolute uncertainty of -0.054 in the retrieved near-UV SSA for an error of \sim 40 % (underestimation) in ACAOD results. The averaged ASY uncertainty of 0.02 is inspired by figure 9 in Kassaniov et al. (2012), who investigate the expected accuracy of 4STAR. It describes the relative difference between "true" and retrieved values of ASY for four selected days and shows a maximum of \sim 40.02 uncertainty for ASY at 1.02 µm, which becomes smaller at shorter wavelengths. Finally, we assume an averaged uncertainty of 0.01 in the surface albedo, inspired by figure 10 in Jin et al., (2011) in which they find a

standard deviation of ~0.01 between measured and parameterized broadband shortwave albedo for two years (2000-

487 2001).

488

For each one-km stretch, we compute DARE_obs using the uncertainty ranges of each variable (see Table 4), compute upper and lower bounds for DARE obs and then combine these values to get the DARE obs uncertainty.

491

- While designing our algorithm, we have evaluated the effects of a few constraints in the computation of our final
- DARE obs results. The effects are identified by (E-1) through (E-6) in Table A3 and quantified in Table A4 in the
- appendix. We separate these effects in five categories the effects of (E-1) adding a lower threshold on extinction
- coefficients, (E-2) adding aerosol information below clouds, (E-3) spatially extending aerosol top height information,
- 496 (E-4) using AOD version 2 along track, (E-5) using AOD version 3 along the track and (E-6) using corrected clouds
- instead of uncorrected clouds for overlying aerosols.
- 498 Regarding categories (E-1), (E-2) and (E-3), the effects add up to a small N=10 1km-data points in Table A4 and lead
- 499 to a small difference in mean instant all-sky (S1-S4) DARE obs of maximum ~1.6 W·m⁻².
- Regarding categories (E-4) and (E-5), we have computed DARE obs using three AOD versions (we call these V1,
- V2 and V3 see Table A3) and have evaluated the differences it makes in the number of 1km-data points and in the
- 502 mean DARE obs values. The latitudinal evolution of AOD V1, V2, and V3 along the CALIOP track are illustrated in
- Fig. A4 in the appendix. Using AOD V2 instead of AOD V1, adds up to N=65 1km-data points in Table A4 and makes
- a difference in mean instant all-sky (S1-S4) DARE obs of maximum ~1.3 W·m⁻². Using AOD V3 instead of AOD
- V2, makes the most difference in mean instant all-sky DARE obs (i.e., up to 3.2 W·m⁻² difference in DARE obs on
- 506 08/13/2017).
- Regarding category (E-6), using corrected vs. uncorrected clouds paired with AOD >0.3 leads to a difference in mean
- instant above-thick cloud (S1) DARE obs values up to ~4.1 W·m⁻² on 09/20/2016 (comparison shown in more detail
- 509 in Fig. A5 and Table A5 in the appendix). Applying a correction to the clouds does not seem to matter much in our
- study regarding DARE obs or COT. We argue that this is likely due to the generally low AOD values on all three
- days. Note that we would probably notice a significant difference in DARE obs when clouds are corrected vs.
- uncorrected if we were to apply our DARE obs calculations to multiple years over the region of Southeast Atlantic.
- In the end, the effects of (E-1) through (E-6) all lead to small differences in DARE obs below a threshold of 6 W.m⁻
- 514 ², which represents the accuracy of total fluxes in overcast conditions when comparing RRTMG-SW with other
- radiative transfer schemes (such as RRTM-SW). We emphasize that the DARE_obs results in section 3 apply a lower
- threshold on the extinction coefficients (E-1), use aerosols below clouds (E-2), extend the ATH when possible (E-3),
- 517 use CALIOP-inferred AOD version 2, and use cloud properties from MODIS that are uncorrected for aerosols above
- 518 them (E-6).

519520

2.2 Parametrized DARE param Calculations

- 521 The DARE param (see Table 2) parametrization framework in this section was developed by Cochrane et al., (2021)
- 522 (see their Eq. (12)). It collectively used airborne observations from the ORACLES field campaigns over the Southeast

Atlantic in conjunction with DARE calculations to derive statistical relationship between a) DARE and b) aerosol and cloud properties. DARE param supports a minimal parametrization for the entire ORACLES campaign. Specifically, for a range of SZAs, within the Southeast Atlantic region and during ORACLES (nine cases from the 2016 and 2017 ORACLES deployments to be exact), it links a broadband instant DARE param estimate for typical biomass burning aerosols injected above an omnipresent stratocumulus deck and in non-cloudy skies to two driving parameters, which are (i) a measure of the AOD (i.e., in our study, a combination of CALIOPACAOD standard, CALIOPACAOD DR, CALIOPAOD standard, and CALIOPODAOD at 532 nm) and (ii) a measure of the albedo of the underlying surface (i.e., either clouds or the ocean surface). Cochrane et al., (2021) report that their DARE param possesses a 20% uncertainty (lower bound on DARE variability) and that this uncertainty is due to factors other than AOD and scene albedo, such as measurement uncertainty and spatial/temporal variability of the cloud and aerosol properties. Note that, had we had a satellite retrieval of SSA with minimal uncertainty, we could have reduced the uncertainty of DARE param by using the second parametrization in Cochrane et al., (2021) that requires SSA in addition to the AOD and the scene albedo. The advantage of DARE param is that it establishes a direct link between DARE and two driving parameters, and it circumvents the need for radiative transfer calculations, aerosol composition, aerosol and cloud top height, atmospheric profiles, or ocean surface wind information that are required to compute semi-observational DARE obs in our study (see Table 2). We emphasize that this parametrization only represents the relationship between DARE and aerosol and cloud properties as sampled over the ORACLES study region and during the ORACLES timeframe. Outside of this framework (i.e., other regions of the globe and other seasons), different aerosol and cloud types can alter the DARE to cloud and aerosol relationship. To our knowledge, there are no current plans to extend the parameterization behind DARE param to other times and regions of the globe. Consequently, we will not be able to assess global DARE obs results in future studies using DARE param. In section 3.3.1, we compare instant DARE obs and DARE param as a first way to evaluate our results.

544545

546

547

548

549

523

524

525

526

527

528

529

530

531

532

533

534

535

536

537

538

539

540

541

542

543

3 Results

First, we describe the atmospheric scenes during three suborbital ORACLES flights (section 3.1). Second, we analyze the temporal and spatial variability of aerosol, cloud properties, and all-sky DARE_obs during these suborbital flights (see section 3.2). Third, we evaluate DARE_obs results (section 3.3) using two methods – collocated DARE_param (section 3.3.1) and airborne SSFR upward spectral irradiance measurements (section 3.3.2).

550551

552

553

554

555

556557

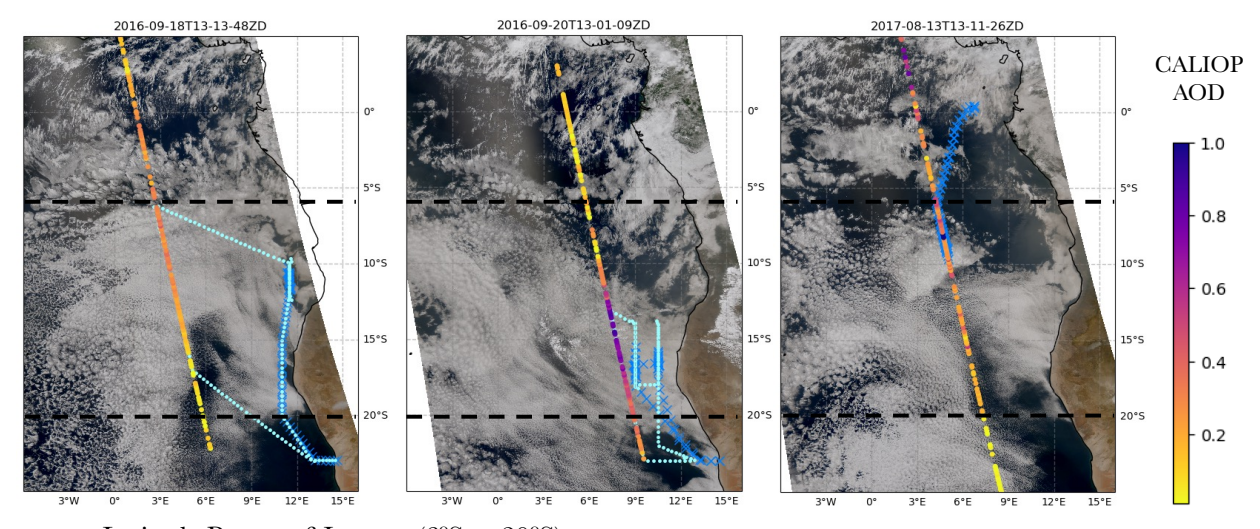
558

559

3.1 Suborbital Flights for Evaluation

Figure 2 illustrates our three case studies offshore from Namibia, South Africa. The MODIS RGB images in Fig. 2 show an omnipresent stratocumulus deck on all three days but a variability in cloud types along the CALIOP track (i.e., broken, uniform, thick and/ or thin – see Table 3). It also shows aerosol plumes of different loading on all three days with CALIOP AOD overlaid along the track from 0.01 (dark blue) to above 1 (dark red). On each day, both a high-flying plane focusing on remote sensing and low-flying plane focusing on *in-situ* sampling were deployed (Redemann et al. 2021). By 18 and 20 September 2016, strengthened westward free-tropospheric winds dispersed aerosol broadly over the stratocumulus deck, up to an altitude of 6.0 km (Redemann et al., 2021; Ryoo et al. 2022).

The highest aerosol loadings of ORACLES-2016 were recorded on 20 September (Pistone et al., 2019; Redemann et al., 2021). The highest AOD values (i.e., > 0.5) are clearly visible on 20 September 2016 in Fig. 2. The aerosol loadings reached maximums during the day, and diminished towards sunrise and sunset (Ryoo et al., 2022). The SSA is approximately 0.85 on 20 September 2016 at a wavelength of 500 nm, based on both in-situ and SSFR retrievals (Pistone et al. 2019). During 13 August 2017, the aerosol was located lower, within a drier (RH < 60%) layer with its top at 3 km, resting on top of a thinner cloud deck transitioning from overcast to broken. Smoke aerosol was also sampled in the boundary layer on 13 August 2017 (Zhang and Zuidema, 2019). The CALIOP track is well aligned with the high-altitude ER-2 aircraft (in light blue) on the two first days and with the lower-altitude P3 aircraft (in darker blue) on the third day, which was purposely achieved by flight plannings beforehand. Among the instruments flying onboard the ER-2, the HSRL-2, RSP and eMAS instruments are usually used to evaluate aerosol and cloud properties retrieved from CALIOP and/or MODIS. Note that we do not use measurements from these airborne instruments in this paper. Among the many instruments flying on board the P3 aircraft, our focus is on the Solar Spectral Flux Radiometer (SSFR) instrument (Pilewskie et al., 2003; Schmidt and Pilewskie, 2012) which we use to evaluate our DARE obs results in section 3.3.2. We remind the reader that in this paper, we use the observations, and the modeled parameters listed in Table 2 (i.e., MODIS for cloud microphysics, CALIOP for AOD, cloud and aerosol heights, MERRA-2 for aerosol intensive properties, atmospheric profiles and winds) to compute all-sky SW TOA DARE obs for each 1km stretch along the CALIOP track on each day.



− Latitude Range of Interest (6°S to 20°S)

MODIS RGB Rayleigh Scattering-Corrected Reflectance

ER-2 (high) Aircraft Track

560561

562

563

564

565

566

567

568

569

570

571

572

573

574

575

576

577

578 579

580

581

582

583

- P3 (low) Aircraft Track

Figure 2: Three case studies during ORACLES offshore from Namibia, South Africa on 09/18/2016, 09/20/2016, and 08/13/2017. The color bar shows AOD across the CALIOP/ CALIPSO flight tracks. The AOD is described under version 2 in Table A3 of the appendix. MODIS RGB Rayleigh scattering-corrected reflectance is in the background, together with ER-2 and P3 flight tracks in light and dark blue. 09/18/2016 and 09/20/2016 show satisfying colocation with the ER-2 aircraft. 08/13/2017 show satisfying colocation with the P3 aircraft.

Figure 3 illustrates the number of S1, S2, S3 and S4 scenarios along the tracks on all three days of Fig. 2 when focusing between 6°S and 20°S in latitude (see dashed horizontal black line on Fig. 2). We note a dominance of aerosol above thick clouds (S1), followed by unassigned (N/A) cases and lastly, non-cloudy skies (S4), aerosol above and below thick, thin and/ or broken clouds (S2 and S3).

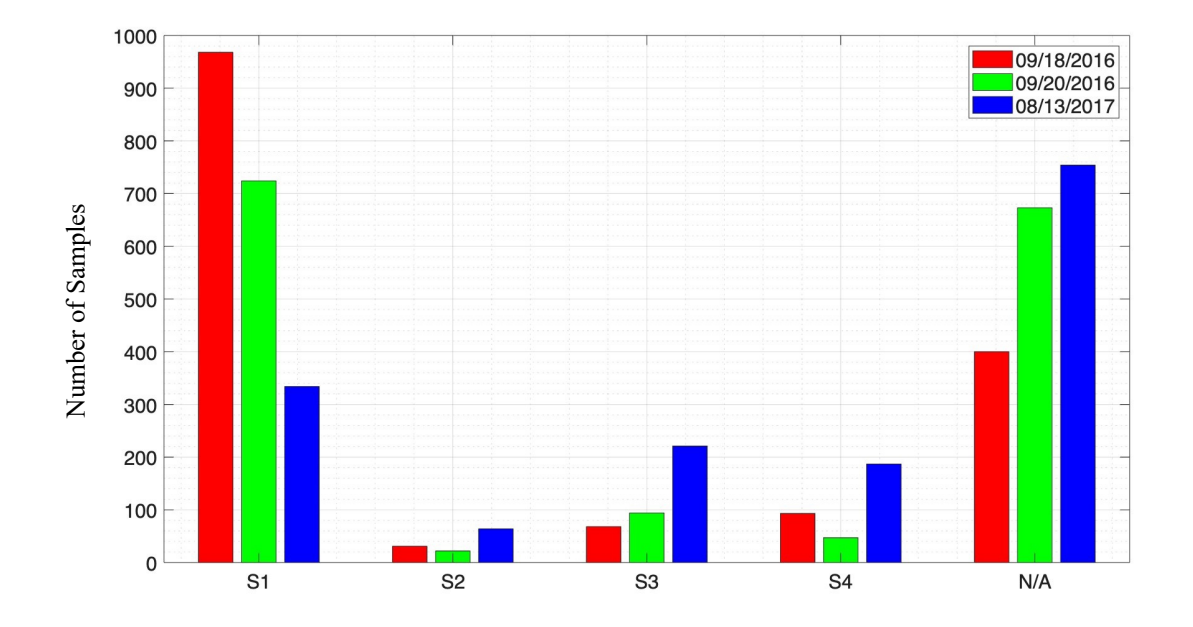


Figure 3: Number of S1-S4 samples on 09/18/2016, 09/20/2016 and 08/13/2017 (red, green, and blue) during ORACLES between 6°S and 20°S in latitude (see dashed horizontal black line on Fig. 2). S1: Thick and uniform cloud with MODIS COT>4; S2: Thick, can be broken cloud with MODIS COT>4; S3: Thin, can be broken cloud with MODIS COT<4; S4: Non-cloudy skies can contain small broken clouds (MODIS cloud mask = "clear"). See Table 3 for more details on S1-S4. N/A denotes the number of cases that were not assigned a scenario S1-S4 for various reasons (see reasons for these cases in the text)

Any scenario labelled "N/A" in Fig. 3 is a scenario that is not assigned to any of the S1 through S4 cases. These "N/A" scenarios constitute 26, 43, and 48% of the entire number of 1km profiles on, respectively, 09/18/2016, 09/20/2016 and 08/13/2017 (i.e., N=400, 673 and 754 compared to N=1560 from 6°S to 20°S). These scenarios could be unassigned in our study due to any of the following reasons:

- 604 (i) More than one cloud is present above a 3km altitude (e.g., cirrus clouds are present over LWLC).
- (ii) The cloud phase classification is unreliable (e.g., CALIOP either fails to classify the cloud as LWLC or insteadsuccessfully classifies the cloud as non-LWLC).
- (iii) The CALIOP and MODIS-based cloud characterization and/or non-cloudy sky determination report conflicting
 results (e.g., (a) CALIOP identifies a "thick cloud" along the CALIOP track when MODIS identifies a cloud with
 COT < 4 within the same 1km pixel or (b) MODIS identifies mostly cloudy skies within the 1km pixel whereas
 CALIOP profiles suggest mostly non-cloudy skies).
- 611 (iv) CALIOP detects cloudy skies, but MODIS does not have a valid collocated COT retrieval.

3.2 Aerosol, Cloud Properties, and All-Sky DARE obs

Figure 4 shows the Probability Distribution Functions (PDFs) of the AOD above clouds (S1-S3), AOD in non-cloudy skies (S4), all-sky SSA, ASY and EAE (S1-S4) values of the aerosol layer at the highest altitude, COT, CWP and

CER of all clouds (S1-S3), and 24 h mean DARE_obs values for all three days (red, green and blue). Table 5 shows the mean values corresponding to the PDFs of Fig. 4 as well as other parameters such as DARE_obs, uncertainties on DARE_obs (instant and 24 h), uncertainties on CWP and AOD, CF, ATH and ABH. Table A6 in the appendix complements Table 5 by providing the same parameters for scenarios S1, S2 and S3 separately.

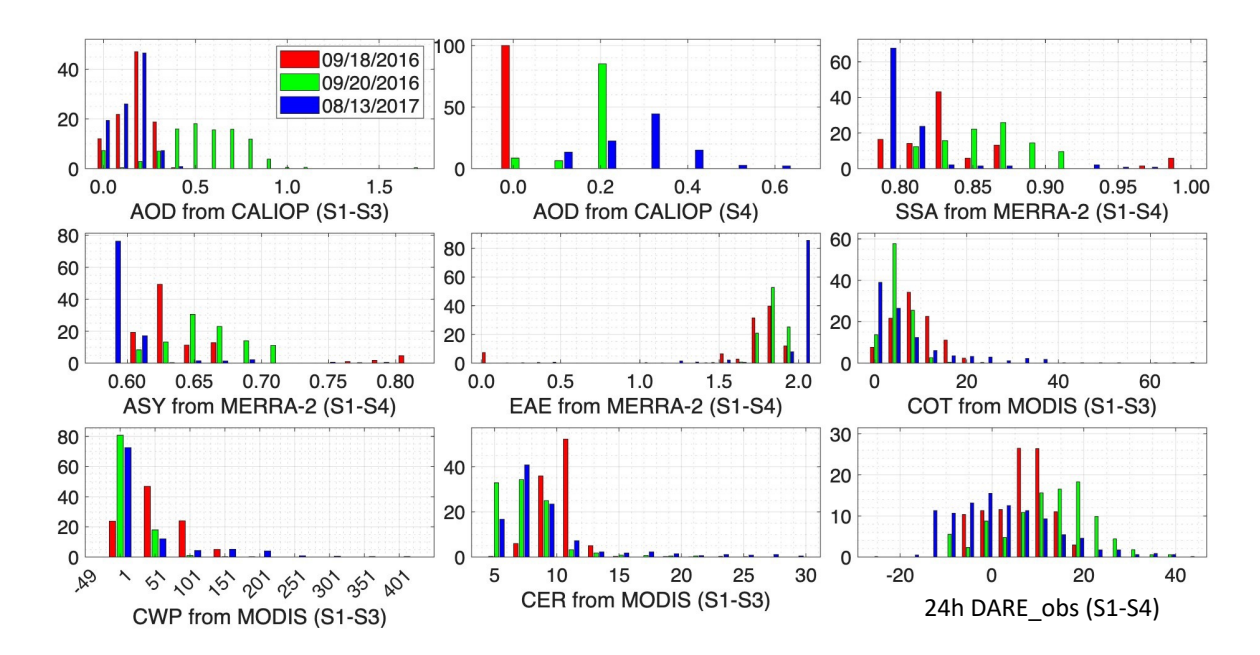


Figure 4: Probability distribution function of aerosol, cloud and 24 h mean DARE_obs properties on 09/18/2016, 09/20/2016 and 08/13/2017 (red, green, and blue) during ORACLES. Y-axis is the number of points in each bin. Table 5 shows the averaged values on each day in non-cloudy sky, cloudy and all-sky conditions. Cloud retrieved optical properties are not corrected for aerosols above them. Latitudes are selected between 6°S and 20°S. AOD is at 532 nm; SSA, ASY and 24h DARE_obs are in the 442-625 nm RRTMG channel; EAE is computed between the 442-625 nm and the 625-778 nm RRTMG channels; SSA, EAE and ASY are selected at the highest aerosol height in MERRA-2.

| | 9/18/16 | | | 9/20/16 | | | 8/13/17 | | |
|-----------------------|---------------------|--------------------|-----------------|---------------------|--------------------|-----------------|---------------------|----------------------|-----------------|
| Averaged Values | Non-cloudy sky (S4) | Cloudy sky (S1-S3) | All-sky (S1-S4) | Non-cloudy sky (S4) | Cloudy sky (S1-S3) | All-sky (S1-S4) | Non-cloudy sky (S4) | Cloudy Skies (S1-S3) | All-sky (S1-S4) |
| Number | 93 | 1067 | 1160 | 47 | 840 | 887 | 187 | 619 | 806 |
| DARE_obs 24 h | -2.4 | 9.4 | 8.4 | -6.4 | 15.5 | 14.3 | -8.9 | 7.9 | 4.0 |
| ΔDARE_obs 24 h | 0.3 | 0.1 | 0.1 | 0.4 | 0.1 | 0.1 | 0.2 | 0.2 | 0.1 |
| DARE_obs Instant | -5.1 | 22.5 | 20.3 | -15.6 | 36.9 | 34.2 | -22.6 | 19.2 | 9.5 |
| ΔDARE_obs Instant | 0.7 | 0.2 | 0.2 | 1.0 | 0.3 | 0.3 | 0.6 | 0.4 | 0.3 |
| СОТ | | 10.8 | | | 7.0 | | | 9.1 | |
| CWP | | 80.3 | | | 37.5 | | | 54.2 | |
| ΔCWP | | 0.5 | | | 0.5 | | | 1.1 | |
| CER | | 11.3 | | | 8.6 | | | 10.0 | |
| CALIOP CF | 0.05 | 0.99 | | 0.04 | 0.99 | | 0.01 | 0.97 | |
| MODIS CF | 0.04 | 0.99 | | 0.05 | 0.99 | | 0 | 0.93 | |
| AOD above clouds | | 0.2 | | | 0.6 | | | 0.2 | |
| AOD in non-cloudy sky | 0.1 | | | 0.2 | | | 0.3 | | |
| ΔΑΟD | 0.0 | 0.0 | | 0.0 | 0.0 | | 0.0 | 0.0 | |
| SSA | 1.0 | 0.8 | | 0.9 | 0.9 | | 0.8 | 0.8 | |
| ASY | 0.8 | 0.6 | | 0.7 | 0.7 | | 0.6 | 0.6 | |
| EAE | 0.2 | 1.9 | | 1.9 | 1.9 | | 2.0 | 2.0 | |
| Aerosol Top Height | 1.1 | 4.6 | | 3.5 | 5.1 | | 2.9 | 2.9 | |
| Cloud Top Height | | 1.0 | | | 0.7 | | | 1.0 | |

Table 5: Averaged DARE_obs values and corresponding averaged aerosol and cloud input values in the case of non-cloudy sky (S4), cloudy (S1-S3) and all-sky (S1-S4) scenarios. The all-sky (S1-S4) averaged values correspond to the PDFs in the lower right panel of Fig. 4. We display results corresponding to AOD version 2 (see Table A3 for more information on version 2). ΔSSA is fixed at 0.05 and ΔASY is fixed at 0.02 (see Table 4). Latitudes are selected between 6°S and 20°S. See Table A6 for a breakdown of cloudy skies (S1-S3) into S1, S2 and S3 scenarios separately. AOD is at 532 nm; SSA, ASY and 24h DARE_obs are in the 442-625 nm RRTMG channel; EAE is computed between the 442-625 nm and the 625-778 nm RRTMG channels; SSA, EAE and ASY are selected at the highest aerosol height in MERRA-2.

Figure 4 shows a variability of 24 h all-sky (S1-S4) DARE obs from -25 to 40 W·m⁻² on all three days (bottom right). It also shows the lowest all-sky 24 h DARE obs values are on 08/13/2017 (in blue), confirmed by a mean all-sky 24 h DARE obs value of \sim 4 \pm 0.1 W.m⁻² on 08/13/2017 in Table 5 (compared to \sim 8 \pm 0.1 and \sim 14 \pm 0.1 W.m⁻² on the other days). This finding can be explained by 08/13/2017 also showing the highest number of non-cloudy sky (S4) cases in Fig. 3, the lowest mean CALIOP CF values in non-cloudy skies (indicating minimal cloud contamination of the S4 cases) and the highest mean AOD value in non-cloudy sky (i.e., 0.3 compared to 0.1-0.2 on the other days) in Table 5. The AOD above clouds on all 3 days (i.e., a mean AOD value from 0.2 to 0.6 in Table 5) agree with monthly averages of 0.2-0.6 in Sept 2016 and Aug 2017 in Chang et al., (2023) (see their Fig. 1). Also, Doherty et al., (2022) (see their Table 3) show a monthly average of integrated vertical profiles of scattering and absorption coefficients above clouds from in-situ instruments of 0.4 in 2016 and 0.3-0.6 in 2017. Mean 24 h cloudy (S1-S3) DARE obs are \sim 9 ± 0.1, 15 ± 0.1 and 8 ± 0.2 W·m⁻² on, respectively, 09/18/2016, 09/20/2016 and 08/13/2017, as shown in Table 5. These values are higher than in Kacenelenbogen et al., (2019), where we found mean 24 h cloudy DARE obs values of 2.49 ± 2.54 and 2.87 ± 2.33 W·m⁻² respectively in JJA and SON over a region between 19° and 2°N and 10°W and 8°E, using satellite data from 2008 to 2012. We attribute this difference in cloudy DARE obs to a difference in the period, the spatial domain, and the way DARE obs is computed. Here, the highest mean 24 h cloudy (S1-S3) DARE obs value of ~15 W·m⁻² is explained by the highest mean AOD above clouds of 0.6. Table 1 in Kacenelenbogen et al. (2019) lists other peer-reviewed calculations of cloudy DARE obs to which our results can be compared (e.g., Chand et al., 2009, Wilcox 2012, De Graaf et al., 2012, 2014, Meyer et al., 2013, 2015, Peers et al., 2015, and Feng and Christopher 2015)).

639

640

641 642

643

644

645

646

647

648

649

650 651

652

653

654

655656

657

658 659

660

661662

663

664

665 666

667 668 Figure 5 illustrates the spatial evolution of key input parameters to our (instant and 24 h mean) DARE_obs calculations, together with the DARE_obs values themselves along the CALIOP track on 08/13/2017. Figure A6 and A7 in the appendix show similar plots for the two other days. From the top to the bottom panels, it shows the location of S1, S2, S3 and S4 cases, the AOD (above cloud and in non-cloudy skies) \pm Δ AOD, COT, CER and CWP \pm Δ CWP values along the CALIOP track and DARE_obs \pm Δ DARE_obs (24 h and instant). The low 24 h DARE_obs value of $\sim 4\text{W}\cdot\text{m}^{-2}$ on 08/13/2017 (see Table 5) is in fact accompanied by strong DARE_obs variability along the track as illustrated on Fig. 5. For example, a thick cloud is detected at $\sim 10^{\circ}\text{S}$ latitude (see also Fig. 2), which corresponds to a peak in COT and CWP (but not CER) values. Over this region, our algorithm detects many S1 cases (in red) for which the AOD and SSA both remain relatively constant (i.e., a light absorbing aerosol plume with a strong loading) and the COT values increase. This leads to a sharp increase in the DARE obs values (i.e., more warming of the atmosphere).

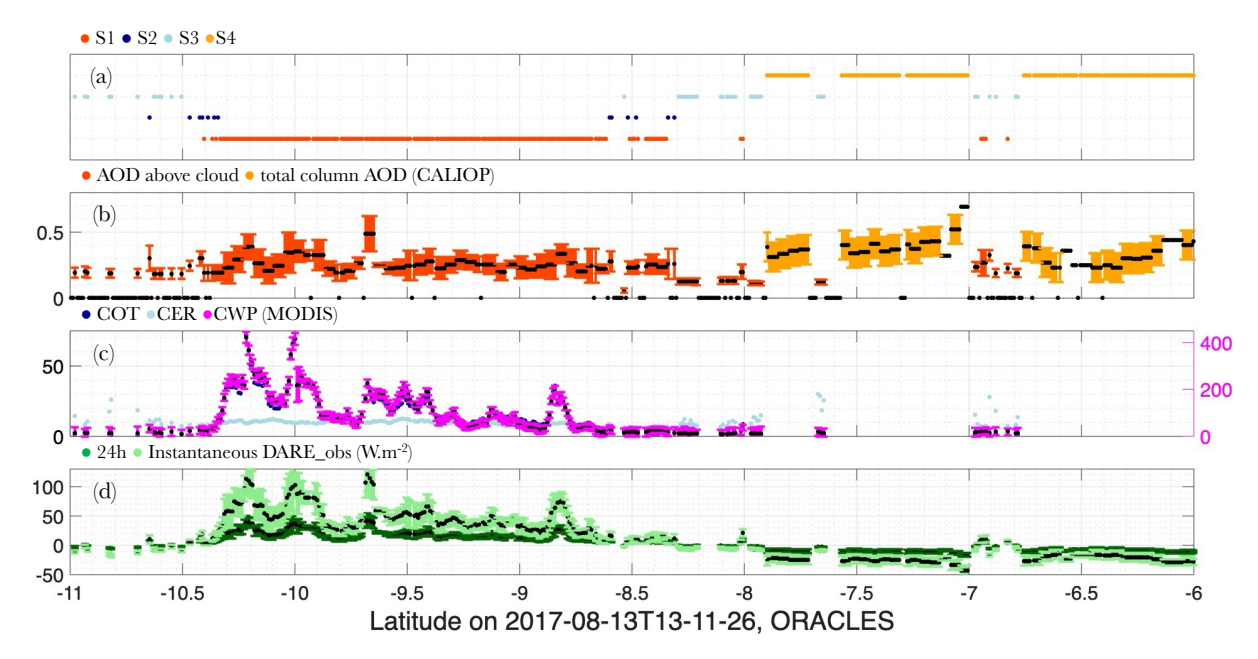


Figure 5: Spatial evolution of key input parameters to our DARE_obs calculations, together with the DARE_obs values (24 h and instant) along the CALIOP track on 08/13/2017. From the top to bottom panel: (a) S1, S2, S3 and S4 cases (red, dark blue, light blue, and orange respectively), (b) Version 2 AOD \pm Δ AOD at 532 nm (red above cloud and orange in non-cloudy sky), (c) COT (dark blue), CER (light blue), CWP \pm Δ CWP (magenta), (d) 24 h (dark green) and instant (light green) DARE_obs \pm Δ DARE_obs (W m⁻²) in the 442-625 nm RRTMG channel. Cloud retrieved optical properties are not corrected for aerosols above them. Instead of showing latitudes between 60°S and 20°S, we reduce the latitude range from 6°S to 11°S for visibility. See Fig. A6 and A7 for the two other days.

Figure A8 in the appendix illustrates 24 h DARE_obs values as a function of AOD and SSA in non-cloudy sky conditions (i.e., S4) on the right and as a function of AOD and COT in cloudy conditions (i.e., S1-S3) on the left on 09/18/2016, 09/20/2016 and 08/13/2017. First, as expected, DARE_obs values are more and more negative when paired with increasing AOD values in non-cloudy skies and any SSA values. Second, also as expected, we observe a clear increase in positive DARE_obs values when paired with an increase of AOD values above clouds. In cloudy conditions and when the AOD above clouds remains similar, DARE_obs records consistently higher values (more warming) when paired with a larger COT value. Note that we were able to reproduce this relationship in our theoretical calculations (see Fig. A2).

3.3 Assessment of DARE obs

3.3.1. Using DARE param

We first assess DARE_obs using the DARE_param calculations described in section 2.2 and Table 2. The DARE_param parametrization was developed during ORACLES, an airborne field campaign specifically designed to investigate aerosols above clouds. Because the DARE_param parameterization applies only to the subset of cloudy scenarios (i.e., S1-S3) measured during ORACLES, we do not include DARE_obs vs. DARE_param comparisons in

non-cloudy sky conditions (i.e., S4) in this paper. Figure 6 shows instant DARE_param on the x-axis and instant DARE_obs on the y-axis, colored by the AOD values above clouds on 09/18/2016 (left), 09/20/2016 (middle) and 08/13/2017 (right). The black crosses denote CALIOP cloud fractions that are below 1 (i.e., more broken clouds). The first section of Table 6 summarizes the statistics.

703

704

705

706

707

708

709

710

711

712

713

714

715

716

717

718

719

720

721

722

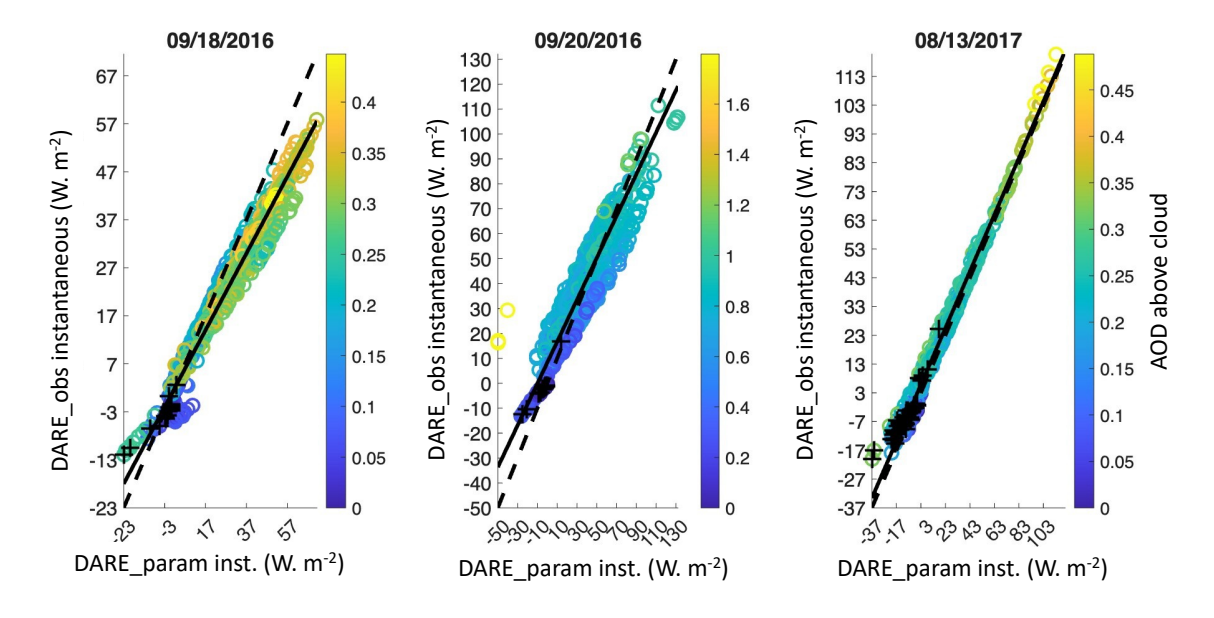


Figure 6: Semi-observational instant DARE_obs (y-axis) compared to DARE_param (x-axis) (W m⁻²) (see section 2.2 and Table 2) for cloudy cases (i.e., S1, S2 and S3 in Table 3) at 532 nm (i.e., in the 442-625 nm channel). Cloud retrieved optical properties are not corrected for aerosols above them. Latitudes are selected between 6°S and 20°S. Black crosses show points with CALIOP cloud fraction below 1 (i.e., more broken cloud). See Table 6 for statistics.

When evaluating our semi-observational DARE obs with coincident parametrized DARE param over all types of clouds (i.e., S1, S2 and S3 in Table 3) and for our three case studies, we find a generally satisfying agreement (R^2 =0.87 to 0.99, slope=0.80 to 0.99, offset =0.37 to 8.30, N=619 to 1067 in (1) Table 6). We posit that the slight differences between DARE obs and DARE param (see, for example, the mean cloudy DARE param and DARE obs values in panel (1) of Table 6) pertain to how they are computed. On the one hand, we assume MERRA-2's vertical distribution of SSA for the DARE obs calculations, even though the SSA magnitude lies outside the observed SSA variability during ORACLES (i.e., as seen in Fig. 4b in Cochrane et al. (2021), the peak of the *in-situ* SSA values measured at 532 nm is between 0.85 and 0.86). By invoking this assumption, we can either overestimate DARE obs if the MERRA-2 SSA value is too low or underestimate DARE obs if the MERRA-2 SSA value is too high. For example, when computing DARE theo (see Fig. A2), we record lower DARE theo values (by ~10 W m⁻²) when adding more scattering aerosols (i.e., "continental") to already absorbing aerosols (i.e., "urban") over a thick cloud (COT=10). A second example is seen on 09/20/2016, where the two data points showing high AOD values above clouds (in yellow) and causing an offset in the DARE param vs. DARE obs regression line (~8 in Table 6) are likely due to an underestimation of MERRA-2 SSA, which in turn causes an overestimation of DARE obs compared to DARE param. On the other hand, while DARE param is computed using the same AOD and cloud microphysical properties as DARE obs, the DARE param framework was developed specifically for aerosols above homogeneous cloud conditions (i.e., S1) and thus might not apply as well to broken and/ or thin clouds (i.e., S2 and S3). The various

amounts of S1, S2 and S3 cases during our three case studies (illustrated in Fig. 3) likely influence the DARE_param accuracy. We also note a distinctive feature in Fig. 6 on 09/18/2016 away from the 1:1 line for low AOD and CALIOP cloud fractions below 1 (black crosses). This feature is very likely due to cloud inhomogeneities paired with low AOD values.

| (1) Cloudy (S1-S3) DARE_param vs. | Dates | | | | | |
|---|---------------------|------------|---------|------------|-----------|--|
| DARE_obs at 532nm | 09/18/2016 | 09/20/2016 | | 08/13/2017 | | |
| Number | 1067 | 840 | | 619 | | |
| RMSE | 6.9 (31%) | 10.3 (28%) | 3.6 (19 | | %) | |
| \mathbb{R}^2 | 0.97 | 0.87 | | 0.99 | | |
| Slope | 0.8 | 0.8 | | 1.0 | | |
| Offset | 0.4 | 8.3 | | 2.9 | | |
| Mean cloudy DARE_param (W m ⁻²) | 27.7 | 34.1 | | 16.6 | | |
| Mean cloudy DARE_obs (W m-2) | 22.5 | 36.9 19.2 | | 19.2 | | |
| (2) All-sky (S1-S4) SSFR vs. | SW RRTMG Bands (nm) | | | | | |
| DARE_obs-related fluxes on 08/13/2017 | 778-1242 | 625-778 | 442 | -625 | 345-442 | |
| Number | | 5] | | | | |
| RMSE | 17.4 (17%) | 6.9 (9%) | 11.7 (| 9%) | 8.2 (16%) | |
| \mathbb{R}^2 | 0.95 | 0.95 | 0.95 | | 0.94 | |
| Slope | 1.1 | 0.9 | 0.8 | | 0.8 | |
| Offset | 7.0 | 5.8 | 14.9 | | 13.9 | |
| Mean all-sky SSFR-measured fluxes (W m ⁻²) | 89.7 | 78.7 | 128.5 | | 43.3 | |
| Mean all-sky DARE_obs-related fluxes (W m ⁻²) | 104.9 | 77.0 | 124.4 | | 50.8 | |

Table 6: Number, Root Mean Square error (RMSE), correlation coefficient, R², and linear regression parameters between (1) cloudy (S1-S3) DARE_param vs. DARE_obs at 532nm (i.e., in the 442-625nm channel) for our three case studies and (2) all-sky (S1-S4) SSFR-measured and DARE_obs-related fluxes in four SW RRTMG broadband channels; % in parathesis is based on the mean cloudy DARE_obs in panel (1) and the mean DARE_obs-related fluxes in panel (2). Latitudes are between 6°S and 20°S.

3.3.2. Using Airborne SSFR Upward Spectral Irradiance Measurements

740 After the statistical assessment of DARE obs using DARE param in section 3.3.1, we now assess DARE obs using 741 the spatially and temporally co-located SSFR measurements on our third case study of 08/13/2017 (see Fig. 2). 742 Although the collocation only provides limited samples for validation, the directly measured irradiance (which can be 743 used to indicate radiative effects) from SSFR can provide further insights in our DARE obs results. 744 We consider only those locations and times when (i) the aircraft flies above the CALIOP-inferred aerosol top height, 745 (ii) the aircraft measurements are within (≤) 0.7 km, (iii) the aircraft measurements are within ± 30 min of the CALIOP observations (i.e., between 13:00 and 14:00 UTC as the overpass occurs at ~13:30 UTC over the region) and 746 747 (iv) the aircraft is leveled (i.e., the aircraft pitch and role are both within ± 5 degrees). After applying those filters, we 748 find N=51 valid (>0) paired CALIOP-SSFR flux results corresponding to aircraft altitudes between 3.57 and 6.46 km 749 above CALIOP aerosol top heights between 3.05 and 3.14 km, distances between CALIOP and the nearest SSFR 750 measurements from 0.44 to 0.70 km, times of SSFR measurements between 13:14 and 13:55 UTC, joint latitudes 751 between 7.86°S and 9.56°S (see Fig. 2 for context) and aircraft pitch and role between -1.5 and 3.5°. We use SSFR 752 "20170813_calibspecs_20171106p_1324_20170814s_150C_attcorr_ratio.nc" files called and

753754755

756

757758

759

760761

762

763

764

765766

767

768

769770

771

772773

774

"20170813 librad info.nc".

As a reminder, DARE obs is the subtraction of the upward spectral broadband irradiances (or fluxes received by a surface per unit area), $F_{b\lambda}^{\uparrow}_{no \text{ aerosol}} - F_{b\lambda}^{\uparrow}_{aerosol}$ in 13 RRTMG broadband channels (from 200 nm to 3,846 nm with spectral bands ranging from 56 to 769 nm in W·m⁻²). The airborne SSFR instrument mounted to the bottom of the aircraft measured the upward flux, F_{λ}^{\uparrow} , in narrow spectral bands (from 350 nm to 2,200 nm with a spectral resolution of 6 nm to 12 nm in W·m⁻²·nm⁻¹). We spectrally integrate SSFR F_{λ}^{\uparrow} within each SW RRTMG broadband channel using a trapezoidal numerical integration. For example, the first RRTMG channel that contains SSFR measurements is between 345 nm and 442 nm. SSFR's shortest channel is at 350nm and measures 15 increments of 6nm-spaced F_{λ}^{\uparrow} up to 442nm i.e., within the first RRTMG channel. Therefore, we sum all 15 increments of F_{λ}^{\uparrow} from SSFR (i.e., from 350 nm to 442 nm) and compare this value to F_{bλ}↑ in the first RRTMG channel (i.e., from 345 to 442 nm). The second part of Table 6 shows a satisfying agreement between SSFR F_{λ}^{\uparrow} and F_{λ}^{\uparrow} at the source of our semi-observational DARE obs in four relevant RRTMG broad band channels (i.e., 345-442, 442-625, 625-778 and 778-1242 nm). This is illustrated by a high correlation coefficient (0.94-0.95) and an RMSE value between 9 and 17 % in Table 6. Fig. A9 in the appendix shows the comparison between SSFR-measured and DARE obs-related fluxes as a function of distance between the aircraft and the satellite track. Figure 7 is like Fig. 5 but focuses on the comparison between collocated airborne and satellite observations (i.e., from -9.6 to -7.9° Latitude). Panel (a) shows the N=51 collocated cases with valid satellite and airborne data (black crosses) and the different S1-S4 scenarios as a function of latitude. Among our N = 51 points, we find a majority of S1 cases, followed by S3 and S4 cases in this stretch. Panel (b) shows AOD ±ΔAOD above clouds and in non-cloudy skies. Panel (c) shows COT, CER and CWP ±ΔCWP. Panel (d) shows the satellite radiative fluxes, $F_{b\lambda}^{\uparrow}$, behind our DARE obs calculations in light green (W·m⁻²) and the distance between the aircraft and the CALIOP ground track in magenta from 0.45 to 0.70 km. Panel (e) shows the absolute difference

between SSFR and satellite $F_{b\lambda}^{\uparrow}$ as a percentage of the satellite radiative fluxes in all four broadband channels (778-775 1242 in solid grey, 625-778 in solid black, 442-625 in dotted black, 345-442 nm in dotted grey). 776 From ~9.2°S to 7.9°S in latitude in Fig. 7, distances between the aircraft and the CALIOP ground track are higher (> 777 778 600m in magenta in (d)), clouds are thinner (i.e., low COT values in dark blue in (c)) and/or more broken (i.e., more 779 S3 cases in (a)), and AOD above cloud is smaller (in red in (b)). These conditions all seem to lead to more unstable 780 and generally higher satellite-SSFR flux differences (e). This is confirmed by Fig. A9 where we observe more scatter between SSFR F_{λ}^{\uparrow} and F_{λ}^{\uparrow} at the source of our semi-observational DARE_obs when the distance between satellite 781 and aircraft increases (see yellow markers) in all four channels. For increased visibility and because the spatial 782 satellite-aircraft colocation is deteriorated from ~9.2°S to 7.9°S in latitude (and hence the data is of lesser significance 783 784 to the overall analysis), we allow a few data points in panel (e) to extend beyond the figure's axes. If we focus on points of close satellite-aircraft collocation (i.e., from ~9.6°S to 9.2°S, < 600 m in magenta in (d)), 785 satellite $F_{b\lambda}$ (in light green in (d)) shows high values (>100 W m⁻²) due to the presence of S1 cases (red dots in (a)), 786 high AOD in (b) and high COT values in (c). For these points, we find an absolute difference in all four broadband 787 channels below ~20% and an absolute difference below 15% between 778 and 442 nm (solid black and dotted black 788 789 in (e)).

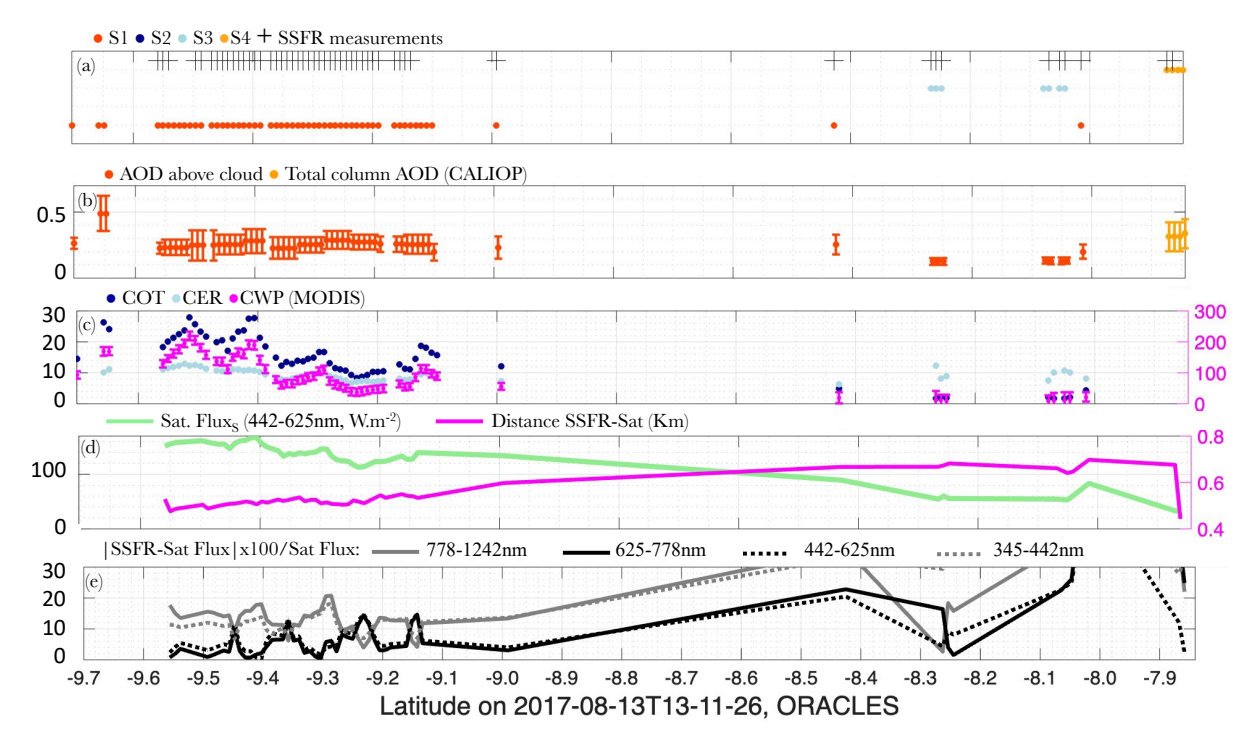


Figure 7. Spatial evolution of key input parameters along the CALIOP track, with a focus on when and where we have collocated airborne SFFR measurements for validation on 08/13/2017. From the top to bottom panel: (a) S1, S2, S3, S4 cases (red, dark blue, light blue, and orange respectively) and collocated SSFR measurements (black crosses), (b) Version 2 AOD $\pm\Delta$ AOD at 532 nm (red above cloud and orange in non-cloudy sky), (c) COT (dark blue), CER (light blue), CWP $\pm\Delta$ CWP (magenta), (d) collocated satellite broadband (spectrally integrated) upward irradiance (or flux) received by a surface per unit area in W·m⁻², F_{bλ} \uparrow , behind our DARE_obs calculations in the 442-625 nm RRTMG channel in light green (W·m⁻²) and distance between the aircraft and the CALIOP ground track (km) in magenta, (e) absolute difference between SSFR and satellite F_{bλ} \uparrow in all four broadband channels (solid grey for 778-1242, solid black for 625-778, dotted black for 442-625, and dotted grey for 345-442 nm) as a percentage of satellite F_{bλ} \uparrow . Cloud retrieved optical properties are not corrected for aerosols above them.

4 Discussions and Future Work

As described in Table 2, MERRA-2 is used in this paper to define the uppermost aerosol top height and lowermost aerosol base height below clouds, the vertical distribution of spectral aerosol extinction coefficient, ASY and SSA, and the atmospheric composition, weather and ocean surface winds. First, we currently use MERRA-2's vertical distribution of aerosols at face value with no consideration of a very likely bias in the modelled aerosol vertical profile (see section 2.1.2). An improvement worth exploring would be to select the MERRA-2 vertical location that corresponds to the strongest aerosol signal. Second, another improvement would be to infer aerosol vertical distribution and loading below clouds as a function of near-by satellite-observed non-cloudy sky aerosol cases. Third,

pairing ESA/JAXA EarthCARE (Wehr et al., 2023) launched in May 2024, NASA PACE (Werdell et al., 2019), SPEXone (Hasekamp et al., 2019), and HARP2 (Gao et al., 2023) launched in Feb 2024 might provide some insight on the observed vertical distribution of spectral aerosol extinction coefficient, ASY and SSA. The EarthCARE processing chain includes operational synergistic lidar, radar, and imager cloud fields, profiles of aerosols, atmospheric heating rates and top-of-atmosphere SW and longwave fluxes using 3D radiative transfer. These fluxes are automatically compared with EarthCARE broad-band radiometer measurements, allowing for a radiative closure assessment of the retrieved cloud and aerosol properties. However, the PACE and EarthCARE satellites are never perfectly co-located in both time and space. The Atmosphere Observing System mission (AOS), on the other hand, holds promising new science as it consists, at the time of writing, of a suite of lidar, radar, and radiometer satellites flying in formation to jointly observe aerosol, cloud, convection, and precipitation. We note that using EarthCARE's joint lidar and imager (possibly paired with PACE polarimeters) will likely reduce the number of unassigned scenarios in this paper as it will provide improved LWLC classification and optical properties, and possibly reduce the mismatch between cloudy and non-cloudy sky scenes.

826827828

829 830

831

832

833

834

835

836

837

838

839

840

841

842

843

844

845

846

847848

849

850

814

815

816

817

818

819

820

821

822

823

824

825

In this paper, to compute our 24 h DARE obs, we solely vary SZAs every hour during the day, which implicitly assumes constant aerosol and cloud vertical optical properties (see Table 2). On a global scale, most of the 24 h DARE variability is due to the varying solar zenith angles. Global 24 h mean DARE does not need many hourly measurements if the AOD is representative of the daily mean (e.g., at the Aqua and Terra overpass times). For example, Arola et al. (2013) found that the average impact of 2 AOD variability on 24 h mean DARE estimates is small when averaged over all global Aerosol Robotic Network (AERONET) sites (Holben et al., 1998). Regional DARE, unlike global DARE, can show considerable variability throughout the day due to varying aerosol and cloud fields. Xu et al. (2016), for example, show that the daily mean non-cloudy skies TOA DARE is overestimated by up to 3.9 W·m⁻² in the summertime in Beijing if they use a constant Aqua MODIS AOD value, compared to accounting for the observed hourly averaged daily variability. According to Min and Zhang (2014) (see their Table 2), assuming a constant CF derived from Aqua MODIS generally leads to an underestimation (less positive) by 16% in the all-skies DARE calculations. Chang et al. (2025) find that including observed cloud diurnal cycle from geostationary (GEO) satellites over the Southeast Atlantic results in nearly a twofold (about 1.4 W m⁻²) increase in the regional mean aerosol radiative warming, compared to assuming a constant early-afternoon cloud field throughout the entire day. We plan on adding diurnal aerosol and cloud information in future DARE obs calculations (instead of only varying SZA) using colocated GEO satellite observations. We note that aerosol and cloud retrievals from GEO satellites are in an earlier stage of development and less well-validated compared to their Low Earth Orbit (LEO) satellite counterparts. GEO aerosol and cloud retrievals are also currently often tied to specific GEO imagers and thus less global than their LEO counterparts. GEO AOD generally shows good agreement with ground-based AERONET AOD (e.g., low RMSE (0.12-0.17) in the case of the GEO Ocean Color Imager (GOCI) AOD over East Asia in Choi et al. (2019)) but have unique bias patterns related to the surface-reflectance assumptions in their retrieval algorithms (e.g., negative bias of 0.04 in GOCI AOD in Choi et al. (2019)). Recent improvements in algorithms consist in correcting surface reflectance, cloud masking and/ or fusing data from LEO and GEO imagers (e.g., Su et al. (2020), Zhang et al. (2020), Kim et al.

(2020), and Choi et al. (2019)). In some cases, GEO AOD, although often biased, was shown to reproduce the AERONET AOD diurnal cycle (e.g., over Asia, on a daily average, GOCI AOD shows a diurnal variation of +20% to -30% in inland sites according to Lennartson et al. (2018)).

853854855

856

857

858

859

860

861

862863

851852

Another extension to this work is to add an atmospheric scenario for which we observe one or more clouds overlying the LWLCs. With the addition of this multi-cloud atmospheric scenario, DARE_obs will be one step closer to a truly all-sky TOA SW DARE_obs. We envision this additional scenario to use (i) the CALIPSO-CloudSat-CERES-MODIS (CCCM or C3M) (Kato et al., 2010, 2011) derived cloud heights and cloud microphysical properties or equivalent EarthCARE-derived product (e.g., as in Table 1 of Mason et al., (2024)) and (ii) MERRA-2 simulated aerosol extensive and intensive properties. The new all-sky DARE_obs results can then be evaluated using collocated airborne field campaign observations such as from the HSRL-2 and the SFFR instruments during the Cloud, Aerosol and Monsoon Processes Philippines Experiment (CAMP²Ex) in 2019 over Southeast Asia. Note that adding atmospheric scenes showing multiple clouds on the vertical would increase the overall number of assigned atmospheric scenarios in our study.

864865866

867

868 869

870

871

872

873

874

875

876

877

878

879

880

881

882

883

884

885

At present, the order of importance of key aerosol, cloud and surface parameters in DARE calculations remains unclear. Thorsen et al., (2020) find that in non-cloudy skies, AOD, SSA and ASY is the order of importance of key aerosol parameters in DARE calculations. However, priorities can differ regionally according to airborne DARE sensitivity studies (e.g., Cochrane et al., 2019, 2021). According to Elsey et al., (2024), the AOD uncertainty is the main contributor to the overall uncertainty on DARE except over bright surfaces where SSA uncertainty contributes most. We plan to apply our DARE_obs calculations to multiple years of combined satellite and model data over different regions of the world. The most important factors influencing the transferability of our method to regions of the globe outside the Southeast Atlantic are (i) different Earth's surfaces (i.e., ocean vs. different land types) and (ii) different horizontal, vertical and temporal distributions of aerosol and cloud types and amounts. Our method requires aerosols in cloud-free skies, and above and below single thick, thin and/ or broken low warm liquid clouds. Kacenelenbogen et al. (2019) define six major global aerosol "hotspots" over single thick low warm liquid clouds (i.e., different aerosol regimes above the same type of clouds) in the northeast Pacific, southeast Pacific, tropical Atlantic, southeast Atlantic, Indian ocean, offshore from western Australia and northwest Pacific (see their Fig. 6; and Table 2 for a list of studies over these regions). According to Fig. 7d of Kacenelenbogen et al. (2019), the region of Southeast Atlantic (this paper) shows the highest mean annual percentage of high AOD values above clouds compared to the five other regions. Note that we also plan to apply our DARE obs calculations to regions that show different cloud regimes in addition to different aerosol regimes (e.g., the Southeast Atlantic, the tropical Atlantic, and a region encompassing the latter two representing the transition between these two regimes). We then plan to use this larger DARE obs dataset for different atmospheric scenarios, over specific regions of the world and linked to key cloud, aerosol and surface input parameters to assess the order of importance of these parameters in DARE obs calculations for specific aerosol and cloud regimes.

5 Conclusion

888

- 889 We compute TOA SW all-sky DARE obs combining CALIOP, MODIS and MERRA-2 along the CALIOP track. 890 These computations are made for four different atmospheric scenarios of aerosols above and below thick, thin and/or 891 broken clouds or aerosols in (mostly) non-cloudy skies. The clouds in our study must be single layer and low level 892 (<3km) liquid clouds. We focus our analysis on three days over the Southeast Atlantic for which we compare our 893 semi-observational DARE obs results to co-located suborbital aerosol and cloud observations during the ORACLES 894 field campaign. During these three days, satellite observations show a high number of cases with aerosols above and 895 below thick and homogeneous clouds (i.e., N=334-968 or 21-62% of our dataset), followed by cases that are not 896 assigned in our study (i.e., N=400-754 or 26-48% of our dataset). 897 The semi-observational 24 h average DARE obs values for our three days range from -25 (cooling) to 40 W·m⁻² 898 (warming). Highly positive DARE obs values are mostly due to aerosols with high AOD above clouds with high COT 899 values. Highly negative DARE obs values, on the other hand, are mostly due to aerosols with high AOD values in 900 non-cloudy sky cases. We use two ways of evaluating our semi-observational DARE obs: (1) a DARE param 901 parametrization, dependent on the AOD and cloud albedo, that was designed using SSFR measurements during the 902 ORACLES field campaign; and (2) an upward irradiance (or flux) directly measured by the airborne SSFR instrument. 903 First, we demonstrate agreement between our semi-observational satellite DARE obs and coincident parametrized 904 DARE param over the region (R²=0.97-0.99, RMSE=19-31%, N=619-1067). Second, we also demonstrate agreement 905 between our semi-observational satellite upward spectral irradiance with coincident measurements from the co-located
- 907 We emphasize that using the EarthCARE lidar and imager instruments instead of pairing A-Train's CALIOP and 908 MODIS, as well as adding cases with one or more clouds above our single water cloud, would bring our results closer 909 to truly all-sky DARE results (and drastically decrease the number of unassigned atmospheric scenarios in our study). 910 We also plan on adding aerosol and cloud diurnal cycle information from co-located geostationary satellites to improve 911 our diurnal mean all-sky semi-observational DARE obs results. Finally, in this paper, we have concentrated on three 912 case studies to examine our methodology in detail and evaluate the results against airborne SSFR measurements. This 913 is a necessary first step before applying our algorithm to multiple years of combined satellite and model data over 914 different regions of the world. Our goal is to ultimately assess the order of importance of atmospheric parameters in 915 the calculation of DARE obs for specific aerosol and cloud regimes. Expanding on the work done in this study will

inform future missions on where, when, and how accurately the retrievals should be performed to most effectively

SSFR instrument in four short-wave broadband channels during ORACLES (R²=0.94-0.95, RMSE=9-17%, N=51).

917918919

916

906

Code and data availability

reduce all-skies DARE uncertainties.

920 Lidar Level 2 1 km Cloud Layer, V4-51 publicly CALIPSO archived here: https://asdc.larc.nasa.gov/project/CALIPSO/CAL LID L2 01kmCLay-Standard-V4-51 V4-51. 921 The CALIPSO 922 5 is Lidar Level km Merged Layer, V4-51 publicly archived here: 923 https://asdc.larc.nasa.gov/project/CALIPSO/CAL LID L2 05kmMLay-Standard-V4-51 V4-51. The CALIPSO 2 Profile, 924 Lidar Level Aerosol V4-51 publicly archived here:

- 925 https://asdc.larc.nasa.gov/project/CALIPSO/CAL LID L2 05kmAPro-Standard-V4-51 V4-51. The MODIS
- 926 CLDPROP L2 MODIS Aqua MODIS/Aqua Cloud Properties L2 5-Min Swath 1000 m is publicly archived here:
- https://ladsweb.modaps.eosdis.nasa.gov/missions-and-measurements/products/CLDPROP_L2_MODIS_Aqua/.
- 928 MERRA-2 data are available at MDISC: https://disc.gsfc.nasa.gov/datasets?project=MERRA-2, managed by the
- 929 NASA Goddard Earth Sciences (GES) Data and Information Services Center (DISC).

Author contributions

- 932 MK designed and performed the scientific analysis and led the preparation of the manuscript with contributions from
- all authors. KM, EN, MV, HC, SS, RF, RL, HB, PZ, RH and WM provided extensive guidance and insight into the
- 934 scientific analysis. EN, KM, MV, and HC provided specific data and guidance on how to use the data from MERRA-
- 935 2, MODIS, CALIOP, and SSFR respectively. RK was instrumental in designing the atmospheric scenarios and
- 936 processed the matching of CALIOP, MODIS and MERRA-2 and other supporting analysis. NA was instrumental in
- processing all the RT-related calculations. MK analyzed all the output results.

938939

Competing interests

The contact author has declared that none of the authors has any competing interests

941942

Acknowledgements

- The authors are extremely grateful for guidance and technical support from the CALIOP, MODIS, MERRA-2 and
- 944 SSFR teams.

945

946 Financial support

- This research has been supported by the National Aeronautics and Space Administration Research Opportunities in
- 948 Space and Earth Science (ROSES) CloudSat and CALIPSO Science Team Recompete program (A.26),
- 949 NNH21ZDA001N-CCST.

950

951 References

- Arola, A., Eck, T. F., Huttunen, J., Lehtinen, K. E. J., Lindfors, A. V., Myhre, G., Smirnov, A., Tripathi, S. N., and
- Yu, H.: Influence of observed diurnal cycles of aerosol optical depth on aerosol direct radiative effect, Atmos. Chem.
- 954 Phys., 13, 7895–7901, https://doi.org/10.5194/acp-13-7895-2013, 2013.

955

- Avery, M. A., R. A. Ryan, B. J. Getzewich, M. A. Vaughan, D. M. Winker, Y. Hu, A. Garnier, J. Pelon, and C. A.
- 957 Verhappen: CALIOP V4 Cloud Thermodynamic Phase Assignment and the Impact of Near-Nadir Viewing Angles,
- 958 Atmos. Meas. Tech., **13**, 4539–4563, https://doi.org/10.5194/amt-13-4539-2020, 2020.

- 960 Bevington, P. R., and D. K. Robinson: <u>Data Reduction and Error Analysis for the Physical Sciences</u>, 2nd Ed., ISBN
- 961 978-0079112439, McGraw-Hill Inc., 328 pp, 1992.

- 963 Chand, D., Anderson, T. L., Wood, R., Charlson, R. J., Hu, Y., Liu, Z., and Vaughan, M.: Quantifying above-cloud
- aerosol using spaceborne lidar for improved understanding of cloudy-sky direct climate forcing, J. Geophys. Res.,
- 965 D13206, 113, https://doi.org/10.1029/2007JD009433, 2008.

966

- Chand, D., Wood, R., Anderson, T. L., Satheesh, S. K., and Charlson, R. J.: Satellite-derived direct radiative effect of
- 968 aerosols dependent on cloud cover, Nat. Geosci., 2, 181–184, https://doi.org/10.1038/ngeo437, 2009.

969

- 970 Chang, I., Gao, L., Flynn, C. J., Shinozuka, Y., Doherty, S. J., Diamond, M. S., Longo, K. M., Ferrada, G. A.,
- Carmichael, G. R., Castellanos, P., da Silva, A. M., Saide, P. E., Howes, C., Xue, Z., Mallet, M., Govindaraju, R.,
- Wang, Q., Cheng, Y., Feng, Y., Burton, S. P., Ferrare, R. A., LeBlanc, S. E., Kacenelenbogen, M. S., Pistone, K.,
- 973 Segal-Rozenhaimer, M., Meyer, K. G., Ryoo, J.-M., Pfister, L., Adebiyi, A. A., Wood, R., Zuidema, P., Christopher,
- 974 S. A., and Redemann, J.: On the differences in the vertical distribution of modeled aerosol optical depth over the
- 975 southeastern Atlantic, Atmos. Chem. Phys., 23, 4283–4309, https://doi.org/10.5194/acp-23-4283-2023, 2023.

976

- 977 Chang I., L. Gao, A. Adebiyi, S. Doherty, D. Painemal, W. L. Smith, E. Lenhardt, A. Fakoya, C. Flynn, J. Zheng, Z.
- 978 Yang, P. Castellanos, A. da Silva, Z. Zhang, R. Wood, P. Zuidema, S. Christopher, J. Redemann, 2025 (in press):
- Programmer Regional aerosol warming enhanced by the diurnal cycle in low cloud, *Nature Geosci*. (reference number: NGS-2024-
- 980 06-01329)

981

- Chin, M., Ginoux, P., Kinne, S., Holben, B. N., Duncan, B. N., Martin, R. V., Logan, J. A., Higurashi, A., and
- 983 Nakajima, T.: Tropospheric aerosol optical thickness from the GOCART model and comparisons with satellite and
- 984 sunphotometer measurements, J. Atmos. Sci., 59, 461–483, https://doi.org/10.1175/1520-
- 985 0469(2002)059<0461:TAOTFT>2.0.CO;2, 2002.
- 986 Choi, M., Lim, H., Kim, J., Lee, S., Eck, T. F., Holben, B. N., Garay, M. J., Hyer, E. J., Saide, P. E., and Liu, H.:
- 987 Validation, comparison, and integration of GOCI, AHI, MODIS, MISR, and VIIRS aerosol optical depth over East
- 988 Asia during the 2016 KORUS-AQ campaign, Atmos. Meas. Tech., 12, 4619–4641, https://doi.org/10.5194/amt-12-
- 989 4619-2019, 2019.
- 990 Clough, S. A., M. W. Shephard, E. J. Mlawer, J. S. Delamere, M. J. Iacono, K. Cady-Pereira, S. Boukabara, and P. D.
- 991 Brown, Atmospheric radiative transfer modeling: A summary of the AER codes, J. Quant. Spectrosc. Radiat. Transfer,
- 992 91, 233–244, 2005.

- Cochrane, S. P., Schmidt, K. S., Chen, H., Pilewskie, P., Kittelman, S., Redemann, J., LeBlanc, S., Pistone, K.,
- 995 Kacenelenbogen, M., Segal Rozenhaimer, M., Shinozuka, Y., Flynn, C., Platnick, S., Meyer, K., Ferrare, R., Burton,
- 996 S., Hostetler, C., Howell, S., Freitag, S., Dobracki, A., and Doherty, S.: Above-cloud aerosol radiative effects based

- 997 on ORACLES 2016 and ORACLES 2017 aircraft experiments, Atmos. Meas. Tech., 12, 6505-6528,
- 998 https://doi.org/10.5194/amt-12-6505-2019, 2019.

- 1000 Cochrane, S. P., Schmidt, K. S., Chen, H., Pilewskie, P., Kittelman, S., Redemann, J., LeBlanc, S., Pistone, K.,
- 1001 Kacenelenbogen, M., Segal Rozenhaimer, M., Shinozuka, Y., Flynn, C., Dobracki, A., Zuidema, P., Howell, S.,
- 1002 Freitag, S., and Doherty, S.: Empirically derived parameterizations of the direct aerosol radiative effect based on
- 1003 ORACLES aircraft observations, Atmos. Meas. Tech., 14, 567–593, https://doi.org/10.5194/amt-14-567-2021, 2021.

1004

- 1005 Colarco, P., da Silva, A., Chin, M. and Diehl, T.: Online simulations of global aerosol distributions in the NASA
- 1006 GEOS-4 model and comparisons to satellite and ground-based aerosol optical depth. Journal of Geophysical Research:
- 1007 Atmospheres, 115(D14), 2010.

1008

- 1009 Colarco, P. R., Kahn, R. A., Remer, L. A., and Levy, R. C.: Impact of satellite viewing-swath width on global and
- 1010 regional aerosol optical thickness statistics and trends, Atmos. Meas. Tech., 7, 2313-2335,
- 1011 https://doi.org/10.5194/amt-7-2313-2014, 2014.

1012

- 1013 Cox, C. and Munk, W.: Measurement of the roughness of the sea surface from photographs on the Sun's glitter, J.
- 1014 Opt. Soc. Am., 44, 838–850, doi:10.1364/JOSA.44.000838, 1954.

1015

- 1016 Das, Sampa, et al. "Improved simulations of biomass burning aerosol optical properties and lifetimes in the NASA
- 1017 GEOS Model during the ORACLES-I campaign." Atmospheric Chemistry and Physics 24.7: 4421-4449, 2024.

1018

- De Graaf, M., Tilstra, L. G., Wang, P., and Stammes, P.: Retrieval of the aerosol direct radiative effect over clouds
- 1020 from spaceborne spectrometry, J. Geophys. Res., 117, D07207, https://doi.org/10.1029/2011JD017160, 2012.

1021

- De Graaf, M., Bellouin, N., Tilstra, L. G., Haywood J., and Stammes, P.: Aerosol direct radiative effect of smoke over
- 1023 clouds over the southeast Atlantic Ocean from 2006 to 2009, Geophys. Res. Lett., 41, 7723-7730,
- 1024 https://doi.org/10.1002/2014GL061103, 2014.

1025

- Doherty, S. J., Saide, P. E., Zuidema, P., Shinozuka, Y., Ferrada, G. A., Gordon, H., Mallet, M., Meyer, K., Painemal,
- D., Howell, S. G., Freitag, S., Dobracki, A., Podolske, J. R., Burton, S. P., Ferrare, R. A., Howes, C., Nabat, P.,
- 1028 Carmichael, G. R., da Silva, A., Pistone, K., Chang, I., Gao, L., Wood, R., and Redemann, J.: Modeled and observed
- properties related to the direct aerosol radiative effect of biomass burning aerosol over the southeastern Atlantic,
- 1030 Atmos. Chem. Phys., 22, 1–46, https://doi.org/10.5194/acp-22-1-2022, 2022.

- 1032 Elsey, Jonathan, Nicolas Bellouin, and Claire Ryder. "Sensitivity of global direct aerosol shortwave radiative forcing
- to uncertainties in aerosol optical properties." Atmospheric Chemistry and Physics 24.7: 4065-4081, 2024.

- Feng, N. and Christopher, S. A.: Measurement-based estimates of direct radiative effects of absorbing aerosols above
- 1036 clouds, J. Geophys. Res.-Atmos., 120, 6908–6921, https://doi.org/10.1002/2015JD023252, 2015.

1037

- Ferrare, R., Burton, S., Cook, A., Harper, D., Hostetler, C., Hair, J., Fenn, M., Scarino, A. J., Müller, D., Chemyakin,
- 1039 E., Vaughan, M., Hu, Y., Meyer, K., Wind, G., Ridgway, B., Jethva, H., Torres, O., and Redemann, J.: Airborne High
- 1040 Spectral Resolution Lidar Measurements of Smoke Aerosol above Clouds during ORACLES, NASA Technical
- Report #20200009498, 3rd International A-Train Symposium, Pasadena, CA, 19-21 April 2017,
- 1042 https://ntrs.nasa.gov/citations/20200009498, 2017.

1043

- Forster, P., Storelvmo, T., Armour, K., Collins, W., Dufresne, J. L., Frame, D., Lunt, D. J., Mauritsen, T., Palmer, M.
- D., Watanabe, M., Wild, M., and Zhang, H.: The Earth's Energy Budget, Climate Feedbacks, and Climate Sensitivity.
- 1046 In Climate Change 2021: The Physical Science Basis. Contribution of Working Group I to the Sixth Assessment
- 1047 Report of the Intergovernmental Panel on Climate Change, Cambridge, UK, 923-1054,
- 1048 https://doi.org/10.1017/9781009157896.009, 2021.

1049

- Gao, M., Franz, B. A., Zhai, P.-W., Knobelspiesse, K., Sayer, A. M., Xu, X., Martins, J. V., Cairns, B., Castellanos,
- 1051 P., Fu, G., Hannadige, N., Hasekamp, O., Hu, Y., Ibrahim, A., Patt, F., Puthukkudy, A., and Werdell, P. J.:
- Simultaneous retrieval of aerosol and ocean properties from PACE HARP2 with uncertainty assessment using
- cascading neural network radiative transfer models, Atmos. Meas. Tech., 16, 5863–5881, https://doi.org/10.5194/amt-
- 1054 16-5863-2023, 2023.

1055

- 1056 Gelaro, R., M. G. Bosilovich, R. Todling, A. Molod, L. Takacs, M. Suarez, C. Randles, A. Darmenov, K. Wargan, R.
- Reichle, et al.: The Modern-Era Retrospective Analysis for Research and Applications, Version 2 (MERRA-2). J.
- 1058 Clim., 30, 5419-5454, doi:10.1175/JCLI-D-16-0758.1, 2017.

1059

- Grosvenor D. P., O. Sourdeval, P. Zuidema, A. Ackerman, M. D.Alexandrov, R. Bennartz, R. Boers, B. Cairns, C.
- 1061 Chiu, M. Christensen, H. Deneke, M. Diamond, G. Feingold, A. Fridlind, A. Hünerbei, C. Knist, P. Kollias, A.
- 1062 Marshak, D. McCoy, D. Merk, D. Painemal, J. Rausch, D. Rosenfeld, H. Russchenberg, P. Seifert, K. Sinclair, P. Stier,
- 1063 B. van Diedenhoven, M. Wendisch, F. Werner, R. Wood, Z. Zhang, and J. Quaas, 2018: Remote sensing of droplet
- number concentration in warm clouds: A review of the current state of knowledge and perspectives. Rev. in Geophys.,
- 1065 56, p. 409-453, doi:10.1029/2017RG000593

1066

- Gupta, S., McFarquhar, G. M., O'Brien, J. R., Poellot, M. R., Delene, D. J., Chang, I., et al.: In situ and satellite-based
- 1068 estimates of cloud properties and aerosol-cloud interactions over the southeast Atlantic Ocean. Atmospheric
- 1069 Chemistry and Physics, 22(19), 12923–12943. https://doi.org/10.5194/acp-22-12923-2022, 2022.

- 1071 Global Modeling and Assimilation Office (GMAO), inst3 3d asm Cp: MERRA-2 3D IAU State, Meteorology
- 1072 Instantaneous 3-hourly (p-coord, 0.625x0.5L42), version 5.12.4, Greenbelt, MD, USA: Goddard Space Flight Center
- Distributed Active Archive Center (GSFC DAAC), Accessed 03/06/2025 at doi: 10.5067/VJAFPLI1CSIV, 2015.

- 1075 Hasekamp, O. P. et al. Aerosol measurements by SPEXone on the NASA PACE mission: expected retrieval
- capabilities. J. Quant. Spectrosc. Radiat. Transf. 227, 170–184, 2019.

1077

- 1078 Hess, Michael, Peter Koepke, and Ingrid Schult. "Optical properties of aerosols and clouds: The software package
- 1079 OPAC." Bulletin of the American meteorological society 79.5: 831-844, 1998.

1080

- Holben, B. N., Eck, T. F., Slutsker, I., Tanre, D., Buis, J. P., Setzer, A., Vermote, E., Reagan, J. A., Kaufman, Y.,
- 1082 Nakajima, T., Lavenu, F., Jankowiak, I., and Smirnov, A.: AERONET A federated instrument network and data
- archive for aerosol characterization, Rem. Sens. Environ., 66, 1–16, 1998.

1084

- 1085 Holz, R. E., et al. "Global Moderate Resolution Imaging Spectroradiometer (MODIS) cloud detection and height
- evaluation using CALIOP." Journal of Geophysical Research: Atmospheres 113.D8, 2008.

1087

- Hu, Y., Vaughan, M., Winker, D., Liu, Z., Noel, V., Bissonnette, L., Roy, G., McGill, M., and Trepte, C.: A simple
- multiple scattering-depolarization relation of water clouds and its potential applications, Proceedings of 23nd
- 1090 International Laser Radar Conference, Nara, Japan, 24–28 July 2006, 19–22, 2006.

1091

- Hu, Y., Vaughan, M., Liu, Z., Powell, K., and Rodier, S.: Retrieving Optical Depths and Lidar Ratios for Transparent
- Layers Above Opaque Water Clouds From CALIPSO Lidar Measurements, IEEE Geosci. Remote, 4, 523–526, 2007

1094

- Hunt, W. H., Winker, D. M., Vaughan, M. A., Powell, K. A., Lucker, P. L., and Weimer, C.: CALIPSO lidar description
- and performance assessment, J. Atmos. Ocean. Tech., 26, 1214–1228, https://doi.org/10.1175/2009JTECHA1223.1,
- 1097 2009.

1098

- 1099 IPCC. Climate Change 2021: The Physical Science Basis (eds Masson-Delmotte, V. et al.) (Cambridge Univ. Press,
- 1100 2021).

1101

- 1102 Iacono, M. J., J. S. Delamere, E. J. Mlawer, M. W. Shephard, S. A. Clough, and W. D. Collins (2008), Radiative
- forcing by long-lived greenhouse gases: Calculations with the AER radiative transfer models, J. Geophys. Res., 113,
- 1104 D13103, doi:10.1029/2008JD009944.

- Jethva, H. T., Torres, O., Ferrare, R. A., Burton, S. P., Cook, A. L., Harper, D. B., Hostetler, C. A., Redemann, J.,
- 1107 Kayetha, V., LeBlanc, S., Pistone, K., Mitchell, L., and Flynn, C. J.: Retrieving UV-Vis spectral single-scattering

- albedo of absorbing aerosols above clouds from synergy of ORACLES airborne and A-train sensors, Atmos. Meas.
- Tech., 17, 2335–2366, https://doi.org/10.5194/amt-17-2335-2024, 2024.

- 1111 Jin Zhonghai, Yanli Qiao, Yingjian Wang, Yonghua Fang, and Weining Yi, "A new parameterization of spectral and
- broadband ocean surface albedo," Opt. Express 19, 26429-26443, 2011.

1113

- Joseph, J. H., W. J. Wiscombe, and J. A. Weinman, The delta-Eddington approximation for radiative flux transfer, J.
- 1115 Atmos. Sci., 33, 2452–2459, 1976.

1116

- Jouan, C., Myhre, G. Satellite-based analysis of top of atmosphere shortwave radiative forcing trend induced by
- biomass burning aerosols over South-Eastern Atlantic. npj Clim Atmos Sci 7, 129, https://doi.org/10.1038/s41612-
- 1119 <u>024-00631-3</u>, 2024.

1120

- Kacenelenbogen, M., Vaughan, M. A., Redemann, J., Hoff, R. M., Rogers, R. R., Ferrare, R. A., Russell, P. B.,
- Hostetler, C. A., Hair, J. W., and Holben, B. N.: An accuracy assessment of the CALIOP/CALIPSO version 2/version
- 3 daytime aerosol extinction product based on a detailed multi-sensor, multi-platform case study, Atmos. Chem. Phys.,
- 1124 11, 3981–4000, https://doi.org/10.5194/acp-11-3981-2011, 2011.

1125

- Kacenelenbogen, M., Redemann, J., Vaughan, M. A., Omar, A. H., Russell, P. B., Burton, S., Rogers, R. R., Ferrare,
- 1127 R. A., and Hostetler, C. A.: An evaluation of CALIOP/CALIPSO's aerosol-above-cloud detection and retrieval
- 1128 capability over North America, J. Geophys. Res.-Atmos., 119, 230-244, https://doi.org/10.1002/2013JD020178,
- 1129 2014.

1130

- Kacenelenbogen M. et al. "Estimations of global shortwave direct aerosol radiative effects above opaque water clouds
- using a combination of A-Train satellite sensors." Atmospheric Chemistry and Physics 19.7: 4933-4962, 2019.

1133

- 1134 Kacenelenbogen M. et al. "Identifying chemical aerosol signatures using optical suborbital observations: how much
- can optical properties tell us about aerosol composition?" Atmospheric Chemistry and Physics 22.6: 3713-3742, 2022

1136

- Kar, J., Lee, K.-P., Vaughan, M. A., Tackett, J. L., Trepte, C. R., Winker, D. M., Lucker, P. L., and Getzewich, B. J.:
- 1138 CALIPSO Level 3 Stratospheric Aerosol Product: Version 1.00 Algorithm Description and Initial Assessment, Atmos.
- 1139 Meas. Tech., **12**, 6173–6191, https://doi.org/10.5194/amt-12-6173-2019, 2019.

1140

- Kassianov, E.; Flynn, C.; Redemann, J.; Schmid, B.; Russell, P.B.; Sinyuk, A. Initial Assessment of the Spectrometer
- for Sky-Scanning, Sun-Tracking Atmospheric Research (4STAR)-Based Aerosol Retrieval: Sensitivity Study.
- 1143 *Atmosphere*, 3, 495-521. https://doi.org/10.3390/atmos3040495, 2012.

- Kato, S., S. Sun-Mack, W. F. Miller, F. G. Rose, Y. Chen, P. Minnis, and B. A. Wielicki: Relationships among
- cloud occurrence frequency, overlap, and effective thickness derived from CALIPSO and CloudSat merged cloud
- 1147 vertical profiles, J. Geophys. Res., 115, D00H28, doi:10.1029/2009JD012277, 2010

- Kato, S., et al.: Improvements of top-of-atmosphere and surface irradiance computations with CALIPSO, CloudSat,
- and MODIS derived cloud and aerosol properties, J. Geophys. Res., 116, D19209, doi:10.1029/2011JD16050, 2011.

1151

- Kim, M.-H., Omar, A. H., Tackett, J. L., Vaughan, M. A., Winker, D. M., Trepte, C. R., Hu, Y., Liu, Z., Poole, L. R.,
- Pitts, M. C., Kar, J., and Magill, B. E.: The CALIPSO Version 4 Automated Aerosol Classification and Lidar Ratio
- Selection Algorithm, Atmos. Meas. Tech., **11**, 6107-6135, https://doi.org/10.5194/amt-11-6107-2018, 2018.
- 1155 Kim, Jhoon, et al. "New era of air quality monitoring from space: Geostationary Environment Monitoring
- 1156 Spectrometer (GEMS)." Bulletin of the American Meteorological Society 101.1: E1-E22, 2020.
- King, N. J., Bower, K. N., Crosier, J., & Crawford, I.: Evaluating MODIS cloud retrievals with in situ observations
- from VOCALS-REx. Atmospheric Chemistry and Physics, 13(1), 191–209. https://doi.org/10.5194/acp-13-191-
- 1159 2013, 2013.

1160

- Kloss, Corinna, et al. "Stratospheric aerosol layer perturbation caused by the 2019 Raikoke and Ulawun eruptions and
- their radiative forcing." Atmospheric Chemistry and Physics 21.1: 535-560, 2021.

1163

- Korras-Carraca, M., V. Pappas, N. Hatzianastassiou, I. Vardavas, and C. Matsoukas: Global vertically resolved aerosol
- direct radiation effect from three years of CALIOP data using the FORTH radiation transfer model. Atmos. Res., 224,
- 1166 138–156, https://doi.org/10.1016/j.atmosres.2019.03.024, 2019.

1167

- 1168 Lacagnina, C., O. P. Hasekamp, and O. Torres: Direct radiative effect of aerosols based on PARASOL and OMI
- satellite observations. J. Geophys. Res. Atmos., 122, 2366–2388, https://doi.org/10.1002/2016JD025706, 2017.

1170

- 1171 Lee, Jaehwa, et al. "Retrieval of aerosol optical depth under thin cirrus from MODIS: Application to an ocean
- algorithm." Journal of Geophysical Research: Atmospheres 118.17: 10-111, 2013.

1173

- Lennartson, E. M., Wang, J., Gu, J., Castro Garcia, L., Ge, C., Gao, M., Choi, M., Saide, P. E., Carmichael, G. R.,
- Kim, J., and Janz, S. J.: Diurnal variation of aerosol optical depth and PM_{2.5} in South Korea: a synthesis from
- AERONET, satellite (GOCI), KORUS-AQ observation, and the WRF-Chem model, Atmos. Chem. Phys., 18, 15125–
- 1177 15144, https://doi.org/10.5194/acp-18-15125-2018, 2018.

- Li, J., Carlson, B.E., Yung, Y.L. et al. Scattering and absorbing aerosols in the climate system. Nat Rev Earth Environ
- 3, 363–379, https://doi.org/10.1038/s43017-022-00296-7, 2022.

- Liu, Z., Kuehn, R., Vaughan, M., Winker, D., Omar, A., Powell, K., Trepte, C., Hu, Y., and Hostetler, C.: The
- 1183 CALIPSO cloud and aerosol discrimination: Version 3, Algorithm and test results, 25th International Laser and
- radar conference, 2010.

1185

- Liu, Z., Winker, D., Omar, A., Vaughan, M., Kar, J., Trepte, C., Hu, Y., and Schuster, G.: Evaluation of CALIOP 532
- nm aerosol optical depth over opaque water clouds, Atmos. Chem. Phys., 15, 1265–1288, https://doi.org/10.5194/acp-
- 1188 15-1265-2015, 2015.

1189

- Liu, Z., Kar, J., Zeng, S., Tackett, J., Vaughan, M., Avery, M., Pelon, J., Getzewich, B., Lee, K.-P., Magill, B., Omar,
- 1191 A., Lucker, P., Trepte, C., and Winker, D.: Discriminating Between Clouds and Aerosols in the CALIOP Version 4.1
- Data Products, Atmos. Meas. Tech., 12, 703–734, https://doi.org/10.5194/amt-12-703-2019_2019.

1193

- Mason, S. L., Barker, H. W., Cole, J. N. S., Docter, N., Donovan, D. P., Hogan, R. J., Hünerbein, A., Kollias, P.,
- Puigdomènech Treserras, B., Qu, Z., Wandinger, U., and van Zadelhoff, G.-J.: An intercomparison of EarthCARE
- cloud, aerosol, and precipitation retrieval products, Atmos. Meas. Tech., 17, 875-898, https://doi.org/10.5194/amt-
- 1197 17-875-2024, 2024.

1198

- Matus, A. V., T. S. L'Ecuyer, J. E. Kay, C. Hannay, and J.-F. Lamarque: The role of clouds in modulating global
- aerosol direct radiative effects in spaceborne active observations and the Community Earth System Model. J. Climate,
- 28, 2986–3003, https://doi.org/10.1175/JCLI-D-14-00426.1, 2015

1202

- 1203 Matus, A. V., T. S. L'Ecuyer, and D. S. Henderson: New estimates of aerosol direct radiative effects and forcing from
- 1204 A-Train satellite observations. Geophys. Res. Lett., **46**, 8338–8346, https://doi.org/10.1029/2019GL083656, 2019.

1205

- Meador, W. E., and W. R. Weaver, Two-stream approximations to radiative transfer in planetary atmospheres: A
- unified description of existing methods and a new improvement, J. Atmos. Sci., 37, 630-643, 1980.

1208

- 1209 Meyer, K., Platnick, S., Oreopoulos, L., and Lee, D.: Estimating the direct radiative effect of absorbing aerosols
- 1210 overlying marine boundary layer clouds in the southeast Atlantic using MODIS and CALIOP, J. Geophys. Res.-
- 1211 Atmos., 118, 4801–4815, https://doi.org/10.1002/jgrd.50449, 2013.

1212

- 1213 Meyer, K., Platnick, S., and Zhang, Z.: Simultaneously inferring above-cloud absorbing aerosol optical thickness and
- underlying liquid phase cloud optical and microphysical properties using MODIS, J. Geophys. Res.-Atmos., 120,
- 1215 5524–5547, https://doi.org/10.1002/2015JD023128, 2015.

- 1217 Meyer, K., Platnick, S., Arnold, G. T., Amarasinghe, N., Miller, D., Small-Griswold, J., Witte, M., Cairns, B., Gupta,
- 1218 S., McFarquhar, G., and O'Brien, J.: Evaluating spectral cloud effective radius retrievals from the Enhanced MODIS
- 1219 Airborne Simulator (eMAS) during ORACLES, Atmos. Meas. Tech., 18, 981–1011, https://doi.org/10.5194/amt-18-
- 1220 981-2025, 2025.

- 1222 Min, Q., Joseph, E., Lin, Y., Min, L., Yin, B., Daum, P. H., et al.: Comparison of MODIS cloud microphysical
- properties with in-situ measurements over the Southeast Pacific. Atmospheric Chemistry and Physics, 12(23), 11261–
- 1224 11273. https://doi.org/10.5194/acp-12-11261-2012, 2012.

1225

- 1226 Min, Min, and Zhibo Zhang. "On the influence of cloud fraction diurnal cycle and sub-grid cloud optical thickness
- variability on all-skies direct aerosol radiative forcing." Journal of Quantitative Spectroscopy and Radiative Transfer
- 1228 142: 25-36, 2014.

1229

- Mlawer, E. J., Taubman, S. J., Brown, P. D., Iacono, M. J., and Clough, S. A.: Radiative transfer for inhomogeneous
- atmospheres: RRTM, a validated correlated-k model for the longwave, J. Geophys. Res., 102, 16663–16682, 1997.

1232

- 1233 Myhre, G., Samset, B., Schulz, M., Balkanski, Y., Bauer, S., Berntsen, T., et al.: Radiative forcing of the direct aerosol
- effect from AeroCom Phase II simulations. Atmospheric Chemistry and Physics, 13, 1853-1877. doi:10.5194/acp-13-
- 1235 1853-2013, 2013.

1236

- Nagle, Frederick W., and Robert E. Holz. "Computationally efficient methods of collocating satellite, aircraft, and
- 1238 ground observations." Journal of Atmospheric and Oceanic Technology 26.8: 1585-1595, 2009.

1239

- 1240 Nakajima, T. and King, M. D.: Determination of the optical thickness and effective particle radius of clouds from
- reflected solar radiation measurements. Part I: Theory, J. Atmos. Sci., 47, 1878–1893, 1990.

1242

- 1243 Nakajima, T., King, M. D., Spinhirne, J. D., & Radke, L. F.: Determination of the Optical Thickness and Effective
- 1244 Particle Radius of Clouds from Reflected Solar Radiation Measurements. Part II: Marine Stratocumulus Observations.
- 1245 Retrieved from https://journals.ametsoc.org/view/journals/atsc/48/5/1520-
- 1246 0469 1991 048 0728 dotota 2 0 co 2.xml, 1991.

1247

- 1248 Noble, S. R., & Hudson, J. G.: MODIS comparisons with northeastern Pacific in situ stratocumulus
- 1249 microphysics. Journal of Geophysical Research: Atmospheres, 120(16), 8332-
- 1250 8344. https://doi.org/10.1002/2014JD022785, 2015.

- Nowottnick, E.P., Colarco, P.R., Welton, E.J. and da SIIva, A.: Use of the CALIOP vertical feature mask for evaluating
- global aerosol models. Atmospheric Measurement Techniques, 8(9), pp.3647-3669, 2015.

1255 Oreopoulos, L., and H. W. Barker: Accounting for subgrid-scale cloud variability in a multi-layer 1-D solar radiative

transfer algorithm, Q. J. R. Meteorolog. Soc., 125, 301–330, 1999.

1257

- 1258 Oikawa, E., T. Nakajima, T. Inoue, and D. Winker: A study of the shortwave direct aerosol forcing using
- 1259 ESSP/CALIPSO observation and GCM simulation. J. Geophys. Res. Atmos., 118, 3687–3708,
- 1260 <u>https://doi.org/10.1002/jgrd.50227</u>, 2013.

1261

- 1262 Oikawa, E., T. Nakajima, and D. Winker: An evaluation of the shortwave direct aerosol radiative forcing using
- 1263 CALIOP and MODIS observations. J. Geophys. Res. Atmos., 123, 1211-1233,
- 1264 <u>https://doi.org/10.1002/2017JD027247</u>, 2018.

1265

- 1266 Peers, F., Waquet, F., Cornet, C., Dubuisson, P., Ducos, F., Goloub, P., Szczap, F., Tanré, D., and Thieuleux, F.:
- 1267 Absorption of aerosols above clouds from POLDER/PARASOL measurements and estimation of their direct radiative
- 1268 effect, Atmos. Chem. Phys., 15, 4179–4196, https://doi.org/10.5194/acp-15-4179-2015, 2015.

1269

- 1270 Painemal, D., & Zuidema, P.: Assessment of MODIS cloud effective radius and optical thickness retrievals over the
- 1271 Southeast Pacific with VOCALS-REx in situ measurements. Journal of Geophysical Research:
- 1272 Atmospheres, 116(D24). https://doi.org/10.1029/2011JD016155, 2011.

1273

- Peters, K., Quaas, J., and Bellouin, N.: Effects of absorbing aerosols in cloudy skies: a satellite study over the Atlantic
- 1275 Ocean, Atmos. Chem. Phys., 11, 1393–1404, https://doi.org/10.5194/acp-11-1393-2011, 2011.

1276

- 1277 Pilewskie, P., Pommier, J., Bergstrom, R., Gore, W., Howard, S., Rabbette, M., Schmid, B., Hobbs, P. V., and Tsay,
- 1278 S. C.:Solar spectral radiative forcing during the Southern African Regional Science Initiative, J. Geophys. Res., 108,
- 1279 8486, https://doi.org/10.1029/2002JD002411, 2003.

1280

- 1281 Pistone, K., J. Redemann, S. Doherty, P. Zuidema, S. Burton, B. Cairns, S. Cochrane, R. Ferrare, C. Flynn, S. Freitag,
- 1282 S. Howell, M. Kacenelenbogen, S. LeBlanc, X. Liu, S. Schmidt, A. Sedlacek, M. Segal-Rosenhaimer, Y. Shinozuka,
- 1283 S. Stamnes, B. v. Diedenhoven, G. V. Harten, and F. Xu, 2019: Intercomparison of biomass burning aerosol optical
- properties from in-situ and remote-sensing instruments in ORACLES-2016. Atmos. Chem. Phys., 19, p. 9181-9208,
- 1285 doi:acp-19-9181-2019, 2019.

1286

- 1287 Platnick, S., & Valero, F. P. J.: A Validation of a Satellite Cloud Retrieval during ASTEX. Journal of the Atmospheric
- 1288 Sciences, 52(16), 2985–3001. https://doi.org/10.1175/1520-0469(1995)052<2985:AVOASC>2.0.CO;2, 1995.

- 1290 Platnick, S., King, M. D., Ackerman, S. A., Menzel, W. P., Baum, B. A., Rieidi, J. C., and Frey, R. A.: The MODIS
- cloud products: Algorithms and examples from Terra, IEEE T. Geosci. Remote, 41, 459–473, 2003.

- 1293 Platnick, S.; Meyer, K.; Wind, G.; Holz, R.E.; Amarasinghe, N.; Hubanks, P.A.; Marchant, B.; Dutcher, S.; Veglio,
- 1294 P. The NASA MODIS-VIIRS Continuity Cloud Optical Properties Products. Remote Sens., 13, 2.
- 1295 https://doi.org/10.3390/rs13010002, 2021.

1296

- 1297 Rajapakshe, C., Z. Zhang, J. E. Yorks, H. Yu, Q. Tan, K. Meyer, S. Platnick, and D. M. Winker, Seasonally transported
- aerosol layers over southeast Atlantic are closer to underlying clouds than previously reported, Geophys. Res. Lett.,
- 1299 44, 5818–5825, doi:10.1002/2017GL073559, 2017.

1300

- Randles, C.A., Da Silva, A.M., Buchard, V., Colarco, P.R., Darmenov, A., Govindaraju, R., Smirnov, A., Holben, B.,
- 1302 Ferrare, R., Hair, J. and Shinozuka, Y.: The MERRA-2 aerosol reanalysis, 1980 onward. Part I: System description
- and data assimilation evaluation. Journal of climate, 30(17), pp.6823-6850, 2017.

1304

- 1305 Redemann, Jens, et al. "An overview of the ORACLES (ObseRvations of Aerosols above CLouds and their
- 1306 intEractionS) project: aerosol-cloud-radiation interactions in the Southeast Atlantic basin." Atmospheric Chemistry
- 1307 and Physics 21.3: 1507-1563, 2021.

1308

- Rogers, R. R., Vaughan, M. A., Hostetler, C. A., Burton, S. P., Ferrare, R. A., Young, S. A., Hair, J. W., Obland, M.
- D., Harper, D. B., Cook, A. L., and Winker, D. M.: Looking Through the Haze: Evaluating the CALIPSO Level 2
- Aerosol Optical Depth using Airborne High Spectral Resolution Lidar Data, Atmos. Meas. Tech., 7, 4317–4340,
- 1312 <u>https://doi.org/10.5194/amt-7-4317-2014</u>, 2014.

1313

13141315

- Russell, P. B., et al. "Comparison of aerosol single scattering albedos derived by diverse techniques in two North
- Atlantic experiments." Journal of the atmospheric sciences 59.3: 609-619, 2002.

1318

- Russell, Philip B., et al. "A multiparameter aerosol classification method and its application to retrievals from
- spaceborne polarimetry." Journal of Geophysical Research: Atmospheres 119.16: 9838-9863, 2014.

1321

- Ryan, R. A., Vaughan, M. A., Rodier, S. D., Tackett, J. L., Reagan, J. A., Ferrare, R. A., Hair, J. W., Smith, J. A.,
- and Getzewich, B. J.: Total column optical depths retrieved from CALIPSO lidar ocean surface backscatter, Atmos.
- 1324 Meas. Tech., 17, 6517–6545, https://doi.org/10.5194/amt-17-6517-2024, 2024.

- Ryoo J.-M., L. Pfister, R. Ueyama, P. Zuidema, R. Wood, I. Chang, J. Redemann: A meteorological overview of the
- ORACLES (ObseRvations of Aerosols above CLouds and their intEractionS) campaign over the southeast Atlantic
- during 2016-2018: Part 2 daily and synoptic characteristics. Atmos. Chem. Phys., 22, p. 14209-14241,
- 1329 doi:10.5194/acp-22-14209-2022, 2022.

- 1331 Schmidt, S. and Pilewskie, P.: Airborne measurements of spectral shortwave radiation in cloud and aerosol remote
- sensing and energy budget studies, in: Light Scattering Reviews, edited by: Kokhanovsky, A. A., Vol. 6, Light
- 1333 Scattering and Remote Sensing of Atmosphere and Surface, Berlin, Heidelberg, Springer Berlin Heidelberg, 239–
- 288, https://doi.org/10.1007/978-3-642-15531-4_6, 2012.

1335

- Stephens, G., Winker, D., Pelon, J., Trepte, C., Vane, D., Yuhas, C., L'Ecuyer, T., and Lebsock, M.: CloudSat and
- 1337 CALIPSO within the A-Train: Ten Years of Actively Observing the Earth System, B. Am. Meteorol. Soc., 99, 569–
- 1338 581, https://doi.org/10.1175/BAMS-D-16-0324.1, 2018.

1339

- Su, Wenying, et al. "Global all-sky shortwave direct radiative forcing of anthropogenic aerosols from combined
- satellite observations and GOCART simulations." Journal of Geophysical Research: Atmospheres 118.2: 655-669,
- 1342 2013.

1343

- 1344 Su, Tianning, et al. "Refining aerosol optical depth retrievals over land by constructing the relationship of spectral
- surface reflectances through deep learning: Application to Himawari-8." Remote Sensing of Environment 251: 112093,
- 1346 2020.

1347

- Tackett, J. L., Kar, J., Vaughan, M. A., Getzewich, B., Kim, M.-H., Vernier, J.-P., Omar, A. H., Magill, B., Pitts, M.
- 1349 C., and Winker, D.: The CALIPSO version 4.5 stratospheric aerosol subtyping algorithm, Atmos. Meas. Tech., 16,
- 1350 745–768, https://doi.org/10.5194/amt-16-745-2023, 2023.

1351

- 1352 Tatro, T. and P. Zuidema, 2025: More biomass burning aerosol is being advected westward over the southern tropical
- 1353 Atlantic since 2003. Science Tot. Env., 965, 178506, doi:10.1016/j.scitotenv.2025.178506

1354

- 1355 Thorsen, T. J., R. A. Ferrare, C. A. Hostetler, M. A. Vaughan, and Q. Fu: "The impact of lidar detection sensitivity
- on assessing aerosol direct radiative effects", Geophys. Res. Lett., 44, 9059-9067,
- 1357 https://doi.org/10.1002/2017GL074521, 2017.

1358

- Thorsen, Tyler J., et al. "Aerosol direct radiative effect sensitivity analysis." Journal of Climate 33.14: 6119-6139,
- 1360 2020.

- 1362 Thorsen, Tyler J., David M. Winker, and Richard A. Ferrare. "Uncertainty in observational estimates of the aerosol
- direct radiative effect and forcing." Journal of Climate 34.1: 195-214, 2021.

- Toth, T. D., Campbell, J. R., Reid, J. S., Tackett, J. L., Vaughan, M. A., Zhang, J., and Marquis, J. W.: Minimum
- 1366 Aerosol Layer Detection Sensitivities and their Subsequent Impacts on Aerosol Optical Thickness Retrievals in
- 1367 CALIPSO Level 2 Data Products, Atmos. Meas. Tech., 11, 499–514, https://doi.org/10.5194/amt-11-499-2018, 2018.

1368

- 1369 Twomey, S.: Pollution and the planetary albedo. Atmospheric Environment (1967), 8(12), 1251–1256,
- 1370 <u>https://doi.org/10.1016/0004-6981(74)90004-3</u>, 1974.

1371

- 1372 Vaughan, M., Powell, K., Kuehn, R., Young, S., Winker, D., Hostetler, C., Hunt, W., Liu, Z., McGill, M., and
- 1373 Getzewich, B.: Fully automated detection of cloud and aerosol layers in the CALIPSO lidar measurements, J. Atmos.
- 1374 Ocean. Tech., 26, 2034–2050, https://doi.org/10.1175/2009JTECHA1228.1, 2009.

1375

- 1376 Venkata, S. L. and Reagan, J. A.: Aerosol Retrievals from CALIPSO Lidar Ocean Surface Returns, Remote Sens., 8,
- 1377 1006, https://doi.org/10.3390/rs8121006, 2016.

1378

Waquet, F. et al. Global analysis of aerosol properties above clouds Geophys. Res. Lett. 40, 5809–5814, 2013.

1380

- Wehr, Tobias, et al. "The EarthCARE mission-science and system overview." Atmospheric Measurement Techniques
- 1382 16.15: 3581-3608, 2023.

1383

- Wilcox, E. M.: Direct and semi-direct radiative forcing of smoke aerosols over clouds, Atmos. Chem. Phys., 12, 139-
- 1385 149, https://doi.org/10.5194/acp-12-139-2012, 2012.

1386

- 1387 Wind, G., Platnick, S., Meyer, K., Arnold, T., Amarasinghe, N., Marchant, B., and Wang, C.: The CHIMAERA system
- for retrievals of cloud top, optical and microphysical properties from imaging sensors, Computers & Geosciences,
- 1389 134, 104345–6, https://doi.org/10.1016/j.cageo.2019.104345, 2020

1390

- Winker, D. M., Vaughan, M. A., Omar, A., Hu, Y., Powell, K. A., Liu, Z., Hunt, W. H., and Young, S. A.: Overview
- of the CALIPSO mission and CALIOP data processing algorithms, J. Atmos. Ocean. Tech., 26, 2310-2323,
- 1393 https://doi.org/10.1175/2009JTECHA1281.1, 2009.

1394

- Witte, M. K., Yuan, T., Chuang, P. Y., Platnick, S., Meyer, K. G., Wind, G., & Jonsson, H. H: MODIS Retrievals of
- 1396 Cloud Effective Radius in Marine Stratocumulus Exhibit No Significant Bias. Geophysical Research
- 1397 Letters, 45(19). https://doi.org/10.1029/2018GL079325, 2018.

- 1399 Xu, H., Guo, J., Ceamanos, X., Roujean, J.-L., Min, M., and Carrer, D.: On the influence of the diurnal variations of
- aerosol content to estimate direct aerosol radiative forcing using MODIS data, Atmos. Environ., 141, 186–196, 2016.

- 1402 Young, S. A. and Vaughan, M. A.: The retrieval of profiles of particulate extinction from Cloud Aerosol Lidar
- 1403 Infrared Pathfinder Satellite Observations (CALIPSO) data: Algorithm description, J. Atmos. Ocean. Tech., 26,
- 1404 1105–1119, https://doi.org/10.1175/2008JTECHA1221.1, 2009.

1405

- 1406 Young, S. A., Vaughan, M. A., Tackett, J. L., Garnier, A., Lambeth, J. B., and Powell, K. A.: Extinction and Optical
- 1407 Depth Retrievals for CALIPSO's Version 4 Data Release, Atmos. Meas. Tech., 11, 5701-5727,
- 1408 <u>https://doi.org/10.5194/amt-11-5701-2018</u>, 2018.

1409

- 1410 Yu, H., Kaufman, Y. J., Chin, M., Feingold, G., Remer, L. A., Anderson, T. L., Balkanski, Y., Bellouin, N., Boucher,
- O., Christopher, S., DeCola, P., Kahn, R., Koch, D., Loeb, N., Reddy, M. S., Schulz, M., Takemura, T., and Zhou,
- 1412 M.: A review of measurement-based assessments of the aerosol direct radiative effect and forcing, Atmos. Chem.
- 1413 Phys., 6, 613–666, https://doi.org/10.5194/acp-6-613-2006, 2006.

1414

- 1415 Zhang, Z., Meyer, K., Yu, H., Platnick, S., Colarco, P., Liu, Z., and Oreopoulos, L.: Shortwave direct radiative effects
- of above-cloud aerosols over global oceans derived from 8 years of CALIOP and MODIS observations, Atmos. Chem.
- 1417 Phys., 16, 2877–2900, https://doi.org/10.5194/acp-16-2877-2016, 2016.

1418

- 2 Zhang, J. and P. Zuidema: The diurnal cycle of the smoky marine boundary layer observed during August in the
- remote southeast Atlantic. Atmos. Chem. Phys., 19, p. 14493-14516, doi:acp-19-14493-2019, 2019.
- Zhang, H., Kondragunta, S., Laszlo, I., and Zhou, M.: Improving GOES Advanced Baseline Imager (ABI) aerosol
- optical depth (AOD) retrievals using an empirical bias correction algorithm, Atmos. Meas. Tech., 13, 5955–5975,
- 1423 https://doi.org/10.5194/amt-13-5955-2020, 2020.

1424

| DARE_theo | | | | | |
|--|--|--|--|--|--|
| Radiative Transfer Model | RRTMG-SW | | | | |
| | [COT =1, CER=12, CWP=8] or | | | | |
| Cloud Detection and Characterization | [COT=10, CER=12, CWP=80] | | | | |
| Cloud Albedo | N/A | | | | |
| Cloud Top Height (CTH) and Cloud Base Height | CTH is 1km and CBH is 0.5km | | | | |
| (СВН) | | | | | |
| Aerosol Top Height (ATH) and Aerosol Base | ATH is 5km and ABH is 1km above | | | | |
| Height (ABH) | СТН | | | | |
| Vertical distribution of spectral ASY | ASY = 0.6 | | | | |
| | Spectral SSA of two built-in RRTMG | | | | |
| V | aerosol types ⁽¹⁾ is weighted by | | | | |
| Vertical distribution of spectral SSA | AOD ₅₃₂ =0.3 for thirty-two canonical | | | | |
| | cases ⁽²⁾ | | | | |
| | Normalized spectral aerosol extinction | | | | |
| Vertical distribution of spectral aerosol extinction | coefficient of two built-in RRTMG | | | | |
| coefficient | aerosol types ⁽¹⁾ is multiplied by | | | | |
| Coefficient | AOD ₅₃₂ =0.3 for thirty-two canonical | | | | |
| | cases ⁽²⁾ | | | | |
| Atmospheric Composition and Weather | Assumed constant ⁽³⁾ | | | | |
| | Cox-Munk parametrization (Cox and | | | | |
| Ocean Surface BRDF | Munk, 1954; Jin et al., 2011) with a | | | | |
| Occan Sariace DRD1 | fixed chlorophyl concentration of 0.2 | | | | |
| | g/m^3 | | | | |

Table A1: Theoretical DARE_theo calculations for aerosols above clouds in our study and their respective inputs. (1) see "Continental average" and "Urban" aerosol types in Fig. A1; (2) see upper panels (a, b, c, d) in Fig. A2; (3) CO₂, N₂O, CH₄, O₂ and ocean surface wind speed are assumed equal to a single value (i.e., respectively 400 ppmv, 0.3 ppmv, 1.7 ppmv, 0.0 kg m³ and 4 m s⁻¹); the pressure, temperature, air density, water vapor and ozone profiles are also assumed constant and illustrated in Table A2; The instant DARE_theo uses the Solar Zenith Angle (SZA) at 15°S latitude and 8°E longitude on

15 September 2016. We compute twenty-four instant DARE_theo values based on twenty-four SZAs (every hour) throughout the day (at the same location and date) and average all instant DARE_theo to obtain the 24 h DARE_theo values.

| Z (km) | P (mb) | T (k) | Air Density | H ₂ O (g m ⁻³) | O_3 (g m ⁻³) |
|--------|----------|-------|-------------|---------------------------------------|----------------------------|
| 50 | 7.98E-01 | 270.6 | 1.03E+00 | 1.20E-05 | 4.00E-06 |
| ••• | ••• | ••• | | ••• | ••• |
| 15 | 1.21E+02 | 216.6 | 1.95E+02 | 7.20E-04 | 2.10E-04 |
| 14 | 1.42E+02 | 216.6 | 2.28E+02 | 8.40E-04 | 1.90E-04 |
| 13 | 1.66E+02 | 216.6 | 2.67E+02 | 1.80E-03 | 1.70E-04 |
| 12 | 1.94E+02 | 216.6 | 3.12E+02 | 3.70E-03 | 1.60E-04 |
| 11 | 2.27E+02 | 216.8 | 3.65E+02 | 8.20E-03 | 1.30E-04 |
| 10 | 2.65E+02 | 223.2 | 4.14E+02 | 1.80E-02 | 9.00E-05 |
| 9 | 3.08E+02 | 229.7 | 4.67E+02 | 4.60E-02 | 7.10E-05 |
| 8 | 3.57E+02 | 236.2 | 5.26E+02 | 1.20E-01 | 5.20E-05 |
| 7 | 4.11E+02 | 242.7 | 5.90E+02 | 2.10E-01 | 4.80E-05 |
| 6 | 4.72E+02 | 249.2 | 6.60E+02 | 3.80E-01 | 4.50E-05 |
| 5 | 5.41E+02 | 255.7 | 7.36E+02 | 6.40E-01 | 4.50E-05 |
| 4 | 6.17E+02 | 262.2 | 8.19E+02 | 1.10E+00 | 4.60E-05 |
| 3 | 7.01E+02 | 268.7 | 9.09E+02 | 1.80E+00 | 5.00E-05 |
| 2 | 7.95E+02 | 275.1 | 1.01E+03 | 2.90E+00 | 5.40E-05 |
| 1 | 8.99E+02 | 281.6 | 1.11E+03 | 4.20E+00 | 5.40E-05 |
| 0 | 1.01E+03 | 288.1 | 1.23E+03 | 5.90E+00 | 5.40E-05 |

Table A2. Atmospheric profiles of pressure, temperature, air density, water vapor and ozone used in the calculation of DARE_theo (see Table A1); see the legend of Table A1 for constant CO₂, N₂O, CH₄, O₂ and ocean surface wind speed values.



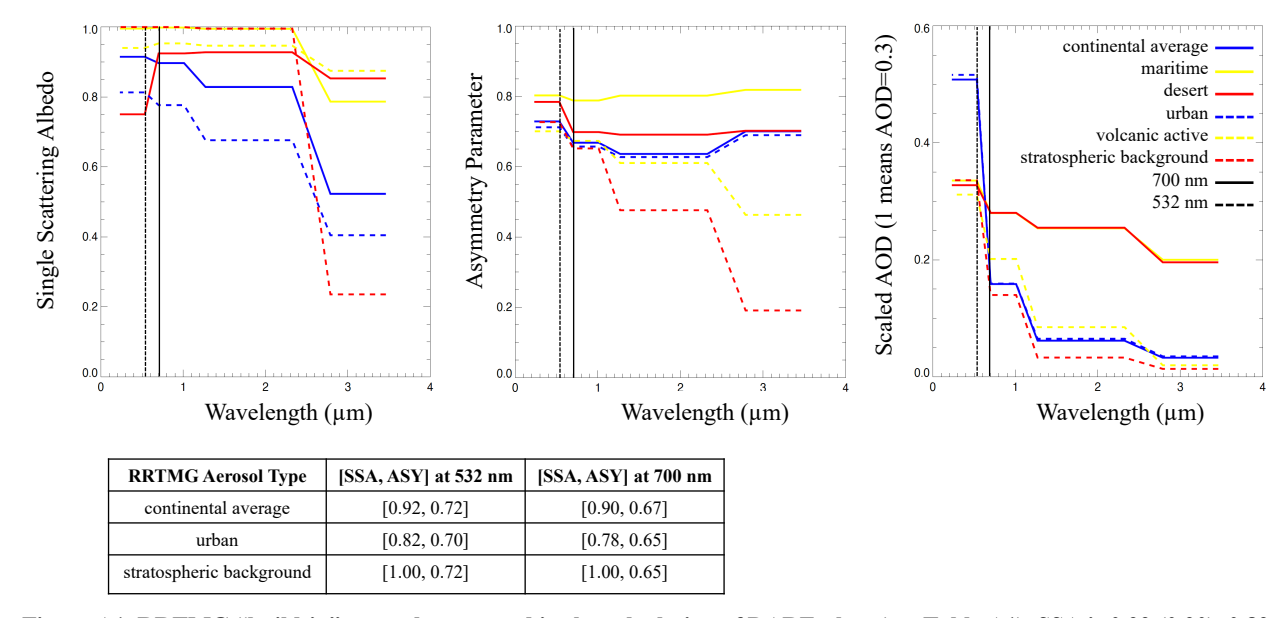


Figure A1. RRTMG "build-in" aerosol types used in the calculation of DARE_theo (see Table A1). SSA is 0.92 (0.90), 0.82 (0.78), 1.00 (1.00) for RRTMG "Continental Average", "Urban" and "Stratospheric Background" aerosol types at 532 (700) nm. Note that RRTMG "Continental Average" seems to correspond roughly to biomass burning smoke aerosol types in Russell et al. (2014). Also note that RRTMG "Urban" seems to correspond to aerosols with considerably higher light absorption properties than the smoke types in Russell et al. (2014). ASY is 0.72 (0.67), 0.70 (0.65) and 0.72 (0.65) for RRTMG "Continental Average", "Urban" and "Stratospheric Background" at 532 (700) nm. Aerosol types are taken from the Optical Properties of Aerosols and Clouds (OPAC) software (Hess et al., 1998).



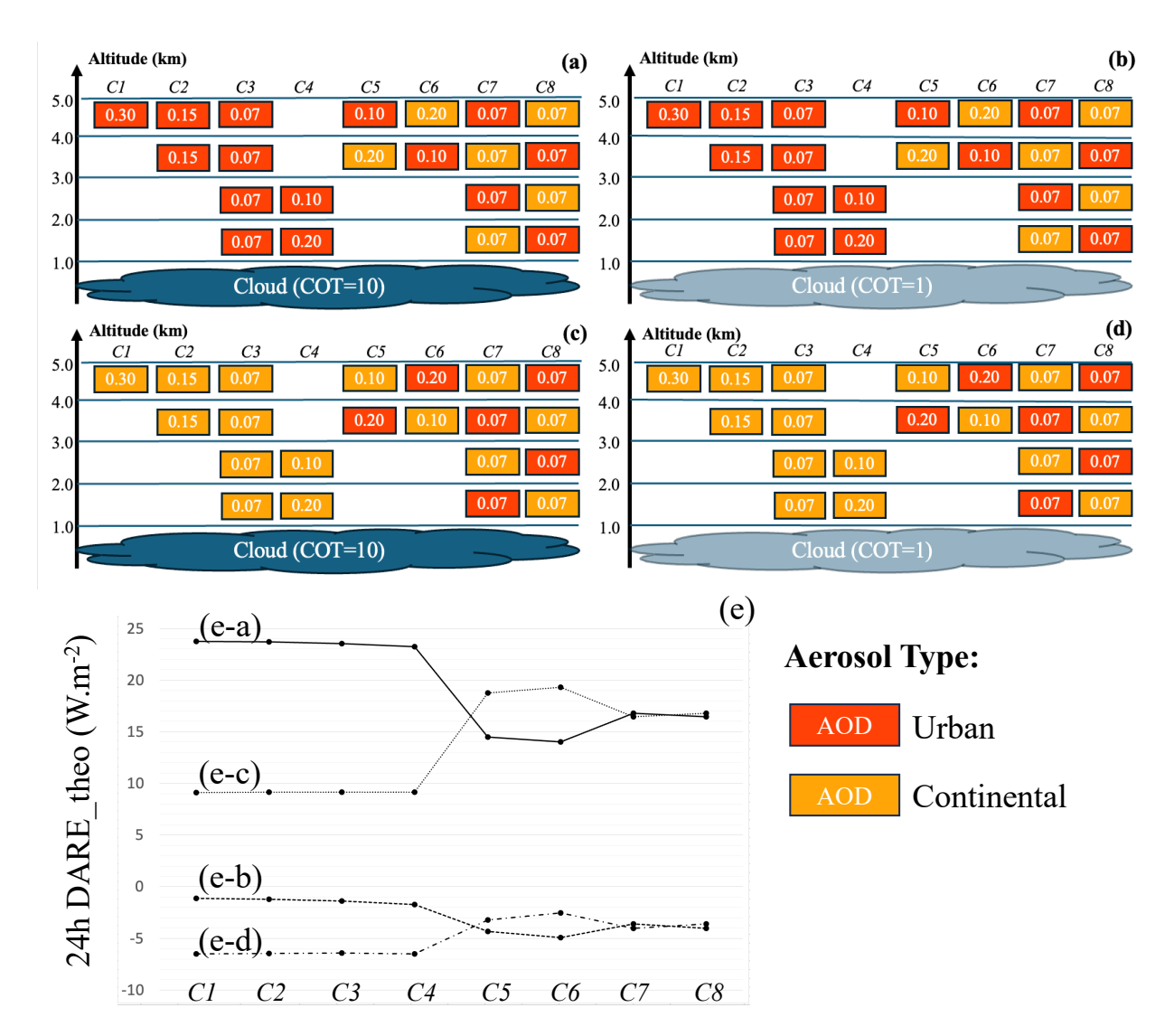


Figure A2. 24 h mean theoretical DARE_theo (in W·m⁻²) results in (e) for thirty-two canonical cases (i.e., eight cases in (a), (b), (c) and (d)) where we vary COT, the number of aerosol layers over clouds, the order of aerosol types and the loading of aerosols over clouds. Orange and red boxes depict two "build-in" RRTMG aerosol types, respectively "Continental average" in orange and "Urban" in red; see Fig. A1 for the optical and microphysical properties of these aerosol types. The vertical distribution of spectral SSA and extinction coefficient are weighed by the AOD above clouds that is assumed constant and equal to 0.3 at 532nm (i.e., in the 442-625 nm RRTMG broadband channel). See Table A1 for a list of the inputs to the DARE theo calculations.

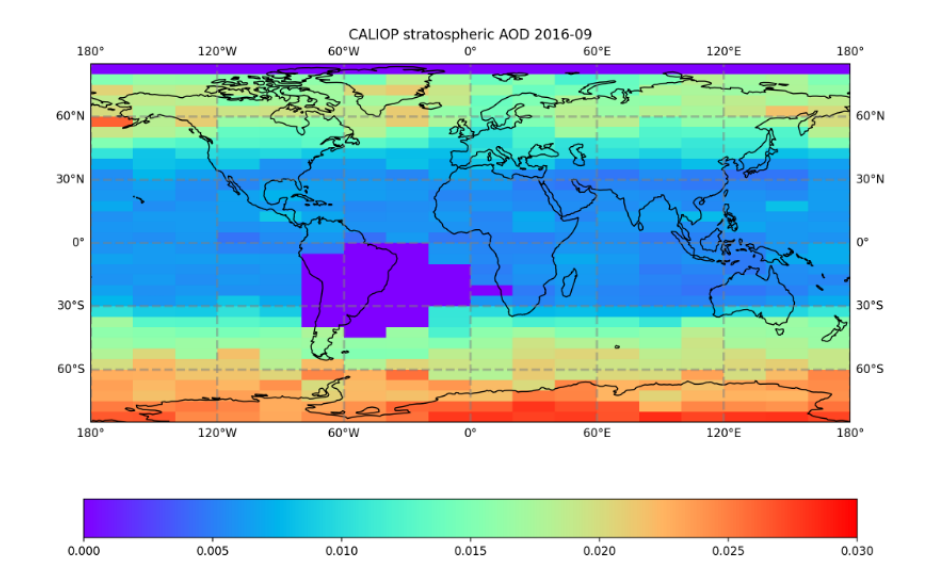


Figure A3: Stratospheric aerosols that are deleted when computing DARE_obs (see Table 2)

| Method to compute DARE obs in each atmospheric scenario | | | | | | | | |
|---|---|-------------------------|---|---|--|--|--|--|
| Atmospheric | S1 | S2 | S3 | S4 | | | | |
| Scenario | | | | | | | | |
| AOD, and vertical | We | use | We use CALIOP _{ACAOD_standard} | We use CALIOPODAOD or | | | | |
| spectral extinction, | CALIOPAG | CAOD_DR | (E-1) (E-4) (E-5) | CALIOP _{AOD_standard} | | | | |
| SSA and ASY | (E-1) (E-4) | (E-5) | | (E-1) (E-4) (E-5) | | | | |
| | Aerosol co | omposition i | Aerosol composition is | | | | | |
| | vertical SS | A, ASY and | d extinction above clouds (E-1) and | informed by MERRA-2 | | | | |
| | below clou | ds (E-1) (E- | 2) | spectral vertical SSA, ASY | | | | |
| | | | | and extinction (E-1) | | | | |
| Aerosol Top Height | ATH=CAL | LIOP _{vfm} upp | ermost ATH (E-3) and ABH=CTH | ATH=CALIOP _{vfm} uppermost | | | | |
| (ATH) and Base | above clou | ds; ATH an | d ABH are informed by MERRA-2 | ATH (E-3); | | | | |
| Height (ABH) | below clou | ds (E-2) | | ABH=CALIOP _{vfm} lowermost | | | | |
| | | | | ABH | | | | |
| CWP, CER, Cloud | We use | MODISC | loud CWP and CER (E-6); | N/A | | | | |
| Top Height (CTH) | CTH=CAL | LIOP _{vfm} CTF | H; CBH = CTH - 500m | | | | | |
| and Base Height | | | | | | | | |
| (CBH) | | | | | | | | |
| More information on | | | | | | | | |
| CALIOP _{ACAOD_DR} | Median v | alue of s | ingle shot CALIOP _{ACAOD_DR} from | m Hu et al. (2007) using | | | | |
| | Column_Pa | articulate_O | ptical_Depth_Above_Opaque_Water | r_Cloud_532 in | | | | |
| | | _ | ILay product within 5km that is inclu | | | | | |
| | _ | | nction flag) are applied on CALIOPA | ACAOD_DR; Stratospheric Aerosol | | | | |
| | - | | is removed from each profile ^(*) | | | | | |
| | _ | | on profile between ATH and ABH us | | | | | |
| CALIOP _{ACAOD_standard} | | | nAPro product; Extinction flag for C | ALIOP _{ACAOD_standard} needs to be | | | | |
| | equal to 0, | | | | | | | |
| CALIOP _{AOD_standard} | | | on profile between ATH and ABH us | | | | | |
| | | | mAPro product; Extinction flag for | CALIOPAOD_standard needs to be | | | | |
| | equal to 0, | | | | | | | |
| CALIOPODAOD | | | n Optical Depths (ODCOD) from V | • , , , | | | | |
| | Ryan e | - | _ | tive_Optical_Depth_532 in | | | | |
| | | _ | fLay product); observation is valid if | • | | | | |
| | | | ce integrated depolarization ratio < | | | | | |
| | detected at 1km or at Single shot resolution, (iii) if wind speed is between 3 and 15m.s ⁻¹ ; if | | | | | | | |
| | observation | 1 is valid, th | en use the median of all single shot | CALIOP _{ODCOD} within 3km that | | | | |

| ſ | | | | | | |
|----------------------------|---|--|--|--|--|--|
| | includes the 1 km stretch; we apply no filters or QA flags (e.g., extinction flag) on | | | | | |
| | CALIOP _{ODAOD} ; Stratospheric Aerosol Optical Depth (SAOD) is removed from each | | | | | |
| | profile(*) | | | | | |
| When do we use | We start with CALIOP _{ODAOD} ; if conditions are not met for (i), (ii) and (iii) in the line above, | | | | | |
| CALIOP _{ODAOD} or | then we use CALIOPAOD_standard | | | | | |
| CALIOPAOD_standard | | | | | | |
| for S4? | | | | | | |
| Three versions of CA | LIOP-derived AOD: | | | | | |
| 171 | For each 1km stretch, consider only valid CALIOPACAOD_DR or CALIOPACAOD_standard; when | | | | | |
| V1 | there is no valid CALIOPACAOD_DR or CALIOPACAOD_standard data, do not replace | | | | | |
| | For each 1km stretch, if CALIOPACAOD_DR (or CALIOPACAOD_standard) is not valid for S1, S2 | | | | | |
| 1/2 | or S3, the invalid point is replaced by ± 10 km median single shot CALIOP _{ACAOD_DR} ; For S3, | | | | | |
| V2 | $if\pm 10 km\ median\ single\ shot\ CALIOP_{ACAOD_DR}\ is\ still\ not\ available,\ invalid\ point\ is\ replaced$ | | | | | |
| | by 5km CALIOP _{ACAOD_standard} | | | | | |
| | For each 1km stretch, use median of rolling ±10km median of single shot CALIOP _{ACAOD_DR} | | | | | |
| V3 | for S1, S2, S3. If the latter does not exist for S3, then use 5km CALIOPACAOD_standard; For | | | | | |
| V3 | each 1km stretch, ATH is replaced everywhere by rolling ± 10 km median V1 ATH; If there | | | | | |
| | is no rolling median ATH available, ATH=median ATH for the entire orbit section | | | | | |
| We have assessed the | effects of these factors in the calculation of DARE obs: | | | | | |
| (E-1) | Apply threshold on extinction: If MERRA extinction < 0.014 km ⁻¹ and/ or CALIOP | | | | | |
| | extinction < 0.07km ⁻¹ (Rogers et al., 2011), assume no aerosols | | | | | |
| (E-2) | Add aerosol below clouds using MERRA-2 | | | | | |
| (E-3) | Extend ATH: If there is (i) no valid CALIOP _{vfm} uppermost ATH corresponding to a valid | | | | | |
| | ACAOD for S1-S4 and (ii) a valid median ATH ± 10 km centered on the invalid ATH then | | | | | |
| | ATH is replaced by ± 10 km median ATH; if (i) but not (ii), then ATH=median(orbit section) | | | | | |
| (E-4) | Use CALIOP-derived AOD V2 instead of V1 | | | | | |
| (E-5) | <u>Use CALIOP-derived AOD V2 instead of V3</u> | | | | | |
| (E-6) | Use clouds corrected (instead of uncorrected) for aerosols above them | | | | | |

Table A3: Detailed description of aerosol and cloud property inputs to DARE_obs calculations for each atmospheric scenario (see Table 3 for S1-S4). We also provide more information on CALIOP-derived input aerosol parameters and describe three CALIOP-derived AOD versions. (E-1) through (E-6) denote effects of varying factors in the calculation of DARE_obs. (E-1) through (E-6) are quantified in Table A4 and reported in section 2.1.4. In the main sections of this paper, we choose to display DARE_obs results with a threshold applied on the extinction coefficients (E-1), aerosols below clouds using MERRA-2 (E-2), ATH extended (E-3), CALIOP-inferred AOD version 2 and cloud properties from MODIS uncorrected for aerosols above them (E-6). (*) The way the Stratospheric Aerosol Optical Depth (SAOD) is removed from each profile is we compute a zonal SAOD from the equal-angle data product (see Fig. A3), then interpolate the zonal data

to the latitude grid of the CALIPSO granule observations and remove the SAOD from either CALIOP_{ACAOD_DR} or CALIOP_{ODAOD}.

| Effects of Varying Factors in DARE_obs Calculations | | | | | | | | | | | | | | | |
|---|------------------|-----------------|----|----|----|----|--------|-----|-----------------|---|----------------------------------|-----------------------------------|--------------------------------------|---------------------------------------|---|
| Th | reshold on | no | ye | ye | ye | ye | ye | yes | yes | ent | | | | | 4) |
| e | xtinction? | | S | S | S | s | S | | | E-1) Adding a threshold on extinction coefficient | | | 1 | 3 | (E-6) Using clouds corrected for aerosols above |
| ATH extended? | | ye | ye | ye | no | ye | ye | yes | yes | 900 1 | | | D V | D V. | ols 8 |
| AII | A i fi extended? | | s | S | | S | s | | | ction | 70 | ţ | A0 | A0 | eros |
| A.C | AOD warratara 9 | | V | V | V | V | V | V2 | V2 | xtin | xtinc | eigh | d to | d to | or a |
| AOD version? | | 1 | 1 | 1 | 1 | 2 | 3 | | | ou e | E-2) Adding aerosol below clouds | E-3) Extending aerosol top height | E-4) Using AOD V2 compared to AOD V1 | (E-5) Using AOD V2 compared to AOD V3 | ted i |
| Aeroso | l below clouds? | no | no | ye | ye | ye | ye | yes | yes | plor | pelo | sol t | com | com | rrec |
| 1101050 | i below clouds. | | | S | S | S | S | | | ıresl | osol | aero | V2 | V2 | ls co |
| Cloud | s corrected for | no | no | no | no | no | no | no | yes | a th | aer | ing a | NOD | VOD | Jone |
| aer | osols above? | | | | | | | | | ding | ding | tend | √ Bu | ng ∤ | o Bu |
| | AOD? | | | 2 | :0 | | | > | 0.3 | Ad | Ad | Ext | Usi | Usi |) Usi |
| | | | | | | | | | E-1) | E-2) | E-3 | E 4 | E-5) | E-6 | |
| | | | | | | | | Th | ick | | | | | Thick | |
| Where? | | All-sky (S1-S4) | | | | | clouds | | All-sky (S1-S4) | | | | clouds | | |
| | | | | | | | | | 51) | | | | | (S1) | |
| | 9/18/16 | 11 | 11 | 11 | 10 | 11 | 11 | 154 | 154 | 0 | 0 | 1 | 53 | 0 | 0 |
| | | 07 | 07 | 07 | 97 | 60 | 60 | | | | | 0 | | | |
| Number | 9/20/16 | 87 | 87 | 87 | 87 | 88 | 88 | 597 | 597 | 0 | 0 | 0 | 9 | 0 | 0 |
| Nun | | 8 | 8 | 8 | 8 | 7 | 7 | | | | | | | | |
| | 8/13/17 | 74 | 74 | 74 | 73 | 80 | 80 | 23 | 23 | 0 | 0 | 2 | 65 | 0 | 0 |
| | | 1 | 1 | 1 | 9 | 6 | 6 | | | | | | | | |
| 2) | 9/18/16 | 23 | 22 | 21 | 21 | 20 | 20 | 38. | 37.3 | 0. | 1. | 0. | 1. | 2.3 | 1.9 |
| stant (W m ⁻²) | | .2 | .4 | .4 | .7 | .3 | .3 | 3 | | 8 | 0 | 3 | 1 | | |
| <u> </u> | 9/20/16 | 35 | 35 | 34 | 34 | 34 | 34 | 46. | 48.3 | 0. | 0. | 0. | 0. | 2.9 | 4.1 |
| Mean I DARE_ob | | .2 | .0 | .5 | .5 | .2 | .2 | 9 | | 2 | 5 | 0 | 4 | | |
| M | 8/13/17 | 12 | 12 | 10 | 10 | 9. | 8. | 80. | 82.5 | 0. | 1. | 0. | 1. | 3.2 | 3.0 |
| Ω | | .4 | .4 | .8 | .8 | 5 | 6 | 7 | | 0 | 6 | 1 | 3 | | |
| | | Ai | Bi | Ci | Di | Ei | Fi | Gi | Hi | mean(Ai-Bi) | mean(Bi-Ci) | mean(Ci)-mean(Di) | mean(Ci)-mean(Ei) | mean(Ei-Fi) | mean(Gi-Hi) |

Table A4: Effects of (E-1) adding a lower threshold on CALIOP and MERRA-2 extinction coefficients, (E-2) adding MERRA-2 aerosol below clouds, (E-3) extending aerosol Top Height (ATH) when there is no valid ATH from the CALIOP

standard product, (E-4) using AOD V2 instead of V1, (E-5) using AOD V3 instead of V2 and (E-6) using clouds corrected for aerosol above when AOD>0.3. Latitudes are selected between 6°S and 20°S.

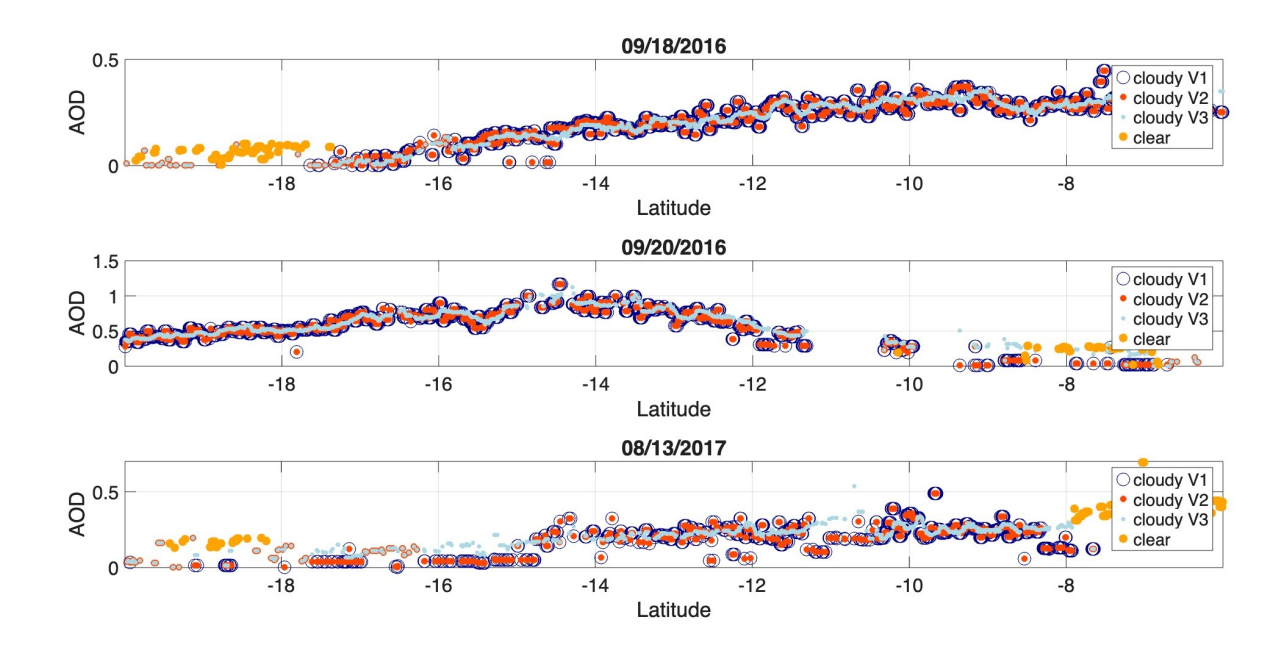


Figure A4: Evolution of CALIOP-inferred AOD V1, V2, and V3 above clouds (S1-S3) (see Table A3 for a definition of these versions) and in non-cloudy skies (S4) for our three case studies. We eventually select AOD V2 in this paper. Latitudes are selected between 6°S and 20°S.



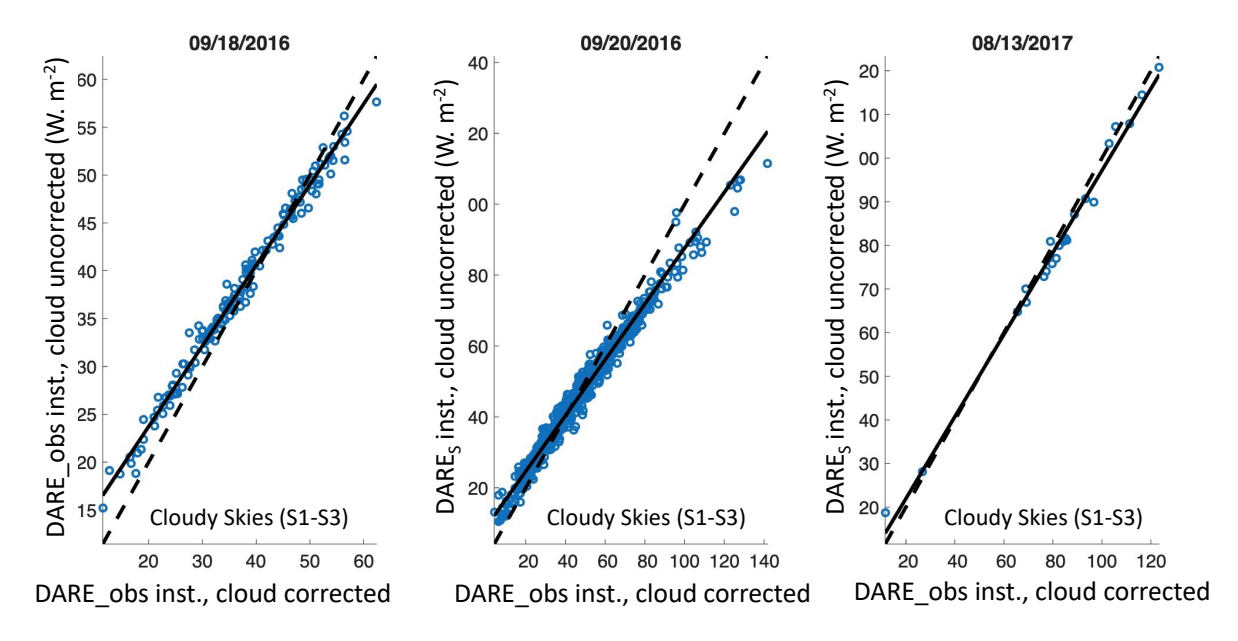


Figure A5: Illustration of the effects of using cloud properties corrected for aerosols above them in DARE_obs calculations (see E-6 in Table A3 and A4). Semi-observational instant cloudy (S1-S3) DARE_obs (W·m²) (see Table 2) using MODIS COT corrected for aerosol above (x-axis) vs. MODIS COT uncorrected for aerosol above (y-axis). We show only values with AOD>0.3 above clouds. See Table A5 for linear regression and correlation statistics. Latitudes are selected between 6°N and 20°S

| | | 9/18/16 | 9/20/16 | 8/13/17 |
|---|--|---------|---------|---------|
| Mean instant cloudy (S1-S3) DARE_obs with clouds co | 37.32 | 48.29 | 82.46 | |
| Mean instant cloudy (S1-S3) DARE_obs with clouds un | 38.33 | 46.91 | 80.66 | |
| Instant DARE_obs using clouds corrected vs. using clouds uncorrected for aerosol above them | \mathbb{R}^2 | 0.99 | 0.98 | 0.99 |
| | Slama Offset | 0.84, | 0.79, | 0.94, |
| | Slope, Offset | 6.88 | 8.87 | 3.15 |
| | N | 154 | 597 | 23 |
| | RMSE | 2.3 | 5.66 | 3.41 |
| | Difference of Mean (W m ⁻²) | 1 | 1.38 | 1.8 |
| | Mean of Difference (W m ⁻²) | 1.86 | 4.06 | 2.98 |
| Mean COT with clouds corrected | 15.5 | 9.71 | 35.56 | |
| Mean COT with clouds uncorrected | | 13.64 | 8.11 | 28.35 |
| | \mathbb{R}^2 | 0.98 | 0.95 | 0.95 |
| | Slope, Offset | 0.72, | 0.60, | 0.69, |
| | Slope, Offset | 2.44 | 2.29 | 3.88 |
| COT with clouds corrected vs. with clouds | N | 154 | 597 | 23 |
| uncorrected for aerosol above them | RMSE | 2.45 | 2.2 | 8.55 |
| uncorrected for acrosor above them | Difference of Mean | 1.86 | 1.61 | 7.2 |
| | Mean of Difference | 1.88 | 1.63 | 7.24 |

Table A5: Effects of using cloud properties corrected for aerosols above them in DARE_obs calculations (E-6). These are the statistics behind Fig. A5 i.e., a comparison between instant DARE_obs using COT (or simply COT) with clouds corrected vs. clouds uncorrected for aerosol above them.

Results

| Averaged Values | | 9/18/16 | | | 9/20/16 | | 8/13/17 | | | |
|-------------------|-------|---------|-------|-------|---------|-------|---------|-------|-------|--|
| Averaged values | S1 | S2 | S3 | S1 | S2 | S3 | S1 | S2 | S3 | |
| Number | 968 | 31 | 68 | 724 | 22 | 94 | 334 | 64 | 221 | |
| DARE_obs 24 h | 10.33 | 2.03 | -1.37 | 17.62 | 11.98 | -0.13 | 14.11 | 6.6 | -1.2 | |
| ΔDARE_obs 24 h | 0.1 | 0.3 | 0.08 | 0.14 | 0.72 | 0.14 | 0.27 | 0.3 | 0.06 | |
| DARE_obs Instant | 24.99 | 3.65 | -4.1 | 42.29 | 27.03 | -1.98 | 35.91 | 14.39 | -4.7 | |
| ΔDARE_obs Instant | 0.26 | 0.72 | 0.21 | 0.39 | 1.91 | 0.39 | 0.73 | 0.77 | 0.15 | |
| СОТ | 11.6 | 5.95 | 1.82 | 7.64 | 6.05 | 2.14 | 14.62 | 6.01 | 1.59 | |
| CWP | 86.42 | 38.45 | 11.65 | 40.71 | 31.86 | 14 | 87.24 | 30.95 | 11.05 | |
| ΔCWP | 0.416 | 2.912 | 3.855 | 0.548 | 3.425 | 2.094 | 0.837 | 1.939 | 2.608 | |
| CER | 11.43 | 10.1 | 10.32 | 8.27 | 8.28 | 10.75 | 8.71 | 8.11 | 12.42 | |
| CALIOP_CF | 1 | 0.98 | 0.92 | 1 | 0.98 | 0.9 | 1 | 0.97 | 0.92 | |
| MODIS_CF | 1 | 1 | 0.82 | 1 | 1 | 0.88 | 1 | 1 | 0.8 | |
| AOD above clouds | 0.24 | 0.11 | 0.06 | 0.63 | 0.53 | 0.19 | 0.25 | 0.22 | 0.1 | |
| ΔΑΟD | 0.002 | 0.011 | 0.006 | 0.004 | 0.024 | 0.012 | 0.004 | 0.008 | 0.002 | |
| SSA | 0.84 | 0.82 | 0.81 | 0.87 | 0.86 | 0.88 | 0.81 | 0.8 | 0.83 | |
| ASY | 0.64 | 0.63 | 0.64 | 0.67 | 0.66 | 0.68 | 0.6 | 0.59 | 0.62 | |
| EAE | 1.86 | 1.77 | 1.67 | 1.89 | 1.91 | 1.81 | 2.1 | 2.1 | 1.92 | |
| ATH | 4.59 | 4.38 | 4.44 | 5.24 | 4.98 | 4.26 | 2.95 | 3.02 | 2.7 | |
| СТН | 1.02 | 0.93 | 0.86 | 0.64 | 0.59 | 0.76 | 1.11 | 0.91 | 0.73 | |

Table A6: This table complements Table 5 – it is a breakdown of cloudy skies (S1-S3) into individual S1, S2 and S3 scenarios (see Table 3). Averaged aerosol, cloud and DARE_obs properties per atmospheric scenario, and case study. We display results corresponding to AOD version 2 (see Table A3 for more information on version 2). ΔSSA is fixed at 0.05 and ΔASY is fixed at 0.02 (see Table 4). Latitudes are selected between 6°S and 20°S. AOD is at 532 nm; SSA, ASY and 24h DARE_obs are in the 442-625 nm RRTMG channel; EAE is computed between the 442-625 nm and the 625-778 nm RRTMG channels; SSA, EAE and ASY are selected at the highest aerosol height in MERRA-2.

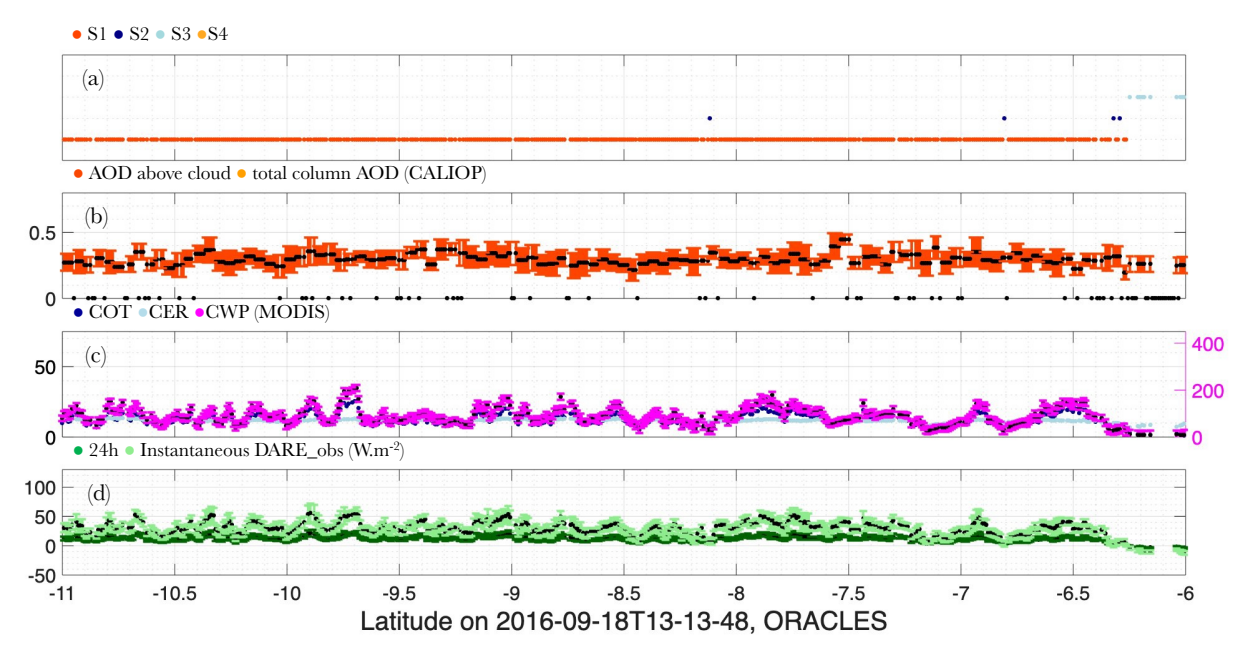


Figure A6: Same legend as for Fig. 5 but for 09/18/2016.

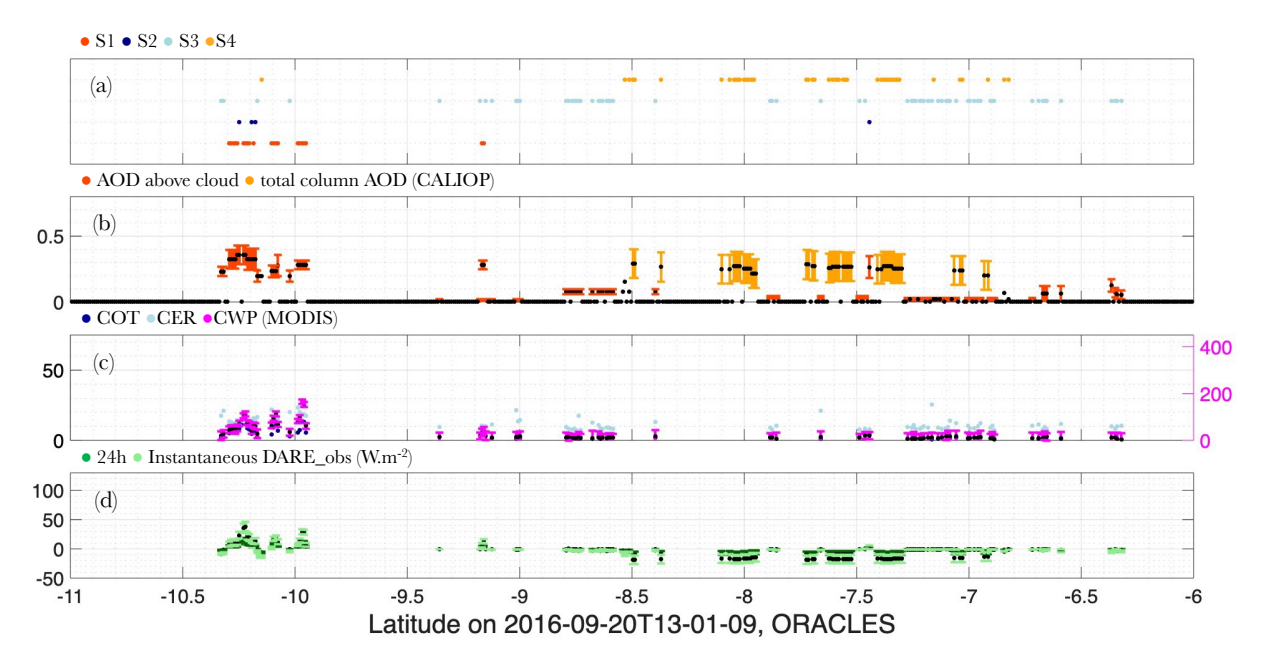
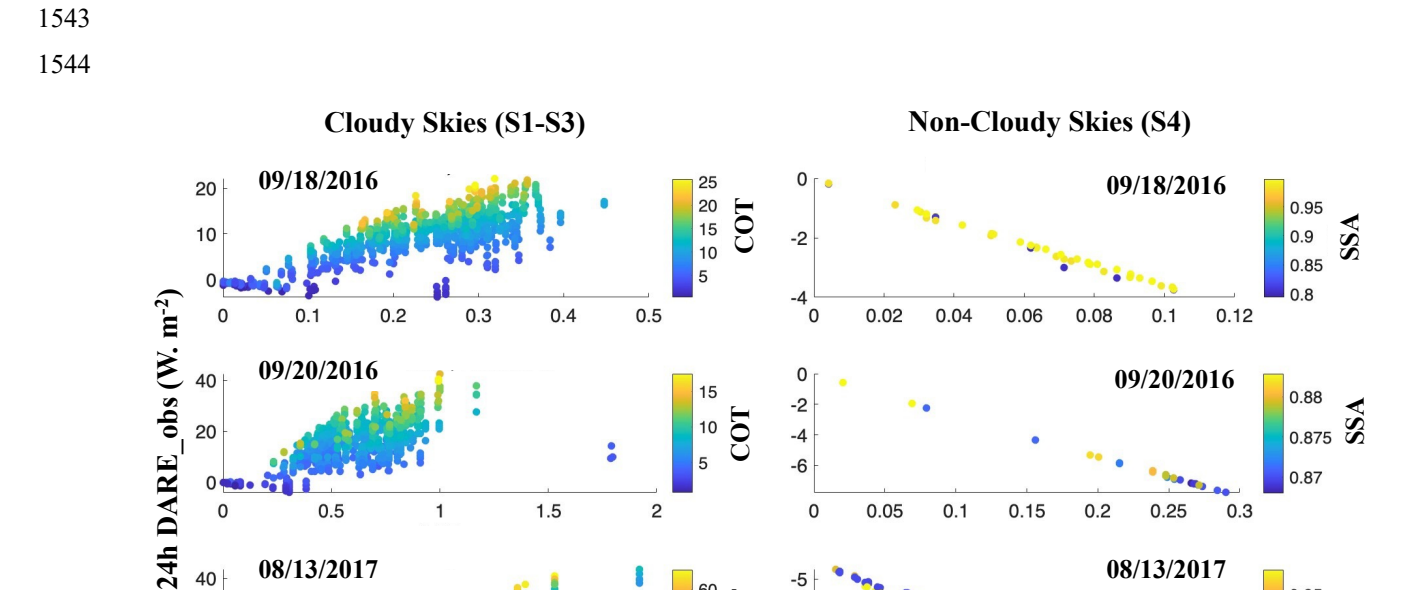


Figure A7: Same legend as for Fig. 5 but for 09/20/2016.



60 LOO

10

15

0.1

0.2

0.3

0.4

AOD

0.5

0.6

0.95

0.9

0.85

0.7

15411542

15451546

1547

1548

1549

1550

1551155215531554

20

0.2

0.1

0.4

0.3

AOD

0.5

Figure A8: 24 h DARE_obs in cloudy skies (S1-S3) (y-axis) as a function of AOD (x-axis) and COT (color bar) (left) and 24 h DARE_obs in non-cloudy skies (S4) (y-axis) as a function of AOD (x-axis) and SSA (color bar) (right) on 09/18/2016 (top), 09/20/2016 (middle) and 08/13/2017 (bottom). Cloud retrieved optical properties are not corrected for aerosols above them. Latitudes are selected between 6°S and 20°S. AOD is at 532 nm; SSA and 24h DARE_obs are in the 442-625 nm RRTMG channel; SSA are selected at the highest aerosol height in MERRA-2.



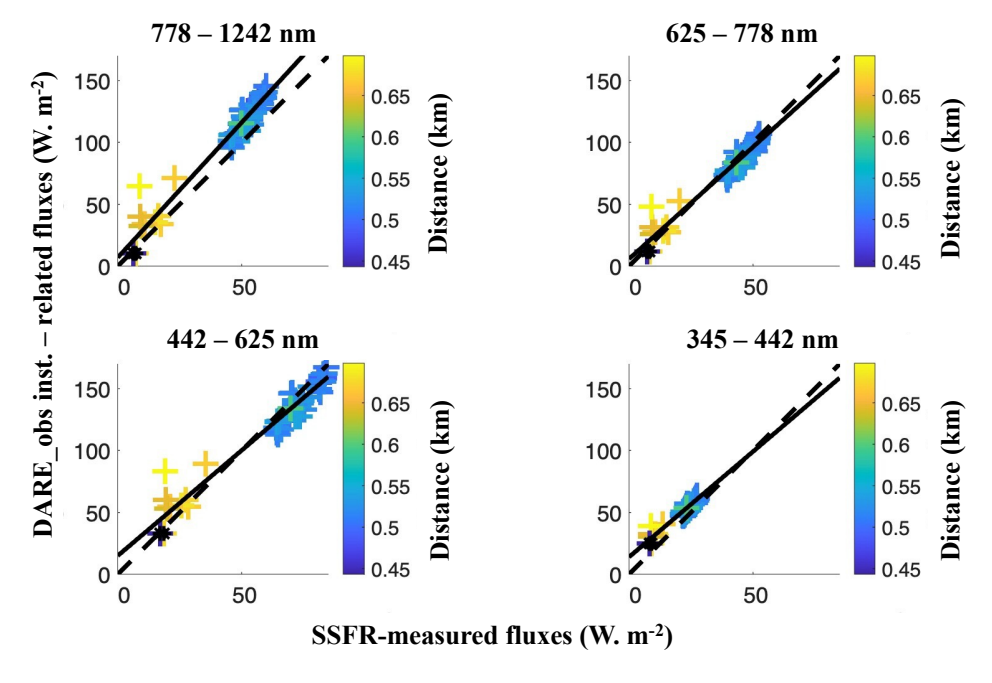


Figure A9: Instant SSFR-measured fluxes (x-axis) vs. instant DARE_obs-related fluxes (W·m⁻²) (y-axis) in four RRTMG broadband channels (clockwise: 778 - 1242, 625 - 778, 345 - 442 and 442 - 625 nm). Points are colored by the distance between the aircraft and the CALIOP track (km). Black crosses are points in non-cloudy sky conditions (S4). See second part of Table 6 in the text for statistics.